Palladium-Based Catalysts for Ethanol Electrooxidation in Alkaline Media

By

Nicolas Brazeau

Thesis submitted to the
Faculty of Graduate and Postdoctoral Studies
in partial fulfillment of the requirements
for the Degree of Master of Applied Science in
Chemical Engineering

Department of Chemical and Biological Engineering
Faculty of Engineering
University of Ottawa

Résumé

Les piles à combustibles à l'éthanol ont été démontrées comme étant une bonne alternative aux moteurs à combustion interne dans le but de réduire les émissions de CO_2. Dans cette étude, des nanocatalyseurs à base de Pd sont déposé sur différents supports (noir de charbon, graphène, SnO_2, CeO_2, TiO_2, nanotubes de TiO_2 et SnO_2 sur nanotubes de TiO_2) et leurs effets sur les propriétés catalytiques envers l'oxydation d'éthanol en milieu alcalin du catalyseur sont étudiés. Ces modifications du système catalytique se sont exprimées par une augmentation de la vitesse de réaction à la surface du catalyseur et une réduction du potentiel de déclenchement de la réaction d'oxydation d'éthanol. Deux mécanismes favorisant l'oxydation d'éthanol sur les systèmes catalytiques ont été identifiés. Premièrement, l'apport d'ions OH^- à l'interface métal-support facilite l'oxydation des molécules adsorbées sur des sites de Pd avoisinant. Deuxièmement, une augmentation de la densité d'électron dans les nanoparticules de Pd cause une modification de l'énergie d'adsorption de l'éthanol et des molécules intermédiaires de son oxydation ce qui influence la vitesse de réaction.

Abstract

Direct ethanol fuel cells have been shown to be a good alternative to internal combustion engines in order to reduce the CO_2 emissions. In this study, Pd and Pd-based nanocatalysts were deposited on various supports (carbon black, graphene, SnO_2, CeO_2, TiO_2, TiO_2 nanotubes and SnO_2/TiO_2 nanotubes) and their effects on the catalytic properties of the deposited metal for ethanol oxidation in alkaline media are studied. These modifications to the catalytic systems have shown to cause an increase in the reaction rate at the surface of the catalyst and to reduce the overpotential of the ethanol oxidation reaction. Two different promotion mechanisms have been identified. Firstly, the supply of OH^- ions at the metal-support interface facilitates the oxidation of adsorbed molecules on neighbouring Pd sites. Secondly, an increase in electron density of Pd nanoparticles with increasing support reducibility modifies the adsorption strength of ethanol and its oxidation intermediates.

Acknowledgements

I would like to acknowledge the work of all those people who helped in the research leading to the redaction of this thesis.

Firstly, I would like to thank my supervisor Dr. Elena Baranova for her financial support, insight, encouragements and the opportunities that she offered me. She did a great job in guiding me throughout those two years.

Secondly, I would like to thank (former and present) coworkers who helped me with my work. Thank you Maxime Lortie, Holly Dole, Spyridon Ntais, Evans Monyoncho and Rima Isaifan it has been a pleasure to work with you.

Troisièmement, j'aimerais remercier les gens formidables qui m'ont accueilli lors de mon séjour à l'Université d'Aix Marseille au Centre Interdisciplinaire de Nanoscience de Marseille. Merci à vous Loïc Assaud, Maïssa Barr et Dr. Lionel Santinacci.

Fourthly, I would like to thank our collaborator at the Chang Gung University, for the synthesis of sulphonated graphene, for physicochemical characterizations and for their help with electrochemical characterizations. Thanks to Dr. Chia-Liang Sun, Jui-Shiang Tang and Jhing-Jhou Wu.

Fifthly, I would like to thank the guys of the technical staff (Louis, Franco and Gérard) who were always eager to help with new experiments.

Statement on Contributions of Collaborators

I hereby certify that I am the author of this thesis. All the experimental work, the data analysis and the redaction of this thesis was made under the supervision of Dr. Elena A. Baranova. All assistance for experimental work, data collection and data analysis is acknowledged at the end of each chapter.

Dédicace

J'aimerais dédier cette œuvre à tous ceux que j'aime et qui m'entourent. Ils m'ont supporté sans cesse et ce, sans jamais questionner si j'allais réussir à surmonter l'épreuve qu'est l'obtention d'un (ou deux) diplôme universitaire. Sans vous je ne serais pas rendu ici.

Premièrement, je veux dédier cette thèse à ma fiancée, Valérie, bientôt ma femme, sans qui sa rédaction aurait été bien plus facile mais, oh combien moins plaisante. Tu m'as fait passer des moments inoubliables, les restos, les cinémas, les voyages, les rencontres, les surprises et les joies tout au long de notre séjour universitaire. J'aimerais inclure que la fin de ce semestre marquera la fin d'une étape de notre vie et le début d'une autre qui nous permettra de réaliser tous nos rêves.

Deuxièmement, j'aimerais que mes parents puissent recevoir eux aussi une partie des mérites pour le cheminement qui m'a apporté jusqu'où je suis aujourd'hui. Ils m'ont supporté autant financièrement que moralement sans jamais mettre en doutes mes choix et je ne pourrais leur en être plus reconnaissant.

En dernier lieu, je voudrais saluer quelques groupes de gens méritant une mention suite aux rôles qu'ils jouent/ont joués dans ma vie. Premièrement, le reste de ma famille: Guillaume (le meilleur frère) et ma très chère grand-mère Rita Colle. Deuxièmement, ma deuxième famille: Chantal Lapensée, Alain, Sara et Alexandre Chartrand et tous les autres. Troisièmement, mes amis à l'université: Maxime Lortie, Benoit Duhoux, Ryad Rahman et Jordan O'Reilly et ailleurs: Daniel Poirier, Guillaume Leclair et Marc-André Fortier.

Table of Contents

Table of Figures

Table of Tables

Nomenclature

Abbreviations

ACF	Activated Carbon Fiber
AEM	Anion Exchange Membrane
AFC	Alkaline Fuel Cell
AFM	Atomic Force Microscopy
AG	As Grown
ALD	Atomic Layer Deposition
Ann	Annealed
a_s	Specific Surface Area
Aux	Auxiliary
Bmim	1-ethyl-3-methylimidazolium
CA	Chronoamperometry
CMS	Carbon Microspheres
CNFs	Carbon Nanofibers
CNTs	Carbon Nanotubes
CV	Cyclic Voltammogram
DAEFC	Direct Alkaline Ethanol Fuel Cell
DEFC	Direct Ethanol Fuel Cell
ECSA	Electrochemical Active Surface Area
EOR	Ethanol Oxidation Reaction
ETFE	Poly(Ethylene-co-Tetrafluoroethylene)
fcc	Face-Centered Cubic
f-CNFs	Fish-Bone Carbon Nanofibers
FEP	Poly(hexafluoropropylene-co-tetrafluoroethylene)
FWHM	Full Width at Half Maximum
GDL	Gas Diffusion Layer
GEO	Geometrical Surface Area
Hg/HgO	Mercury/Mercury Oxide Reference Electrode
$Hg/HgSO_4$	Mercury/Mercury Sulphate Reference Electrode
HRTEM	High Resolution Transmission Electron Microscopy
ICE	Internal Combustion Engines
IPCC	Intergovernmental Panel on Climate Change
ISPs	Ion Solvating Polymers
LSV	Linear Scan Voltammetry

MEA	Membrane Electrode Assembly
MMO	Mercury/Mercury Oxide Reference Electrode
MSE	Mercury/Mercury Sulphate Reference Electrode
MWCNTs	Multiwall Carbon Nanotubes
ORR	Oxygen Reduction Reaction
PBI	Poly(benzimidazole)
p-CNFs	Platelet Carbon Nanofibers
Pd(hfac)$_2$	Palladium Hexafluoroacetylacetone
PEGDE	Poly(ethylene glycol) Dimethyl Ether
PEM	Proton Exchange Membrane
PEMFC	Proton Exchange Membrane Fuel Cell
PVA	Poly(vinyl) Alcohol
PVP	Poly(vinylpyrrolidone)
QCM	Quartz Crystal Microbalance
SEM	Scanning Electron Microscopy
sG	Sulphonated Graphene
t-CNFs	Tubular Carbon Nanofibers
TDMASn	Tetrakisdimethylamido Tin
TEM	Transmission Electron Microscopy
TiO$_2$-nts	Titanium Dioxide Nanotubes
VWA	Volume Weighted Average
XPS	X-ray Photoelectron Spectroscopy
XRD	X-ray Diffraction

List of symbols

2θ	Bragg's Diffraction Angle
b	Backward
d	Diameter
f	Forward
I	Current
i	Current Density
K	Dimensionless Shape Factor
P	Power
Q	Charge (mC)
r	Radius
B	FWHM
λ	X-ray Wavelength (Å)
Λ	Power Gain Ratio
ρ	Power Enhancement Ratio
τ	Average Crystallite Size

Chapter 1 : General Introduction

1.1 Present Global Situation

The Intergovernmental Panel on Climate Change (IPCC) published their Fourth Assessment Report in 2007 assessing the current knowledge of the climate change situation at the time of publication. The Fifth assessment report, which was not yet published at the time of redaction of this thesis, was aimed to be released at the end of 2014. In this assessment report, the IPCC makes predictions about the future of climate change and global warming based on recent literature. They also assess the deviation between the present state of global warming and previous predictions. The IPCC made the prediction that for the global temperature not to increase by more than 2.0 to 2.4 °C, which is considered the agreed limit to avoid irreversible climate change, the average atmospheric CO_2 concentration should be kept under 400 ppm. Even with a sudden stop in man-produced CO_2, the global temperature is not expected to drop anytime in the course of the next centuries. This means that the present situation cannot be reversed but merely stopped. The rate at which the concentration of airborne CO_2 increases has been pretty steady since 1956 where the concentration has been measured monthly at the Mauna Loa Observatory in Hawaii (as shown in **Figure 1-1)** where it was measured at the time to be around 315 ppm which is already 35 ppm over the pre-industrial revolution value of 280 ppm. At the time of the Fourth Assessment Report the airborne concentration of CO_2 was measured to be around 380 ppm [1]. However, in May 2013 the airborne CO_2 concentration at the observatory was measured at 400 ppm, a 43 % increase from the pre-industrial concentration, for the first time in recorded history. This signifies that we are already at the position where the temperature is predicted to increase by the maximal amount that is considered safe [2], [3].

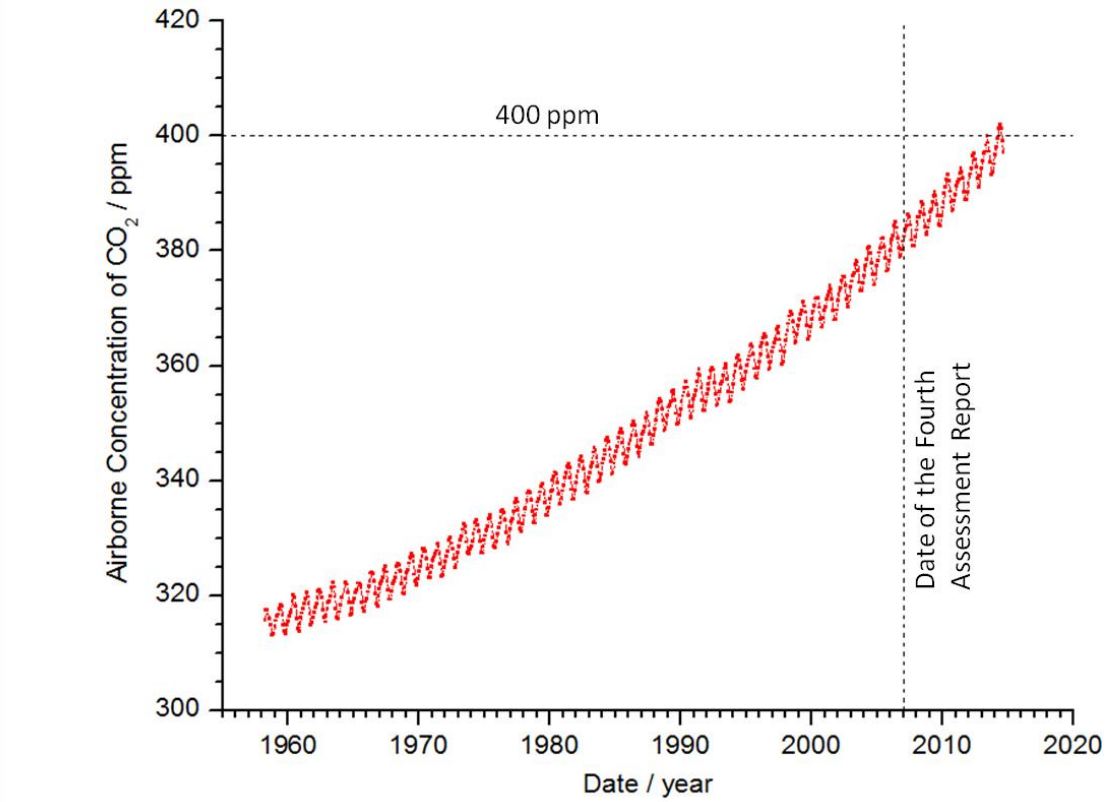

Figure 1-1: Airborne CO_2 concentration measured at the Mauna Loa observatory March 1958 to August 2011 [3]

In 2012 the worldwide production of CO_2 was approximately 9.7 ± 0.5 billion tonnes of carbon per year [4] whereas the estimated capacity of the earth's carbon sinks is 7.0 ± 1.6 billion tonnes per year meaning that between 0.6 and 4.8 billion tonnes of carbon remain airborne every year [5]. This data does not include the CO_2 released by the transformation of the landscape by humans for different purposes (intense agriculture, deforestation for urban expansion, recreational lands or/and fuel, etc.) which releases an additional estimated 1.2 billion tonnes of carbon per year [5]. A decrease in CO_2 production from the combustion of fossil fuel to an amount lower than the carbon sinks' capacity is of the outmost importance to mitigate the effect of greenhouse gases and global warming on the earth climate. In order to decrease our CO_2 production without suddenly reducing our energy consumption, which would have a large impact on the present economical state, new green energy sources need to be developed/perfected and implemented. We already have the technology to produce green energy by harvesting nature's resources such as hydropower, wind power, solar power, nuclear power, etc. However, all of these power sources have their drawbacks which prevent our divergence from fossil fuel. For example, wind and solar power have a very low output and massive infrastructures are needed to obtain large amount of power, hydropower requires the perfect geological location and has an immense impact on the surrounding ecosystem by flooding the upstream lands while nuclear energy is very controversial and the disposal of large amounts of radioactive material remains a problem. Additionally, while all of those are suitable to produce electricity for the grid they are not as efficient to supply energy to vehicles, portable application or secluded locations due to the poor power density of our current electricity storage technology compared to fossil fuels. As a matter of fact, fossil fuels currently supply 97 % of the world's energy consumed for transportation [6]–[8].

1.2 Alternative fuels

In view of the previous statements, the transfer from our reliance on fossil fuels to a greener, more efficient, practical and sustainable source of energy for those applications, which cannot depend on the stationary sources stated above, is imperative in order to stabilize the current airborne CO_2 concentration and avoid irreversible effects on the environment. A few alternatives have been considered amongst which fuel cells are one of the most promising candidates. As of now, most vehicles and secluded locations are powered by internal combustion engines (ICE) which has a typical break thermal efficiency of less than 20 % [9], [10], due to temperature constraints [11]. Operating with a theoretical power density of 12.3 kWh/kg for gasoline and 12.7 kWh/kg [12], [13]for diesel fuel the maximal power density that can be obtained is 2.6 kWh/kg in a conventional ICE. Portable application such as portable computer and cellular phones presently rely on electrical power supplied by batteries which can be obtained by green energy sources but has a very limited power density of 0.6 kWh/kg for state of the art lithium-ion batteries [6]. However, fuel cells can have efficiencies ranging from 40 to 60 % [10] with power densities of 33.3, 6.09 and 8.01 kWh/kg [13]–[17] when using hydrogen, methanol and ethanol as a fuel respectively which are the three most extensively studied potential fuels. **Table 1-1** presents the energy density by mass and by volume of different commonly used fuels. It also shows the price of fuels by units of energy where it can be observed that for fuels suitable for mobile application those extracted from crude oil still lead the way followed closely by ethanol and methanol while hydrogen is by far the most expensive fuel per amount of energy contained.

Table 1-1: Power densities and price per kWh of various common fuels

Fuel	Mass Density (kWh/kg)	Volumetric Density (kWh/L)	Cost (US$/kWh)	References
Gasoline	12.3	9.3	0.062[b]	[12], [13]
Diesel	12.7	10.6	0.055[b]	[13]
Hydrogen	33.3	1.23[a]	0.098[d]	[13], [17]
Methanol	6.09	4.82	0.079[c]	[14], [15]
Ethanol	8.01	6.31	0.072[b]	[15], [16]
Coal	5.6 – 8.3	4.8 – 7.1	0.011[b]	[12]
Natural Gas	15.3	----------	0.013[b]	[12]

a. Density of hydrogen at 700 bar [18].
b. Values obtained from NASDAQ for the month of October 2014.
c. Value obtained from Methanex for the month of October 2014.
d. Value obtained from the *Clean Cities Alternative Fuel Price Report* published by the *US Department of Energy* for the year 2013 [19].

Hydrogen fueled proton exchange membrane fuel cells (PEMFC) are the most mature type of fuel cells achieving reasonable power density to compete with current ICEs. Some commercial PEMFC systems are commercially available but the high prices of these units prevent their widespread distribution and restrain their use to specialised equipment. The major downside of the use of hydrogen as a fuel, beside the price of the fuel cell system, is its storage. While hydrogen has the highest gravimetric density of all non-nuclear fuels, its volumetric density is one of the lowest due to its gaseous form at ambient temperature which is only 1.23 kWh/L at a pressure of 700 bar [18] which is the current maximal safe pressure of operation of high pressure hydrogen cylinder. Also, liquefying hydrogen at temperatures of 20 K grants it a density of 71 g/L which is about 10 % of the volumetric density of gasoline or ethanol and provides only a power density of 2.36 kWh/L. On top of that, the theoretical energy required for the liquefaction of hydrogen from ambient temperature is 3.23 kWh/kg but the current liquefaction techniques require 15.2 kWh/kg [17] meaning that 46 % [13] of the contained energy needs to be used only to store the fuel. An alternative hydrogen storage system is to contain the fuel in hydrogen absorbing meta-based material, called metal hydrides, and release it when it is needed. This technique reduces the energy required for storage and solves the dangers linked to liquid/pressurized hydrogen. Metal hydrides have been shown to offer a hydrogen volumetric density of up to 115 g/L but with a gravimetric density reaching only a mere 3 % of the total mass [17]. The other large problem to the widespread availability of hydrogen is our current lack of distribution system and supply infrastructure. Indeed, our current distribution system is based on a liquid fuel which can be efficiently transported by land and by sea. Hydrogen on the other hand would require a totally different distribution system due to its low gravimetric density, gaseous form and explosive nature which would take time and considerable funds to be implemented.

The use of methanol in PEMFC solves the previous issues present with hydrogen as methanol has a relatively large volumetric density of 792 kg/m^3, a volumetric energy density of

4.82 kWh/L and is compatible with our current distribution system given a few modifications. Methanol is the smallest alcohol molecule and the only alcohol containing a single carbon atom. For this reason the reaction kinetics are quite fast and its conversion is complete with a high yield. Also, the aqueous form of the fuel removes the need of a complex humidification system to keep the membrane hydrated [6]. However, the high toxicity of methanol for humans prevents its widespread distribution. Therefore, various additional security systems would need to be developed and implemented in order to prevent contact between consumers and the product increasing the cost of the fuel and the equipment. While the use of either hydrogen or methanol as a fuel for fuel cells would greatly reduce the global amount of CO_2 produced by ICE due to their higher efficiency, both of these fuel are currently synthesized in most part from fossil fuels by steam reforming. Consequently, this solution does not solve the issue of eventual depletion of the fossil fuel reserves and a more sustainable solution is necessary.

Nowadays, ethanol is the fuel that attracts the most attention when it comes to fuel cells due to its high power density (31 % higher than methanol at 6.31 kWh/L), low toxicity, low fuel crossover (due to the larger size of the molecule) and its compatibility with the current fuel distribution system [20]–[22]. The biggest advantage of ethanol is that it can be produced on large scales by the fermentation of biomass with high sugar content such as corn (glucose) and sugar cane (sucrose) [7]. However, the idea of converting such important food sources to fuel has caused quite a commotion as the competition between the food and fuel industry will cause a shortage of the product bringing an increase of the prices of raw products. As food has been deemed more important than fuel, the fermentation of biomass using plant products containing no nutritive value for humans, such as corn cobs and stalks, sugar cane waste, straw, forestry and paper mill discards, has been developed to prevent interference with the food sector [7]. To do so the polysaccharides (starch and cellulose) are hydrolyzed to monosaccharides using enzymes (and acid for the latter). From there the fermentation process is the same as for glucose/fructose. Naturally, the complete electrooxidation of ethanol in fuel cells will produce two moles of CO_2 per mole of fuel but the biomass used to produce this fuel absorb through its growth an amount of CO_2 equal or higher than what is produced from the fuel by photosynthesis. This concept of a renewable fuel leads to a theoretically null CO_2 output which has the potential to reduce CO_2 emissions to a level lower than the carbon sinks capacities, by consequent slowing the increase of atmospheric CO_2 concentration.

Bioethanol/gasoline blends with concentrations between 15 and 85 % are already used in internal combustion engines in North America [19]. While being more renewable, this does not affect significantly the efficiency of internal combustion engines and the lower power density of ethanol requires more of the fuel for the same amount of energy meaning that the costs and emissions related to the transportation of the fuel will also increase. However, by feeding 100 % bio-ethanol to highly efficient direct ethanol fuel cell (DEFC) in order to replace ICE the amount of fuel needed per unit of power output would be reduced and, in consequence, decreasing the price of the fuel per amount of usable energy. While this green and efficient technology is very attractive, there are still various problems to overcome before commercialization.

1.3 State of the technology

Since the development of the proton exchange membrane (PEM) Nafion by Dupont in the 1960's, the benefits of having a solid electrolyte, such as a reduced thickness of the electrolyte, no carbonate deposition [23] and a simpler design that do not need to contain a liquid electrolyte without leaking, have revived the interest in fuel cells. Nafion is still, to date, the PEM with the highest ionic conductivity and is commonly used in hydrogen, methanol and ethanol fuel cells. However, in this acidic fuel cell environment the only catalyst that is stable enough to be of any practical use is platinum. The high price and low availability of the catalyst increases the cost of production of the units to a point where it is not competitive with current ICE. In the last decades, the syntheses of solid anion exchange membranes (AEM) have brought the attention of scientists around the world to the potential of alkaline fuel cell (AFC) [24]. Various problems arising when using a PEMFC can be mitigated by operating in an alkaline environment using an AEM. First, the range of catalysts that can be used for ethanol oxidation becomes much larger. Indeed, Shen et al. [25], [26] have shown in their studies that Pd can have an activity up to 50 % higher than Pt as the anode catalyst for the ethanol oxidation reaction (EOR) when a fuel cell operates in an alkaline environment. Also, the faster kinetics of the oxygen reduction reaction (ORR) in an alkaline environment allows the use of non-noble metal as cathode catalysts such as Ni and Ag [24], [27]. This modification of the catalysts on both sides of the membrane electrode assembly (MEA) reduces the costs of production by a significant amount. The less corrosive environment of AFC also ensures a potentially greater longevity of the different fuel cell components leading to reduced maintenance costs. The reverse ionic flow, now from the cathode to the anode, provides an osmotic drag towards the anode reducing the fuel crossover through the membrane which would reduce the output potential difference. There is also no need for a complex water management system due to the fact that water is produced at the anode which contains an aqueous solution instead of at the cathode where there is a gaseous phase [24], [28]. While some problems are mitigated when operating in an alkaline environment there is still an important drawback in the DEFC technology present in both media which is the cleavage in the C-C bond in the ethanol molecule. As of now, even the state of the art catalysts result mainly in the production of acetaldehyde and acetic acid producing 2 and 4 electrons per molecule of ethanol following **Eq. 1.1**and **1.2** [29], [30] **i**nstead of the theoretical 12 electrons available [15], [31], [32]. Unless this problem is solved it is impossible to commercialize this technology. For these reasons, this research will focus on the development of highly active catalyst for the EOR in alkaline medium.

$$CH_3CH_2OH \rightarrow CH_3CHO + 2H^+ + 2e^- \tag{1.1}$$

$$CH_3CH_2OH\ +\ H_2O \rightarrow CH_3COOH + 4H^+ + 4e^- \tag{1.2}$$

It is now known that many catalyst variables can be modified to increase their catalytic activity towards the EOR. First, physical characteristics such as particle sizes, shapes and surface plane orientation can be manipulated to offer optimal reaction sites for the oxidation of the desired molecule. This effect is caused by the modification of the binding energy of the reagents, products and/or intermediates by a change in the inter-atomic distance of the catalysts surface atoms in small nanoparticles (< 10 nm) which was attributed to surface stress [34]–[37] or by the difference in atomic spacing on different surface planes. The dispersion and the size of nanoparticles on the surface of the support also have an effect on the mass activity of the catalyst. A higher dispersion, meaning reducing the amount of agglomeration of the catalysts particle and the portion of their surface in contact with the support, increases the amount of catalyst surface fraction available for the reaction per unit of mass [34]. This is also true for smaller particles which will have a larger fraction of their atoms on the surface of the clusters increasing the amount of reaction site available per mass of metal as shown in **Figure 1-2**. Properties of the catalyst, other than its morphological structure, such as the chemical composition of a catalyst can also affect its catalytic activity. The degree of oxidation of a metal catalyst can be varied, a metal oxide can be doped by hetero-atoms to modify its ionic/electronic conductivity, bandgap and Fermi level, metals can be alloyed or bi-phase systems can be formed. All of these modifications can have an effect on the activity of a catalyst for a given reaction due to different effects. The adsorption strength of different reagents on a catalyst will be modified with a change in the electron density of the catalyst caused by a lower binding energy of the electrons with the atom nucleus. The doping of a metal oxide creates a stoichiometric instability causing a change in conductivity and creating oxygen vacancies which can act as highly active reaction sites. In a bi-phase material two reagents can attached preferably on different material causing an increase in activity for sites situated at the 3-phase boundary due to faster adsorption of both reagents on the different surfaces.

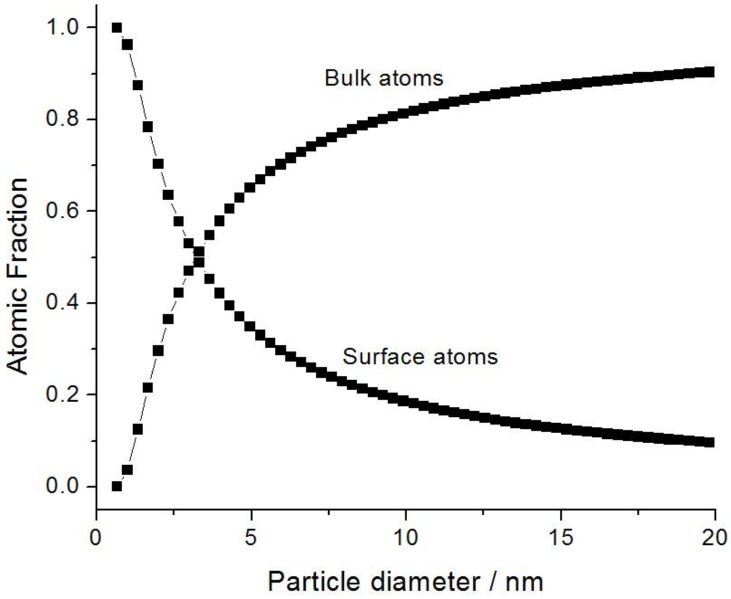

Figure 1-2: Calculated surface to bulk ratios for solid metal particles vs diameter [33]

Another modification that has an important effect on the catalyst activity is the material used to support the catalyst particles. Generally catalyst nanoparticles are deposited on the surface of carbon black due to its high specific surface area (a_S), its wide availability, its high electronic conductivity and its low price. However, it is now known that the use of other support for metal catalysts could improve their activity compared to carbon black. One type of support that can increase the mass activity of the metal catalyst is graphene and other carbon monolayer configurations. This increase in mass activity is caused by an increase in a_s increasing the dispersion of nanoparticles on the surface of the support leading to a larger utilisation. Another type material that promoted the catalytic activity of metal catalysts is metal oxides. Generally, the promotional effect of metal oxides is attributed to two mechanisms. First, oxygenated species adsorbed on the metal oxide surface at the metal-support interface are known to accelerate the oxidation of neighbouring carbonaceous species. Secondly, the electron density of the catalyst can be modified by contact with the support causing a modification in the adsorption energy of organic species on the metallic surface.

1.4 Layout

Chapter 2 contains an overview of the recent studies on the subject of alcohol electrooxidation for use in fuel cells. In a first part are recent advances in catalysts development using carbon-based supports for the EOR in alkaline media including: Pt-based catalysts, Pd-based catalysts and alternate catalysts. The results obtained from testing those catalysts in direct alkaline ethanol fuel cell (DAEFC) are also displayed. In a second part is a summary of research made using metal oxides as support/co-support for metal catalysts toward the oxidation of light alcohols and of the promoting effect observed. In a third part is discussed the promotional effect, when used as a support, of two novel catalysts (titanium dioxide nanotubes (TiO_2-nts) and graphene) for light alcohol oxidation. This is followed by a brief discussion on recent literature concerning the development of cathode catalysts for oxygen reduction and of highly conductive AEM for AFCs.

In **Chapter 3** Pd nanoparticles are synthesized in-situ on the surface of different metal-oxide supports using a simple metallic ions reduction method with $NaBH_4$ as the reducing agent. The as synthesized nanoparticles are characterized using X-ray diffraction (XRD), transmission electron microscopy (TEM) and X-ray photoelectron spectroscopy (XPS). Their electrochemical active surface area (ECSA) is calculated using CO stripping and their ethanol oxidation potential normalized by the found surface area to compare the activity of each catalytic surface and the effect of the support on the EOR.

In **Chapter 4** TiO_2-nts are electrochemically grown by anodization on the surface of a thin Ti film. Different loadings of Pd nanoparticles are grown on the surface of the TiO_2-nts using an atomic layer deposition (ALD) method to obtain a large surface area and an even distribution. The physical and electrical properties of the as grown TiO_2-nts were modified by annealing the nanotubes in order to observe their effects on the electrocatalytic behaviour of the Pd nanoparticles for the EOR. In this study the ECSA was found using the PdO reduction region of the cyclic voltammograms (CV) in electrolyte.

In **Chapter 5** TiO_2-nts are synthesized using the same method as in the previous chapter but are modified by the addition of a thin SnO_2 layer deposited by ALD on the surface of both as grown and annealed TiO_2-nts. Different Pd loadings were deposited on the surface of the synthesized supports and their morphologies are assessed by electronic and atomic force microscopy. Their catalytic activities towards the EOR are compared using the surface area found using PdO reduction.

Chapter 6 is a study made on the EOR potential of Pd and PdNi with different Ni contents nanoparticles deposited on the surface of sulphonated graphene (sG) compared to that of Pd on carbon black. The dispersion of the Pd and PdNi nanoparticles is assessed using electron microscopy on both supports. The catalytic activities of the catalysts are compared using the ECSA found by CO stripping measurements.

Chapter 7 is a continuation of the research made in **Chapter 3** where the best catalyst of the latter is tested in a DAEFC purposefully built for this research. In this chapter is explained the design and layout of the fabricated triode fuel cell. Pd/TiO_2 nanocatalyst is tested in the fuel cell using ethanol in an alkaline media and an AEM supplied by Fumatech.

Chapter 8 restate the conclusions found in the previous result chapters concerning the effects of the supports and of the addition of Ni on the activities of the electrocatalysts for the EOR. It explains briefly the causes of the promotion of the catalytic activities through metal-support interaction and the geometry of the catalytic systems.

Chapter 2 : Literature Review

2.1 Introduction

The aim of this chapter is to present the current state of the technology concerning ethanol oxidation in alkaline solution for its use in direct ethanol fuel cells (DEFC). In a first part, a review of the recent developments in anode catalysts for ethanol electrooxidation in alkaline environment is made. This review is separated in subcategories such as Pt-based, Pd-based and non-noble metal based catalysts followed by a description of the proposed oxidation mechanism and the performance obtained from direct alkaline ethanol fuel cells (DAEFC). Also, the effect of the type of support used for the catalyst on their activity for the ethanol oxidation reaction (EOR) is made using various recent publications concerning the addition of metal oxides to the support. In a second part, the development of Pt and non Pt-based catalyst for oxygen reduction at the cathode is assessed. Lastly, a short review of the different types of anion exchange membrane (AEM) developed in laboratory and commercially available is made along with their performance concerning ionic transport.

2.2 Anode Catalyst

The anode catalyst is the most limiting factor in the power output of fuel cells due to the incomplete oxidation of ethanol to acetaldehyde and acetic acid following the reactions shown in **Eq. 1.1 and 1.2**, respectively, yielding only a fraction of the theoretically available 12 electrons per molecule obtained from complete oxidation [31], [32] following **Eq. 2.1** [29]. Most modern catalysts for ethanol electrooxidation are Pt-based which brings a few problems. First, Pt is easily poisoned by strongly adsorbed oxidation intermediates blocking ethanol reaction sites. Secondly, Pt is a very expensive and scarce metal which increases the cost of potential fuel cells. For these reasons, the scientific community focussed on the development of low Pt loading or Pt-free catalysts for ethanol electrooxidation.

$$CH_3CH_2OH + 3H_2O \rightarrow 2CO_2 + 12H^+ + 12e^- \qquad 2.1$$

2.2.1 Carbon Supported Catalysts for Ethanol Electrooxidation in Alkaline Media

The ethanol electrooxidation kinetics were shown to be faster in an alkaline media than in an acidic media. Also, the use of a basic environment opens up the possibility to use non-noble, less expensive, metal catalysts for this process. The recent development of anion conducting membrane with high ionic conductivity has promoted this field of research.

2.2.1.1 Carbon Supported Pt and Pd-Based Catalysts

As in acidic media, Pt is still very active for the EOR in alkaline media. In order to reduce the amount of precious metal in the catalyst, the structure of the Pt nanoparticles can be altered to offer optimal reaction rates with as small an amount of Pt as possible. It is in this scope, that Stanley et al. [38] observed the electrodes behaviours for the EOR in alkaline media of preferably oriented Pt (111), (15 15 14), (554), (553) and (110). They have shown that increasing the amount of steps on the terraces planes going from Pt (111) to Pt (110) lowers the onset potential of the EOR by about 200 mV showing the importance of low coordinated atoms. They have also observed a significant increase in electrode stability with an increasing number of steps along with a modification of the main adsorbed molecules on the catalysts' surface. For large terraces Pt (111) the molecules adsorbed on the surface were CH_x while the main poisoning specie on the stepped surface Pt (110) was CO_{ads} showing that the EOR was more complete on stepped surfaces.

While Pt is almost the only option in acidic media, in alkaline media it is possible to use a much larger variety of material due to a less corrosive environment and faster ethanol oxidation kinetics. Notably, many studies have shown that Pd had a higher activity towards the EOR in alkaline media than commercial Pt/C [25], [26], [39]–[45]. Amongst others, Fengping et al. [25] and Xu et al. [26] have shown that Pd-NiO/C shows an activity for the EOR between 30 and 100 % higher than Pt-NiO/C. Also, various modifications of the catalytic system such as: a modification of the carbon support structure [26], [30], [41], [46], a modification of the bulk structure of the catalyst nanoparticles by formation of alloys [39], [42], [44]–[49] and the surface morphologies of the nanoparticles [16], [43] can influence significantly their catalytic activity for the EOR.

The most common catalyst support for the EOR is carbon black which has a very high a_s and a low cost. However, by modifying the structure of the carbon support it is possible to influence the catalytic activity of the supported catalyst. In a study conducted by Xu et al. [40] Pd and Pt nanoparticles were synthesized on the surface of both carbon black and carbon microspheres (CMS) by metallic ion reduction using $NaBH_4$ as the reducing agent. The CMS were synthesized using a hydrothermal method which resulted in spherical carbon particles with diameters ranging from 1 to 2 μm. It was calculated that the ECSA for both types of nanoparticles deposited on CMS was about twice as much as their carbon black-deposited counterparts. The current density by ECSA of the Pd catalysts was shown to be 4 to 5 times higher than the current density for the Pt particles deposited on carbon black and CMS, respectively. Also, the current density of the nanoparticles deposited on CMS showed a 71 and 140 % increase over those on carbon black for Pt and Pd respectively. This increase in activity is attributed to the larger dispersion and smaller size (as measured by X-ray diffraction (XRD)) of the nanoparticles deposited on CMS and to the facility of the solution to diffuse to a larger three-phase boundary where OH^- groups can be supplied from the support to oxidize adsorbed ethanol molecules.

Another study conducted by Zheng et al. [41] compares the activity of Pd nanoparticles deposited on various carbon supports via intermittent microwave heating. The three different carbon supports used were: multiwall carbon nanotubes (MWCNTs), activated carbon fiber (ACF) and carbon black. This study shows an increase in catalytic activity for the nanoparticles deposited on the carbon supports following the order: ACF < carbon black < MWCNTs with the stability of the catalysts following the same trend. The onset potential of the EOR was found to be 100 mV more negative on MWCNTs than on carbon black. They have also shown that Pd/C had a current density around twice as high as that of commercial Pt/C. However, no explanation as to why the catalytic properties of Pd are enhanced when deposited on MWCNTs is offered.

Two different research groups have studied the activity of Pd and PdNi alloys deposited on the surface of different types of carbon nanofibers (CNFs). In a first place, Maiyalagan et al. [46] have synthesized Pd:Ni (3:1) nanoparticles on the surface of CNFs using the metallic ion reduction method with $NaBH_4$ as the reducing agent. They observed a negative shift of 200 mV for the onset of the EOR on the PdNi/CNFs compared to Pd/C synthesized using the same method. An increase in current density by a factor of 4 was also observed for the nanoparticles deposited on CNFs. Their study has also shown a significantly higher current density for PdNi/CNFs under an applied potential of -0.5 V for 30 min. The increased catalytic activity is in part attributed to the better dispersion of the catalyst nanoparticles on the surface of the support. In a second part, Qin et al. [30] have deposited Pd nanoparticles using pulse electrodeposition technique on the surface of different types of CNFs synthesized in their laboratory. The three different types of CNFs were platelet CNFs (p-CNFs), fish-bone CNFs (f-CNFs) and tubular CNFs (t-CNFs) for which the graphite sheets have different orientations in relation to the fiber axis. This difference influences the ratio of the number of edge to basal atoms on the surface of the nanofibers. It is shown using Raman spectroscopy that the p-CNFs have a higher number of edge atoms on the surface while t-CNFs has the lowest with f-CNFs being somewhere in the middle. They show using TEM that the dispersion of nanoparticles on edge atoms is more uniform while a higher amount of agglomeration appears with a higher number of basal atoms. They have shown that the activities for the EOR of the synthesized catalysts could be enhanced by more than 20 % by increasing the amount of edge atoms on the surface of the carbon support. However, no effect of the structure of the carbon support on the position of the EOR onset potential has been reported.

The morphological effect of the Pd structure can also have an important effect on the activity of the catalyst for the EOR due to the difference in the crystal planes exposed and to an increase in exposed surface area. Two different studies have shown an increase in catalytic activity of Pd towards the EOR by changing its morphology. First, Carrera-Cerritos et al. [16] have synthesized (using a modified polyol method) Pd nanoparticles of different shapes deposited on carbon black giving then preferential plane orientation. Their study have shown that the Pd nanobars having a larger fraction of (100) facets offer the higher activity towards the EOR with Pd nanoparticles having a higher amount of (111) facets lead to the lowest activity. This higher activity for Pd nanobars is explained by a stronger ethanol-Pd bond on (100) planes bringing down the energy barrier for dissociation. In a second study conducted by Wang et al. [43] unsupported, highly ordered, nanowire arrays were synthesized using an anodised alumina template and tested for the EOR. The synthesized nanowires have an approximate length of

800 nm with an average wire diameter of 80 nm. The activity of this catalyst is compared to the activity of a Pd film and to commercial PtRu/C catalyst (E-TEK). They have calculated that the ECSA per amount of Pd was 14 times higher on Pd nanowires than on the Pd film due to its extensive 3D structure. They found that the current density of Pd nanowires was 7 times higher than on Pd film and more than 1.5 times higher than commercial PtRu/C. The study reported a negative shift of 170 mV for the EOR onset potential for Pd nanowires compared to Pd film and a good stability of Pd nanowires in the operating media. This increase in current density is explained by an easy diffusion of the ethanol in the catalyst layer and of products out of the catalyst layer increasing the reagent concentration at the liquid-catalyst interface by reducing the liquid sealing effect.

Many studies have observed the effect of the addition of another metal either as the formation of an alloy, of a biphase material or as a co-support on the activity of Pd on the EOR. Various metals such as: Ni [46], [47], [49], Au [39], [45], [48], Ru [42], [44], Sn [44], [45] have been considered, studied and their results published.

Different studies have shown [46], [47], [49] that the addition of Ni to Pd during its synthesis could improve the nanoparticles catalytic properties for the EOR. In general, these studies have attributed the promotional effect of Ni to the formation of NiOOH species at the metal-support interface where the hydroxyl group could be supplied to neighbouring adsorbed organic species on Pd surfaces to facilitate its oxidation and reduce catalyst poisoning. These studies propose that the optimal Ni loading for the activity of the catalysts towards the EOR would be between 25 and 60 metallic wt%. Ni has also shown to have a promotional effect on the electrooxidation of methanol and ethanol on Pt based nanocatalysts [50]–[53].

Zhang et al. [47] synthesized Pd-Ni/C catalysts using a modified solution phase-based nanocapsule method with various Pd:Ni ratios and one sample of PdNi/C Pd:Ni (1:1) using the metallic ion reduction method using $NaBH_4$ as a reducing agent. The synthesized samples were also compared to Pd/C synthesized using the first method. XRD analysis revealed that the PdNi nanoparticles had a higher degree of alloying when synthesized by the use of $NaBH_4$ which was characterized by a shift in the Pd (111) peak. They have shown an increase in Pd mass activity with increasing Ni content up to a Pd:Ni ratio of 1:1 after which a sharp decrease in activity was observed. The onset potential for the EOR was shifted by about 100 mV towards lower potential for samples containing the optimal Ni content. While PdNi/C synthesized using $NaBH_4$ has a higher mass activity than Pd/C it was observed that the other synthesis methods yield much higher activity per ECSA. They propose that the nanocapsule synthesis method facilitates the formation of better contacts between Ni and Pd promoting the oxidation of adsorbed species on the Pd surface with neighbouring NiOOH sites.

In another study conducted by Maiyalagan et al. [46], for which the carbon support effect was discussed previously, PdNi/CNFs were synthesized using a Pd:Ni ratio of 3:1 for ethanol electrooxidation. They have shown that PdNi/CNFs have an activity higher than Pd/C by a factor of 4 and a significantly higher current density after prolonged operation. The decrease of the onset potential by 200 mV for the sample containing Ni is also attributed to the presence of NiOOH sites on the surface of the catalyst which promotes the oxidation of ethanol and adsorbed intermediates on the surface of Pd.

Shen et al. [49] have tested the catalytic activity of co-deposited PdNi catalysts on carbon synthesized by ionic reduction using $NaBH_4$ towards the EOR. The Ni content of the catalyst was varied between 0 and 72 atomic % on a metal basis. They have shown by cyclic voltammetry that the catalyst with a Ni content of 60 atomic % showed the highest current density and the best steady-state current at almost twice the value obtained from Pd/C. By X-ray photoelectron spectroscopy (XPS) and XRD they have confirmed the presence Ni in various chemical states including Ni_M, NiO, NiOOH and $Ni(OH)_2$. It is proposed that these Ni phases would promote the EOR by supplying the hydroxyl group needed for the oxidation of adsorbed organic species on Pd surfaces.

Ru has shown to improve the catalytic activity of Pt in acidic media by increasing its resistance towards the poisoning of the catalyst surface by strongly adsorbed carbonaceous species. A study conducted by Yougui et al. [42] have synthesized PdRu/C nanoparticles using an aqueous impregnation method with a theoretical Pd:Ru ratio varying between 1:0 and 1:2. They have shown that the activity for the EOR of PdRu/C 1:1 was 4 times higher than that of PtRu/C 1:1 for potential between 0.3 and 0.4 V vs mercury/mercury sulphate electrode (MSE) while the current density for Pd/C in this range is still zero. Following this observation, it was observed that the onset potential of the EOR was shifted by about 250 mV towards lower potential on PdRu/C compared to Pd/C. This increase in catalytic activity is explained by a mechanism similar to that observed on PtRu catalysts where the Pt atoms catalyse the dissociative adsorption of ethanol while the Ru promotes this reaction by catalysing the dissociative adsorption of water molecules providing hydroxyl groups at a lower potential.

Other metals such as Sn and Au have been studied as an addition to Pd in order to increase its catalytic activity for the ethanol electrooxidation. A study made by Modibedi et al. [44] study the catalytic activity towards the EOR of the binary and tertiary systems PdSn and PdRuSn deposited on carbon black. The nanocatalysts were synthesized using a chemical reduction reaction using $NaBH_4$ as a reducing agent in a mixed aqueous/organic (ethylene glycol) solution. The PdRuSn/C was also prepared using a two step reduction method with only Pd being reduced on the surface of RuSn nanoparticles, prepared in a first reduction, in the second step. It is shown that the co-reduction of the 3 metals shows a much smaller activity for the EOR than the two steps reduction. Both binary and tertiary systems show and increased in catalytic activity compared to Pd/C and to commercial PtRu/C 1:1. While the tertiary system shows a significantly lower onset potential, the high poisoning of CO, the lower current density at more positive potential and a lower stability shows that PdSn/C 2.5:1 is the best catalyst for the EOR.

He et al. [54] made a comparative study between the activity of a commercial Pt/C catalyst, of Pd_4Au_1/C and $Pd_{2.5}Sn/C$ for the EOR in alkaline media. The nanocatalysts were synthesized via the metallic ion reduction method using $NaBH_4$ in aqueous solution. In this study, the onset potential of commercial Pt/C was seen to be almost 200 mV lower than for the other catalysts for which the current densities were higher at more anodic potentials. However, chronoamperometry experiments have shown that for long term application the decay of the activity of commercial Pt/C was higher than that of the other Pd based samples which were conserving higher current densities after prolonged periods showing an increased tolerance towards CO poisoning. It is shown that Pd_4Au_1/C has a very similar activity for the EOR than $Pd_{2.5}Sn_1/C$ with a slightly lower onset potential and a higher current density during long term operation. On their side, Zhu et al. [48] have tested a different configuration of PdAu/C by depositing between a sub-monolayer of Pd and a few layers by epitaxial growth on the surface of Au nanoparticles synthesized using the metallic ion reduction method with $NaBH_4$. The PdAu nanoparticles were deposited on carbon black with a nominal loading of 20 metal wt%. Different Pd loadings were synthesized in order to obtain Au coverage between 0 and 100 %+. It can be observed that the highest activity was showed for the Pd/Au particles with a ratio of 1:4 for which the coverage was calculated to be slightly less than a full monolayer. This higher activity is explained by a catalytic promotion effect reducing the poisoning effect of CO on the surface of the catalyst. At higher coverage, the low amount of surface Au atoms limits this promoting effect to the low amount of Pd-Au interfaces while at lower loadings the small Pd islands are to small and sparse to form the continuous Pd plane necessary for ethanol oxidation.

Ag is another metal that was tested for its activity for the EOR when combined with Pd. Indeed, Nguyen et al. [39] have alloyed Pd with Ag to form nanoparticles using a co-reduction method in aqueous solution using $NaBH_4$. The Pd:Ag ratio was varied between (2:1) and (1:2.5) while the Pd loading on carbon was kept steady at 10 wt%. The formation of an alloy between Pd and Ag was confirmed by an augmentation of the lattice parameter compared to pure Pd calculated by the XRD peak position. This study shows that Pd_1Ag_1/C has the highest activity of all the catalysts (3.5 times higher than both Pd/C and Pt/C) with further increase in Ag loading bringing a decrease in catalytic activity while all the samples containing Ag are still more active than both Pd/C and Pt/C synthesized using the same method. They also showed that the onset potential of the EOR was lowered by 200 mV on Pd_1Ag_1/C compared to Pd/C and Pt/C with different Ag loadings having a lessened effect. This higher activity is explained by a higher coverage of the catalyst surface by OH^- at lower potential promoting the EOR and to the supply of the hydroxyl species to neighbouring Pd sites at higher potential.

In summary, Pd has shown to be a promising catalyst to replace Pt as the conventional catalyst in alkaline fuel cell due to its high catalytic activity and wider availability. We have seen that many modifications of the catalytic system can promote the catalytic properties of Pd nanoparticles. The type of carbon support (CNF and CMS instead of carbon black) used for Pd nanoparticles has shown to promote its catalytic activity. The surface configuration of the Pd nanoparticles also has an effect on the oxidation rate of ethanol on its surface due to a modification of the adsorption strength of the molecules with the (100) facet having the best surface reaction rate. The creation of alloys and bi-phase materials also shown to cause an increase in catalytic activity of Pd nanoparticles due to a supply of OH^- species at lower potential for the oxidation of ethanol molecules.

2.2.1.2 Alternate Metal Catalysts

Numerous attempts at the development highly active catalytic systems Pt and Pd-free for the EOR in alkaline media were made [42], [55]–[57]. In general the proposed catalyst had a non-negligible activity for the EOR without reaching the catalytic potential of Pt and Pd. In a study discussed earlier, Yougui et al. [42] have tested the activity of Au/C and AuRu/C (an atomic ratio of Ag:Ru of 1:1), synthesized using the method discussed above, for the EOR. For these catalysts, the onset potential was about 0.6 V vs RHE which is 200 mV higher than for their sample of Pd/C. After the onset potential the current density stays very low until 0.9 V vs RHE is reached. The addition of Ru to Au does not influence the onset potential but increases significantly the activity of the catalyst at higher potential suggesting that the EOR is limited by the slow dissociative adsorption of ethanol on the Au surface. In order to create a good Pt/Pd-less catalyst for the EOR they suggest the use of a metal having low hydrogen oxidation overpotential along with a material providing oxygenated species such as Ru.

Following this suggestion, a few research groups have synthesized Ni-based materials that were tested for the EOR in alkaline media. Amongst others, Tarasevich et al. [55] have synthesized RuNi/C 15 wt% nanoparticles containing between 37 and 100 % of Ru on a metal basis using ultrasonication of metallic ions in an aqueous/alcohol solution. The onset potentials, observed for the EOR were found to be comparable to those of Pt and Pd with the current density at higher potential being significantly lower. The lowest onset potential was found for the sample containing a Ru:Ni ratio of 77:23. The fact that such a low onset potential was obtained for a material completely free of Pt and Pd suggests that further development of Ni and Ru based catalysts could lead to competing commercial catalysts.

Kim et al. [56], [57] have conducted two independent study concerning the EOR on unsupported Ni-based electrode with the addition of different materials. In a first study [57], they have modified Ni and Ti wires by thermal decomposition of $RuCl_3$ to obtain RuO_2 modified electrodes. While the activities of the Ti based catalysts were almost zero, the RuO_2 coated Ni electrode has a much higher activity than the bare Ni wire. The stability of the catalyst in highly alkaline concentration was low, a problem that was attributed to the degradation of the RuO_2 layer at high OH^- concentrations. The increase in activity caused by the addition of the RuO_2 layer was proposed to be caused by the ability of the Ru oxide layer to change its oxidation state releasing electrons creating various Ni oxide species (Ni(OH)/NiOOH) increasing the catalyst activity for the EOR. The other study [56] was made by the co-electrodeposition of various Ni-based ionic mixture. The theoretical samples produced in this study were $Ni_{99}Na_1$, $Ni_{89}Co_{10}Na_1$, $Ni_{98}Ru_1Na_1$ and $Ni_{88}Co_{10}Ru_1Na_1$. They show that the NiCoRuNa electrode is potentially the best electrode for the EOR as the addition of Co can be seen to increase the current density due to its transformation to higher valence state oxide than 4+ while the addition of Ru also shows an increase in current density and reduces the onset. The enhanced properties of the electrode are attributed by increased Co and Ru oxidation state caused by the electro-generated nickel oxides.

In summary, Ni-based catalysts have shown to be the best contenders to Pt and Pd-based catalyst for ethanol oxidation in alkaline media. The addition of a reducible material to the Ni catalyst has shown to promote the formation of NiOOH species facilitating the oxidation of adsorbed carbonaceous molecules. However, while it is a promising material, the currently high overpotential does not make it competitive to Pt and Pd-based catalysts.

2.2.1.3 Proposed Mechanisms

Very few studies have addressed the mechanism of ethanol complete electrooxidation due to its complexity and generally incomplete oxidation. However, the oxidation mechanism to acetaldehyde and acetic acid is better known and generally accepted. A study of the composition of the products and intermediates of an ethanol fuel cell was made by Paik et al. [20] showing a wide variety of products ranging from CO_2 and simple C_1 molecules such as formic acid and methanol to complex molecules such as C_2 radicals and ethers showing the oxidation of ethanol follows a very complex mechanism formed of various reaction paths. It is generally accepted that the oxidation of ethanol in alkaline media starts with the formation of either a CH_3CHO_{ads} specie on the path to acetaldehyde or a strongly adsorbed ethoxy molecules on the surface of the Pd after the adsorption of ethanol following **Eq. 2.2 and 2.3** and **Eq. 2.2 and 2.4** [58], [59] respectively. The oxidation of this ethoxy molecule following **Eq. 2.5 and 2.6** is thought to be the rate limiting step of ethanol electrooxidation rather than the dissociative adsorption of ethanol [24]. The oxidation of the ethoxy molecule is followed by the desorption of the adsorbed molecule in a non-rate limiting step represented by **Eq. 2.7** [59].

$$\boldsymbol{Pd + CH_3CH_2OH \rightarrow Pd - CH_3CH_2OH_{ads}} \qquad \textbf{2.2}$$

$$\boldsymbol{Pd - CH_3CH_2OH_{ads} + 2OH^- \rightarrow Pd + CH_3CHO + 2H_2O + 2e^-} \qquad \textbf{2.3}$$

$$\boldsymbol{Pd - CH_3CH_2OH_{ads} + 3OH^- \rightarrow Pd - CH_3CO_{ads} + 3H_2O + 3e^-} \qquad \textbf{2.4}$$

$$\boldsymbol{Pd + OH^- \rightarrow Pd - OH_{ads} + e^-} \qquad \textbf{2.5}$$

$$Pd - CH_3CO_{ads} + Pd - OH_{ads} \rightarrow Pd - CH_3COOH_{ads} \qquad \textbf{2.6}$$

$$Pd - CH_3COOH_{ads} + OH^- \rightarrow Pd + CH_3COO^- + H_2O \qquad \textbf{2.7}$$

2.2.1.4 Tests in Fuel Cells

Various research groups have studied the behaviour of various Pt and Pd-based commercial and synthesized catalysts using different AEM in DAEFCs. These results are often compared to results of the same or similar catalyst operating in a comparable acidic environment with an appropriate cation exchange membrane (CEM) and their power output are found to be comparable, if not superior. Even though Pd has been shown to be more active, more stable and less prone to poisoning, Pt is still widely used in the development of highly efficient DAEFC.

A study conducted by Santasalo-Aarnio et al. [60] shows the results obtained by a direct alkaline alcohol fuel cell (DAAFC) operating using methanol, ethanol and iso-propanol using a commercial Fumasep FAA-2 from Fumatech Company and the results are compared to the same fuel cell operating in acidic media with a Nafion 115 membrane. The anode catalyst for this experiment was a commercial PtRu/C catalyst while the cathode catalyst was Pt/C operating under a pure oxygen environment both with a metal loading of 1 mgcm^{-2}. By varying the fuel concentration at the anode it was found that a molar ratio of 1:1 would provide the highest current density in both media. They found that the operation of the fuel cell under atmospheric conditions would yield a power density of 0.45 mWcm^{-2} in alkaline media while a higher power density of 3.8 mWcm^{-2} was obtained in an acidic environment. These results shows that such a membrane in alkaline media does not allow to obtain a current competing those obtained using Nafion membranes.

Another study made by Fujiwara et al. [61] have tested commercial unsupported PtRu black and Pt black nanoparticles in a ADEFC using a research grade AEM from Tokuyama Corporation with a metal loading of 3 mgcm^{-2} for each electrode. The power densities observed were compared to the same setup using a Nafion 117 CEM in acidic media. The overpotentials of the reactions on both sides of the membrane were reduced when operating in an alkaline environment showing that both reactions were favored. A high current density of 58 mWcm^{-2} was observed under ambient conditions, humidified oxygen and a fuel concentration of 0.5M KOH + 1M ethanol for the setup operating in alkaline media while a much smaller power density of 6 mWcm^{-2} is observed under acidic operation with the same operating conditions. The exhaust products were analysed and it was shown that the main product of fuel cell operation in alkaline media was acetic acid while a ratio of about 1:1 was found for acetaldehyde and acetic acid in the fuel cell using a CEM showing that the 4 electrons pathway is favored in an alkaline media.

There are other options than using commercial AEM for DAEFC tests as it was shown by this group [62] who used a synthesized KOH doped polybenzimidazole (PBI) membrane. The synthesized membrane was found to have an ionic conductivity of 0.2 times that of Nafion with low ethanol permeability. This membrane was tested using a PtRu/C 45 wt % with a Pt:Ru ratio of 2:1 as the anode catalyst and Pt/C 20 wt% as the cathode catalyst. The power densities obtained in this study were 49 and 61 mWcm^{-2} for the fuel cell operating at temperatures of 75 and 90°C respectively with a fuel concentration of 2 M KOH + 2 M ethanol while pure O_2 at 2 bars was fed at the cathode.

A few other research groups such as [63] have tested Pd catalysts in DAEFC instead of the highly popular Pt. In this study, Pd nanoparticles were deposited on MWCNTs which were used as the anode catalyst for the electrooxidation of methanol, ethanol and glycerol. The membrane used for these test was supplied by Tokuyama Corporation while the cathode catalyst was a Fe-Co HYPERMEC^{TM} catalyst. They show that the synthesized catalyst is more active for ethanol oxidation with a lower onset potential than for the other fuels. They observed a power density output of 72 mWcm^{-2} for the DAEFC at a temperature of 80°C with a fuel concentration of 2 M KOH and 10 wt% ethanol. They also observed, as in a study discussed earlier [61], that the main product of ethanol oxidation was acetic acid providing a higher power density than the oxidation to acetaldehyde. Another Pd based catalyst was synthesized and tested by Shen et al. [49] using the same membrane and cathode catalyst. On their side, they have synthesized Pd/C and PdNi/C nanoparticle with ratios of Pd:Ni varying between 1:1 and 2:5 which they used as anode catalysts. All cathodes loading were calculated to have a constant 1 mg$_{Pd}$cm^{-2}. They have shown that all the samples had a higher catalytic activity and lower overpotential for the EOR. They have found that the sample containing Pd:Ni with a ratio of 2:3 offered the highest current density reaching 90 mWcm^{-2} at a temperature of 60°C and a fuel concentration of 3 M ethanol + 5M KOH compared to 67 mWcm^{-2} obtained with Pd/C. This fuel concentration is thought to be optimal by providing a large coverage of the catalyst surface by hydroxyl groups facilitating the oxidation of adsorbed ethoxy molecules which is accepted as the rate limiting step of the oxidation of ethanol to acetic acid [24], [64].

Another research groups has shown innovation by finding a way to operate a DEFC using a CEM in alkaline media. An et al. [65] have theorized that by using a base with a small cation at the anode it would be possible to use a CEM to allow this cation to reach the cathode. At the anode, the fuel would get oxidized by the hydroxyl molecule present in the solution on the surface of the catalyst which would send electrons through an external circuit. Meanwhile, the cation migrates through the membrane to the cathode where two reactions occur: 1) oxygen and water react to produce adsorbed hydroxyl molecules, 2) the adsorbed hydroxyl molecules would react with an electron exiting the external circuit and with the transferred cation to form a based (e.g. NaOH). In their publication they have tested their theory by testing an AEM from Tokuyama Corporation and a Nafion 117 membrane in the same fuel cell under the same conditions. A PdNi/C catalyst was used at the anode and a Fe-Co HYPERMEC^{TM} catalyst was used at the anode both with a metallic loading of 1 mg$_M$cm^{-2}. By testing both systems with a fuel concentration of 3 M ethanol + 5 M KOH they have shown that operating using a CEM in alkaline media could provide a higher current density than while using an AEM. Indeed, they have shown that a power density of 100 mWcm^{-2} could be obtained compared to 90 mWcm^{-2} when operating with a CEM. However, at higher temperature the performances are inversed with the CEM operating at 135 mWcm^{-2} which is 17% higher than the AEM operating at 115 mWcm^{-2}. This change is explained by an increase in NaOH permeability of the CEM at higher temperature reducing the operating potential of the DEFC.

In summary, various DAEFCs have been tested using ethanol in KOH as a fuel with a Pt or Pd-based anode catalyst. These fuel cells have shown to be able to compete with similar fuel cells operating in acidic environment with some of them even showing higher power densities with a maximum of 115 mWcm^{-2} achieved. The AEM currently competing with Nafion is supplied by Tokuyama Corporation achieving comparable ionic conductivity.

2.2.2 Catalysts for Alcohol Electrooxidation Containing Metal Oxides

Amongst other materials, metal oxides have been intensively studied as co-support/co-catalyst for the electrooxidation of alcohols in alkaline media when combined with Pt and Pd based catalysts. These tests have shown that such modifications of the catalytic systems could improve significantly the activity of the catalysts, reduce the overpotential of the EOR and reduce the poisoning rate of the catalyst surfaces. This section, separated in four sub-sections, will resume previously published research concerning the addition of the three metal oxides concerned in this research to Pd and Pt based catalytic systems along with a fourth section concerning ethanol oxidation in the presence of various other popular metal oxides.

2.2.2.1 Catalysts Containing CeO_2

Many studies have turned their attention on the effect of the addition of CeO_2 to Pt and Pd based catalytic systems for ethanol electrooxidation [26], [66]–[69]. All these studies have reported similar results including: lower onset potential than the same catalyst without the metal oxide, a higher current density over the whole potential range and a higher stability. In all these articles the higher onset potential and faster oxidation rate on the metal surface has been attributed to the ability of the CeO_2 phase to adsorb OH^- species (OH_{ads}) at lower potential than on Pd and Pt which is thought to be the rate limiting step for ethanol oxidation at low potential. These OH_{ads} would either react with neighbouring catalytic sites or spilled directly on the metal surface providing these needed molecules to strongly adsorbed CO-like species liberating new reaction sites. Some of these studies [26], [68], [69], have varied the composition ratio of Pd:CeO_2 and Pt:CeO_2 in the catalysts and have found that the composition that was the most active for the EOR was 2:1 in both cases. This volcano behaviour is explained for the first part by an increase in OH_{ads} species on or near the surface of the metal catalyst caused by the presence of the metal oxide improving the reaction rate of ethanol oxidation. At a certain composition the loss in Pd or Pt surface due to an increasing amount of CeO_2 overtake the promoting effect of the OH_{ads} molecules causing the apparent activity of the catalyst to diminish due to a decreasing amount of reaction sites.

In three complimentary studies, Xu et al. [26], [68], [69] have shown the promoting effect of CeO_2 on the activity of both Pd/C and Pt/C nanocatalysts. In their works, the CeO_2 was deposited on carbon via a solid-state reaction under microwave irradiation while the Pd and Pt were synthesized on the surface of the support by the reduction of their dissolved salts in aqueous solution. In these experiments, they have observed an EOR onset potential negative shift of 50 to 100 mV on both Pd and Pt with the presence of CeO_2 compared to bare Pd/C and Pt/C nanocatalysts. In the first two studies [68], [69] they have varied the composition of the Pt:CeO_2 catalysts ranging from 100 % Pt to 50 % Pt and 50 % CeO_2 and they have observed that the optimal ratio was around 2:1 (Pt:CeO_2) where they obtained a current density around 2.4 times higher than for Pt/C. In a third study [26], they have shown that the activity of the Pd based catalysts was about twice as high as their Pt-based counterparts resulting for an increase in the current density by a factor of four between Pt/C and Pd-CeO_2/C.

More recently Uhm et al. [66] have synthesized Pd-CeO_2 nanobundles via anodic co-electrodeposition of CeO_2 nanoparticles and Pd ions on an alumina template resulting in a highly ordered array with a depth of 3000 nm and a rod diameter of 200-300 nm. They have reported a shift in the EOR onset potential similar to that reported by Xu et al. [26], [68], [69] with an increase in current density of 75 % compared to pure Pd nanobundles. They have also observed an increase in stability of the electrode. The promotion mechanism was attributed to the same effect as discussed earlier in this section.

In another study conducted by Bambagioni et al. [67] Pd-CeO_2/C nanocatalysts were synthesized by a two step method and were then tested in an DAEFC using an AEM provided by Tokuyama Corporation and a Co-Fe/C cathode. The first step in the nanoparticle synthesis was the ionic reduction of a Ce(IV) salt in aqueous solution followed by a reflux of a Pd salt in the presence of the previously formed support in a mixed aqueous/alcohol solution. This group has also observed a negative shift in the EOR onset potential of the CeO_2 containing catalysts corresponding to what was reported earlier. For the fuel cell test they have obtained a power density of 65 $mWcm^{-2}$ at room temperature with pure oxygen at the cathode which was three times as high as what was obtained with Pd/C. A power density of up to 140 $mWcm^{-2}$ was obtained for a higher temperature of 80°C.

2.2.2.2 Catalysts Containing SnO_2

A few groups worked on the development of Sn and SnO_2 containing Pd and Pt based catalysts for electrooxidation in alkaline and acidic media [70]–[73]. It was reported that the attempt at the formation of a PtSn or a PdSn alloy would result in a large part of the Sn atoms to forming a SnO_x phase which was confirmed by XRD where the lack of crystallinity of Sn and the absence of an alloy could be observed [70], [73]. Some of them [71], [73] have found that a relatively high Sn atomic ratio was the most favorable composition for the EOR on the Pt and Pd catalysts with results varying between 30 and 50 atom%. All studies agreed that this increase in catalytic activity observed for SnO_2 containing catalysts is attributed to a synergistic effect where the adsorption of OH^- species on the surface of SnO_2 promotes the oxidation of strongly adsorbed carbonaceous molecules on the surface of the catalyst which is needed for ethanol adsorption.

In two independent studies, Mao et al. [70] and da Silva et al. [73] have deposited obtained $PdSnO_2/C$ nanoparticles by trying to synthesize PdSn/C nanoparticles which were tested for the EOR in alkaline media. In the first study, the SnO_2 nanoparticles were formed using a modified polyol method while in a second step the Pd nanoparticles were obtained by ion reduction using $NaBH_4$. They have observed an increase in current density by a factor of 2.4 and a significantly higher steady state current density after prolonged operation. In the second study, the $PdSnO_2/C$ nanoparticles were synthesized by the co-reduction of Sn and Pd ions using $NaBH_4$. They have synthesized catalysts with atomic ratios of Pd:Sn varying between 1:0 and 1:1. It was observed that the sample with a Pd:Sn ratio of 1:1 had the highest activity during electrochemical characterizations with a current density around 4 times higher than that of Pd/C and a much higher stability. However, tests in fuel cell have shown that the catalyst having the composition Pd:Sn 9:1 showed the highest power density, a behaviour that was attributed to the lower total loading of catalysts due to a constant geometric density of Pd and to a constant Pd loading (20 wt%) which decreased the dispersion of the particles and the conductivity of the catalyst with increasing Sn constant.

Two other studies using Pt-based nanoparticles in acidic media (one for methanol oxidation and one for ethanol oxidation) have shown the promotional effect of SnO_2 as a co-support. A study by Ren et al. [72], synthesized, using a microwave-assisted polyol reduction method, Pd/C, $PdSnO_2/C$ and $PdSnO_2$/MWCNTs for methanol oxidation. They observed a negative shift of 20 and 30 mV in the onset potential respectively while going from Pd/C to $PdSnO_2/C$ and $PdSnO_2$/MWCNTs respectively along with an increase in stability following the same trend. The current densities observed were found to be 40 % and 90 % higher for $PdSnO_2/C$ and $PdSnO_2$/MWCNTs respectively when compared to Pd/C. The increase caused by the modification of the support is attributed to the structural and electrical properties of the MWCNTs. On their side, Jiang et al. [71] have prepared $Pd/SnO_x/C$ nanoparticles with Pt:Sn atomic ratios ranging between 8:2 and 5:5 using a modified polyol method. They have found that the oxidation of ethanol on Pt and on their synthesized catalyst results mainly in acetaldehyde (about 80 %). The yield of acetic acid was at its maximum on the catalysts with the composition 7:3 which was also characterized by a higher current density than the other catalysts. It is also this composition that showed the highest power density (60 mWcm^{-2}) in an acidic fuel cell at 90°C with a fuel concentration of 1 M and an operating pressure of 2 bar at the cathode using humidified oxygen.

2.2.2.3 Catalysts Containing TiO_2

Another metal oxide material that has been of large interest as a co-support for ethanol or alcohol electrooxidation in alkaline media is TiO_2 either in the nanotube [74], [75] form or nanoparticles [76], [77]. All of these studies have observed an increase in catalytic activity per ECSA for TiO_2 containing catalysts compared to Pd/C. This increase in catalytic activity following the addition of TiO_2 to the catalytic systems was attributed to a few different phenomena. First, TiO_2 is known be able to have a large surface density of hydroxyl groups ranging from 1.5 to $6.2*10^{14}$ molecules per cm^2 of surface area [78], [79] depending on its crystal structure. This property of the metal oxide is proposed to supply hydroxyl groups to the Pd catalyst in order to help in the removal of adsorbed molecules at a faster rate and without monopolizing prime ethanol reaction sites. It was also proposed that there was an electronical effect between Pd nanoparticles and the TiO_2 modifying the binding energy of the d band electrons of Pd resulting in a modification of the adsorption strength of carbonaceous intermediates facilitating their oxidation [76], [77]. A downside that was found during these studies is that the ECSAs were found to decrease with increasing TiO_2 content due to a lower porosity of the support [75]–[77].

A study conducted by Hu et al. [75] tested the electrochemical activity of Pd deposited on carbonised TiO_2-nts (TiO_2C) for the EOR and compared it to the activity of Pd/C. The nanotubes were synthesizes by a mild hydrothermal method while their carbonisations were made by annealing the obtained nanotubes in an Ar atmosphere at 600°C in the presence of polyethylene glycol. The nanoparticles were subsequently formed directly on the surface of the nanotubes by ion reduction using $NaBH_4$. They varied the Pd loading on the surface of the nanotubes and have found that a mass ratio of Pd:TiO_2C of 1:1 yields the best performance showing a threefold increase in power density obtained by Pd/C for ethanol electrooxidation. The decrease in catalytic activity at higher Pd loading is explained by a lost in porosity of the system by the formation of a complete layer of Pd on the surface of the nanotubes.

Another work published by Silva et al. [77] concerning the activity of Pd nanoparticles deposited using $NaBH_4$ on a physical mixture of C + TiO_2 nanoparticles with C:TiO_2 ratios varying between 1:0 and 0:1. Using linear sweep voltammetry (LSV), they have found that a support with a ratio of C:TiO_2 of 40:60 proved to have the highest Pd mass activity for the EOR. This optimal point is explained by an increasing catalytic activity of the Pd surface caused by the supply of hydroxyl group coming from the TiO_2 surface with increasing TiO_2 content and the modification of the binding energy of the electrons in the Pd d-band which are counteracted by the decrease in a_s caused by the substitution of porous carbon support by more dense TiO_2 particles. They have obtained an increase of 25 % in the Pd mass current density when compared to Pd/C without TiO_2 at 0.0 V vs Ag/AgCl.

There is also a recent work conducted by Qin et al. [76] which explores the performance of a catalytic system composed of Pd nanoparticles deposited on the surface of a C-doped TiO_2 layer surrounding a carbon black core using a modified polyol method. In this study, they have shown that the poisoning of the electrode decreases with the addition of C-doped TiO_2 layer over the carbon black nanoparticles and that an increase in current density of the EOR on the Pd nanoparticles was increased by 50 %. On top of the two effects discussed previously, they suggest that the adsorption of ethanol on the surface of TiO_2 caused by an interaction with the partially empty d-orbitals, due to the presence of carbon atoms replacing oxygen ions, would facilitate the transportation of ethanol molecules to Pd reactive sites and would also play a role in the increased activity of the Pd nanoparticles.

2.2.2.4 Catalysts Containing Other Metal Oxides

Various other metal oxides have been studied as to observe their effect as a co-support along with carbon to Pt and Pd-based catalysts on the EOR. It was shown that a wide variety of metal oxides could have a beneficial effect on the EOR. This increase in activity was almost always attributed to the effect discussed previously where the metal oxide surface would supply adsorbed hydroxyl species at lower potential than on the metal surface facilitating the oxidation of the adsorbed molecules.

A series of studies conducted by Xu et al. [26], [80], [81] have tested the effect of the addition of various metal oxides (NiO, Co_3O_4, Mn_3O_4 and MgO) as co-supports to carbon on the catalytic activity of Pt and Pd nanostructured catalysts. In all of their studies the metal oxide modified carbon support was synthesized using an intermittent microwave heating method in aqueous solution. They have found that the addition of NiO with a mass ratio of 1:6 in relation to Pd and to Pt had the highest effect on the metal activity for the EOR with an increase in current density of 3.5 and 5 times that of the NiO free Pt and Pd catalysts respectively. They have also shown that Pd/C and Pd-NiO/C had a catalytic activity twice as high as their corresponding Pt based homologues. Similar results concerning the NiO containing catalysts were observed by Hu et al. [25] which were explained by a higher poisoning rate by CO-like species on the surface of Pt than on Pd. Xu et al. [26], [80], [81] have also shown that an addition of Mn_3O_4 and Co_3O_4 to Pd/C with mass ratios of Pd to metal oxide of 4:1 for both systems would lead to an increase in current densities of 50 and 250 % respectively [26], [80] and that an addition of MgO to Pt/C with a mass ratio of Pt:MgO of 4:1 would lead in an increase in current density of 400 % [81].

There is also a study published by Bai et al. [82] which shows that the addition of Zr ions during the physical deposition of Pt ions on the surface of carbon black in aqueous solution would result in a Pt-ZrO_2/C system. They tested these catalyst for the EOR and have found that the addition of ZrO_2 to the catalyst with a molar ratio of Pt:ZrO_2 of 1:4 shows the best performance with an increase in current density of 60 % and a lower maximum ethanol peak potential.

2.2.2.5 Summary

In summary, various metal oxides have been shown to promote the catalytic activity of Pt and Pd-based nanocatalysts for ethanol oxidation in alkaline media when used as support/co-supports. Current density increases as high as 400 % were been observed. This promotional effect is usually attributed to two different phenomena. Firstly, a larger supply of OH^- species and that at lower potential than on carbon black promote the oxidation of carbonaceous species near the metal-metal oxide interface. Secondly, the oxidation of adsorbed species on the surface of the catalysts is facilitated by a modification of the adsorption strength due to an electronic effect modifying the Pd electron density.

2.3 TiO_2-nanotubes as Electrocatalyst Support for the Oxidation Reaction of Organic Molecules

The use of TiO_2-nts formed via various methods for use as supports for oxidation reactions is increasing in popularity and various research groups have studied their promotional effect for various organic molecules [83]–[90]. This interest comes from the fact that TiO_2 has shown to give a promotional effect to different supported metal nanoparticles for various reactions. That is why it is expected to obtain high catalytic activity both by ECSA and by geometric area following the deposition of metal nanoparticles on the surface of highly ordered TiO_2-nts arrays exposing an extensive three dimensional structure with high surface area to geometrical surface area ratio. Also, various parameters can be modified in order to obtain a relatively high level of control on the morphology of the obtained nanotubes.

Two groups have tested the electrooxidation of ethanol on TiO_2-nts containing catalysts. A first study, lead by Song et al. [88], studied the difference in catalytic activity of three different catalysts: Pt/C, TiO_2/Pt/C and TiO_2-nts/Pt/C. The TiO_2 nanoparticles and nanotubes were mixed with the Pt/C catalyst with a TiO_2 to Pt weight ratio of 1:1. They observed an increase in current density of 100 % when going from Pt/C to TiO_2-nts/Pt/C during the EOR in acidic media with the activity of TiO_2/Pt/C situated approximately in the middle. A negative shift in the potential at which the CO stripping peak was observed on TiO_2-nts/Pt/C compared to the other samples which suggests that the oxidation of strongly adsorbed intermediates is easier on this catalyst than on TiO_2/Pt/C and Pt/C. A second study by Qin et al. [90] produced anodically grown TiO_2-nts of different length (325 to 425 nm) on which they deposited Pd nanoparticles electrochemically. They have found that the synthesized catalysts had good activities towards the EOR which was ascribed to a good dispersion of the Pd nanoparticles on the TiO_2-nts surface and to a reduced poisoning of the Pd surface. They also reported an increase in a_s with increasing TiO_2-nts length but a lower mass current density. This phenomenon was explained by larger transport resistance of the reagents and products with increasing tube length and to a higher conductivity of shorter nanotubes.

The use of TiO_2-nts as supports for different noble-metals used for the oxidation of various other organic molecules has been reported. Indeed, a series of studies conducted by

Hosseini et al. [85]–[87] have shown the potential of anodically grown TiO_2-nts as supports for the oxidation of a wide variety of organic molecules: galactose, glycerol, glucose, dopamine and ascorbic acid. In a first study [86] Au nanoparticles were deposited on TiO_2-nts and the activity of the resulting electrocatalyst towards the oxidation of galactose was compared to pure Au electrodes. A good activity towards this reaction was obtained and the Arrhenius plot suggested that the activation energy of the oxidation of galactose on Au nanoparticle was lower than that of Au films. Another publication [87], describes the catalytic activity of Pt/TiO_2-nts towards the oxidation of glycerol. They have shown an increase in catalytic activity compared to pure Pt and to Pt/Ti which is attributed to a slower deactivation process caused by the increase roughness of the electrode surface. A last study [85] investigated the activity of Au nanoparticles deposited on TiO_2-nts for the oxidation of glucose, dopamine and ascorbic acid. It was demonstrated that the catalysts had much higher activities for glucose oxidation than pure Au foil. Also, whereas pure Au foil does not have any catalytic activity towards ascorbic acid and dopamine oxidation Au/TiO_2-nts showed distinguished peaks for those reactions. Ag/TiO_2-nts have also been synthesized in this study and it has shown a good activity towards the oxidation of hydrazine.

A few other groups have reported the oxidation of small organic molecules on the surface of Pt-based nanoparticles deposited on the surface of TiO_2-nts. One of them is Chen et al. [83] who synthesized Pt/TiO_2 and PtAu/TiO_2 catalysts with Pt:Au atomic ratios of 2:1 and 1:1 and tested their activity towards formic acid oxidation. Both Au containing catalysts have shown a similar activity for formic acid oxidation which was higher than that of the Pt/TiO_2 catalyst. They also reported a negative shift in the onset potential of the oxidation reaction for Au containing catalysts. Another study made by Macak et al. [84] tested Pt/Ru nanoparticles deposited on TiO_2-nts and conventional nonporous TiO_2 supports for the oxidation of methanol.

They have also observed the effect of annealing the support to form an anatase phase before the deposition of the nanoparticles. They have found that Pt/Ru deposited on TiO_2-nts had a higher catalytic activity and that crystallisation of the nanotubes further promote the methanol oxidation reaction.

In summary, TiO_2-nts have shown to be promising catalyst support for alcohol oxidation due to its high real surface area per geometrical surface area. The mass current density has been shown to reach values up to 100% higher on metal catalysts nanoparticles deposited on TiO_2-nts compared to those deposited on carbon black. Also, modification of this support, such as annealing, has shown to further improve the catalytic activity of the deposited catalyst due to the enhanced electronic conductivity caused by the more crystalline structure.

2.4 Graphene as Electrocatalyst Support for the Oxidation Reaction of Small Alcohol Molecules

Graphene is a large two dimensional monolayer of hexagonally arranged sp_2 carbon atoms which offers an a_s reaching up to 2600 m^2g^{-1} [54], [91], [92]. This very high a_s offer the possibility to obtain a higher dispersion and utilisation of the deposited nanoparticles. For this reason many groups have studied this material as a support for Pt group-based nanoparticles used in the electrooxidation of small alcohol molecules and compared their result to nanoparticles supported on other carbon based materials [15], [49], [87]–[96]. All of these studies have observed highly homogeneously dispersed nanoparticles on the surface of the graphene sheets which is generally used to explained increase mass current density due to a higher metal surface utilisation.

The following studies [15], [91]–[94], [97]–[99] have looked into the promotional effect of reduced graphene and graphene oxide as supports for Pt-based and Pd-based catalysts for small alcohol molecules compared to those deposited on carbon black or other carbon supports. In general, it was observed that going from another carbon support to a graphene support causes an increase in mass current density, real surface area current density, a decrease in the onset potential and a higher resistance to poisoning.

Three studies have looked into the catalytic activity of Pt nanocluster on graphene towards methanol oxidation [91], [92] and ethylene glycol oxidation [99]. Both studies on methanol have found the mass activity of Pt doubles when it is deposited on graphene instead of carbon black with possible loadings as high as 80 wt% having a high utilisation due to a very good dispersion on the support surface caused by the large a_s. The study on ethylene glycol oxidation revealed that the ECSA of the catalyst deposited on graphene was slightly higher than that of Pt/MWCNTs. It also expressed a lower poisoning rate showed by a lower If/Ib ratio and an increase of 30 % in the current density per ECSA. The following study [15] tested the catalytic performances of Pt-Ru nanocatalysts for methanol and ethanol electrooxidation when deposited on carbon black and on graphene. An increase of 20 % in ethanol oxidation current density and of 100 % methanol was observed on the Pt-Ru nanoparticles on graphene.

Other studies [93], [94], [97], [98] have investigated the catalytic activity of Pd and Pd-M alloys deposited on graphene as nanocatalysts for the oxidation of ethanol. In two of the studies [97], [98], pure Pd nanoparticles were deposited on graphene and tested for the EOR. Singh et al. [98] have observed an increase in current density for the EOR of 30 and 50 % when going from carbon black and MWCNTs to graphene respectively. On their side, Wu et al. [97] showed that thermal treating of graphene sheets under inert atmosphere at temperatures of 400 to 600°C before Pd deposition could further increase the activity of the catalyst for the EOR. They have shown that the activity of the catalyst could increase by 75 % compared to non-treated graphene supports. Two studies, one by Huang et al. [94] and the other by Liu et al. [93], have investigated the activity of PdAu and PdAg nanocatalyst deposited on graphene respectively. In the first one the PdAu nanoparticles deposited on graphene has shown an ECSA 2.7 and 7 times larger than those obtained with PdAu nanoparticles on MWCNTs and carbon black respectively. Also, mass current densities of the catalyst on graphene were found to be 1.7 higher than on MWCNTs and 3.25 times higher than on carbon black. In the second study PdAg nanoparticles deposited on graphene had a higher catalytic activity than similar nanoparticles deposited on carbon black and on MWCNTs. They have also observed that the catalyst composed of PdAg with a mass ratio of 1:1 had the highest catalytic activity for the EOR.

Different surface modifications can be made to graphene in order to influence various parameters such as the promotion of the catalytic activity of supported nanoparticles, the dispersion of nanoparticles on its surface and its hydrophobicity. It was shown that the modification of graphene surfaces using sulphonated groups would increase the resistance to poisoning by adsorbed carbon species of supported catalyst compared to non-modified graphene [101]. Sulphonation of graphene has also shown to increase the dispersion of metallic nanoparticles on its surface during deposition [101]. Also, the higher hydrophobicity of sulphonated graphene has shown to increase its dispersion in water favoring a more even dispersion of nanoparticles when deposition is obtained in aqueous media [102], [103]. A study made by Wen et al. [54] have also shown that Pd deposited on SnO_2-modified graphene expressed a higher catalytic activity than non-modified graphene sheets towards ethanol electrooxidation. This increase in activity is attributed to the supply of OH^- from SnO_2 sites to neighbouring Pd nanoparticles.

In summary, graphene was shown to promote the mass activity of Pt and Pd-based catalysts for alcohol oxidation compared to other carbon-based supports such as carbon black, CNTs and MWCNTs. This larger mass activity is attributed to the high a_s of the material allowing a better dispersion of nanoparticles and an increased metal-support interface where OH^- ions can be supplied to oxidised adsorbed species. It is also shown that modifications of graphene sheets such as thermal treating or the addition of functional groups can further promote the activity of the deposited metal catalysts.

2.5 Cathode Catalyst (Oxygen Reduction)

2.5.1 Pt and Pt-Based Catalysts

On the cathode side of a DAFC, whether it is fed air or pure oxygen, the oxygen reduction reaction (ORR) (represented by **Eq. 2.8** to **2.11**) takes place [104], [105]. In this reaction an oxygen molecule is adsorbed on the surface of a metal atom in a bridge configuration. Neighbouring hydroxyl groups react with one of the oxygen atom to form a HO_2 group on the surface of a metal atom. This molecule is further oxidized to two water molecules.

$$\boldsymbol{O_2 + Pt \rightarrow Pt - O_2} \qquad \textbf{2.8}$$

$$\boldsymbol{Pt - O_2 + H^+ + e^- \rightarrow Pt - HO_2} \qquad \textbf{2.9}$$

$$\boldsymbol{Pt - HO_2 + Pt \rightarrow Pt - OH + Pt - O} \qquad \textbf{2.10}$$

$$\boldsymbol{Pt - OH + Pt - O + H^+ + 3e^- \rightarrow 2H_2O + 2Pt} \qquad \textbf{2.11}$$

Once again Pt is known to be the best catalyst for this reaction. It is however possible to increase the activity of Pt for the ORR by alloying the metal with other metal atoms (including but not limited to Cr, Mn, Fe, Co, Ni, Sn and V) or by the deposition of a thin Pt layer on the surface of other nanoparticles as it was shown in various independent studies [105]–[109]. These increases in activity were attributed to different phenomena occurring simultaneously. In a first part, by alloying Pt with various metal atoms it is known that the lattice parameter of the crystal structure will vary with the degree of alloying and the size of the ad-atom. This modification in Pt-Pt or Pt-M distance could influence the ORR rate by favoring the adsorption of oxygen on the surface of the catalyst. Also, by adding ad-atoms with an incomplete d-band it is possible to modify the electron density of the Pt 5d orbital due to a Volta potential modifying the Fermi level of the catalyst favoring the reduction of attached molecules. Finally, it was proposed that a presence of a more complete oxide layer on the surface of the catalyst could be achieved with an alloy which would provide hydroxyl groups for the ORR [110].

A study conducted by Mukerjee et al. [109] has tested various Pt alloys with an atomic Pt to Cr, Mn, Fe, Co or Ni ratio of 1:1 de posited on carbon for the ORR. They have shown that the presence of any of these metals had a beneficial effect on the catalytic activity of the catalyst for the ORR. They have observed an increase in current density by ECSA up to a factor of 3 for PtCr alloy and a decrease in current density following: PtCr/C > PtFe/C > PtMn/C > PtCo/C > PtNi/C > Pt/C. A trend with a volcano shape in the current density was observable when the maximum current density was plotted against both the inter-atomic distance of the catalyst and the d-orbital vacancy. This optimal point is explained by reaching the smallest variation in Gibbs energy for the adsorption of hydroxyl groups on the surface of the catalyst.

Another study published by Toda et al. [105] reuse a few of the alloys presented in the previous study and vary the Pt to metal atomic ratio from pure Pt to low Pt content. The metals used in this study are Ni, Co and Fe. They observed that it was possible to obtain a current density for the ORR up to 20 times higher with a PtM alloy than on Pt alone. The optimal Pt to metal ratio was found to be different for each type of metal ad-atom with a ratio of 3:7 for Ni, 2:3 for Co and 1:1 for Fe. This increase is caused by a modification of the electron density of the

Pt 5d orbital facilitating the acceptance of the 2p electrons of O_2 increasing the adsorption speed and decreasing the bond strength.

In two other studies, one made by Jeyabharathi et al. [106] and the other by Antolini et al. [108], the performances of two other Pt based alloys for the ORR is explored. In the first study, a PtSn alloy with a Pt to Sn ratio of 7:3 is synthesized using a modified polyol method obtaining two structures: an fcc configuration with a composition of $Pt_{75}Sn_{25}$ and an hexagonal configuration containing a $Pt_{50}Sn_{50}$ composition. They found that while the synthesized catalyst was only marginally better than pure Pt/C it was more resistant to fuel crossover increasing its life expectancy. In the second study Pt is alloyed to V with a nominal ratio of 1:1 and tested for the ORR. They found that the as synthesized catalyst showed lower performance for the ORR than Pt/C at atmospheric pressure. However, an increase in pressure over 2 atm gives the vanadium containing catalyst a higher catalytic activity which increases to 20 % higher than that of Pt/C under the same conditions at 5 atm. It is also shown that annealing the catalyst at 850°C under a reducing atmosphere increases the activity of the PtV/C catalyst at lower pressure higher than that of Pt/C while sacrificing activity at higher pressure. This effect of annealing is suggested to be caused by a change in the catalyst structure which passes from the fcc structure with a Pt_3V composition to another fcc structure with the Pt_2V composition.

A last study used another approach where instead of alloying a metal with Pt they deposited a sub-monolayer of Pt on the surface of carbon supported metallic nanoparticles. Indeed, Sasaki et al. [107] have deposited partial layers of Pt on the surface of Au and Ru nanoparticles using a spontaneous deposition method. They observed that the activity of a sub-monolayer of Pt on Au could offer the same current density for the ORR than a Pt/C catalyst containing several times the Pt loading.

In summary, Pt is a very active catalyst when used for the ORR. However, alloying Pt with another metal, such as Cr, Mn, Fe, Co, Ni, Sn, V, etc. could further increase the reaction rate of oxygen molecules at the surface of the catalyst. This promotional effect is caused by two phenomena. Firstly, a modification of the lattice parameter of Pt influences the oxygen adsorption rate on its surface modifying the ORR reaction rate. Secondly, the addition of ad-atoms with an incomplete valence band it is possible to modify the electron density of the Pt 5d orbital favoring the reduction of adsorbed molecules.

2.5.2 Non Pt-Based Catalysts

As for the anode catalysts, scientists around the world have explored the possibility of using other materials than Pt as cathode catalyst in order to decrease its production costs. As of now, a few materials have shown promising results out of which MnO_x based nanocatalyst deposited on carbon based supports have taken the lead as potential substitute to Pt catalysts [111]–[115]. While the activity of Pt for the ORR has yet to be surpassed, Pt-less catalysts have shown comparable activities with significantly higher stability during operation [116]. Other materials such as metallic alternatives [117], [118] or nitrogen doped carbon materials [116], [119] have also been proposed as catalyst after demonstrating reasonable activity.

As mentioned, MnO_x and MnO_x-based catalysts show good activities towards the ORR. Many modifications were made to the catalysts in order to further promote the surface reaction. Amongst other, Roche et al. [113] made some modification to MnO_x nanoparticles on carbon by doping the nanoparticles with Ni and Mg ions. This modification provided a specific and mass activity for the ORR comparable to commercial Pt/C catalysts. Another group [114] published a study where they show the effect of the deposition of MnO_x nanoparticles on the surface of Nafion-modified Au electrodes. They found that the addition of MnO_x nanoparticles to the electrode had a beneficial effect on the ORR when compared to the bare Nafion-modified Au electrode. A study by Zhang et al. [111] tested the activity of a dual catalytic system composed of MnO_x modified with cobalt octacyanophthalocyanine deposited on a glassy carbon electrode towards the ORR. They observed an activity similar to that obtained on Pt nanoparticles. In all the works dedicated to the ORR on MnO_x materials the high in activity is explained by the promotion of the 4 electron reduction pathway which has faster kinetics and less hydrogen peroxide by products due to the reduction of Mn from Mn (IV) to Mn (III) in the form of MnOOH [111]–[115].

Other groups have tested metals less expensive than Pt for the ORR with interesting results. Xiao et al. [117] have compared two Pd nanostructured materials with different geometry showing preferential plane orientation and have compared the results with Pt. They have shown that Pd with the (110) preferential orientation (Pd nanorods) had an activity higher by an order of magnitude compared to standard Pd nanoparticles. The activity of the Pd nanorods for the ORR was comparable to that of Pt. The proposition made for such a difference in activity is the weak bond of oxygen on the Pd (110) surface accelerating the reaction rate when compared to other surface configurations. There is also a study by Hacker et al. [118] have tested Ag as a catalyst for the ORR. They have found that depositing Ag nanoparticles on the surface of CNFs could give catalyst with an activity comparable to that of Pt at low loading with a low overpotential. They have also shown that an increase in loading would not result in higher activity but would rather be express by a higher overpotential.

A few works are also dedicated to the ORR on nitrogen doped carbon nanosheets (graphene or carbon nanotubes). Indeed, in a work published by Nagaiah et al. [119] bare carbon nanotubes (CNTs) doped with nitrogen are used for the ORR and the effect of annealing the catalysts in an inert environment on their activity for the reaction is assessed. They have found that the formation of different nitrogen components on the surface of the CNTs at higher temperature as shown by peaks apparition at higher binding energy (XPS) would promote the ORR reaching activities higher than that of commercial Pt nanocatalysts. Also, a study made by Liang et al. [116] shows the effect of the nitrogen doping of the graphene support of Co_3O_4 on the ORR. They have shown that while Co_3O_4/graphene had a reasonable activity for the ORR, the doping of the support with nitrogen has boosted the activity just under that of commercial Pt catalysts with a very high stability for long periods of time in harsh alkaline environments.

These studies show that there are many potential alternatives to the costly Pt as cathode catalyst and that a lot of them are more stable with comparable current density. These results bring us one step closer to commercial DAFCs.

2.6 Anion Exchange Membrane

As discussed previously, while the utilisation of an AEM in DEFC brings various benefits when compared to CEM such as lower fuel crossover, cheaper catalysts and easier water management, there is still the problem of obtaining a high anionic conductivity (>0.01 Scm^{-1} to be competitive with Nafion) [24]. The solid polymer electrolyte membranes used in alkaline media are usually categorised in two distinct main groups, polyelectrolytes and ion solvating polymers (ISPs) [24]. The former is based upon the grafting of positively charged groups (usually quaternary ammonium groups [120], [121] (sulphur and carbon based groups have also been reported [24]) on polymer chains that interacts with the anion of the ionic salt (usually NaOH or KOH in fuel cells) to transfer an anion from high to low OH^- concentrations (Nafion is a polyelectrolyte for H^+). On the other hand, ISPs are polymers with integrated electronegative heteroatoms (oxygen, nitrogen, sulphur and phosphorus [24], [120]) soluble in water. These membranes are composed of the polymer, a hydroxide salt and a plasticizer (to maintain the solid form) [120]. The cation from the hydroxide salt (usually potassium) is attracted to the electronegative atoms through a donor-acceptor link causing apparent positively charged sites on the surface of the polymer which allows the transport of anions. **Table 2-1** gives a list of some experimental ISPs and polyelectrolyte and commercial AEM expressing high conductivity.

Membranes based on polyelectrolyte with quaternary ammonium groups have been shown to express conductivities in the range of 0.01 to 0.065 $\mathrm{Scm^{-1}}$ with membrane thickness being less than 100 μm. A series of studies by Slade and Varcoe [27], [122]–[125] have shown that Poly(hexafluoropropylene-co-tetrafluoroethylene) (FEP) and Poly(Ethylene-co-Tetrafluoroethylene) (ETFE) based membrane grafted with quaternary ammonium groups with and without modifications to the polymer chain could express ionic conductivities in the range of 0.02 to 0.035 $\mathrm{Scm^{-1}}$ at moderate temperatures (30 – 60°C). More recently, other groups [126]–[128] have shown high conductivity of an AEM based on other quaternary ammonium grafted polymers such as poly(arylene ether sulphone), poly(phenylene oxide) and poly(aryl ether ketone)s out of which the former expressed the highest conductivity with values up to 0.065 $\mathrm{Scm^{-1}}$ at 70°C [126].

AEMs based on ISPs usually show slightly lower anionic conductivities with typical values below 0.02 $\mathrm{Scm^{-1}}$ with a few exceptions. One of these exceptions has been discussed in a work by Xing et al. [133] where a PBI film doped with KOH demonstrated a conductivity of up to 0.09 $\mathrm{Scm^{-1}}$ which is comparable to that of Nafion at room temperature. Also, a work by Yang et al. [130] obtained conductivities of up to 0.047 $\mathrm{Scm^{-1}}$ at room temperature from a polyvinyl alcohol (PVA) membrane doped with KOH. Various other groups have obtained good results by modifying PVA polymer chains before KOH doping (refer to **Table 2-1** for more details).

Table 2-1: List of recent experimental and commercial membrane with thickness and ionic conductivity

Membrane	Thickness / µm	Temperature / °C	Conductivity / Scm^{-1}	Ref
Experimental				
Polyelectrolyte				
FEP quaternary ammonium	50	60	0.02	[122], [123]
ETFE quaternary ammonium	51	30	0.03	[124]
FEP-g-PVBC quaternary ammonium	50	50	0.023	[27]
ETFE-based quaternary ammonium	78	50	0.034	[125]
Poly(arylene ether sulphone) quaternary ammonium	----------	70	0.025 - 0.065	[126]
Poly(phenylene oxide) quaternary ammonium	----------	70	0.0083	[127]
Poly(aryl ether ketone)s quaternary ammonium	----------	80	0.0307	[128]
Ion Solvating Polymers				
PEO/KOH	----------	25	0.001	[129]
PVA/KOH	300 – 600	25	0.047	[130]
PVA/PECH	400 – 600	25	0.02	[131], [132]
PVA/TEAC	400 – 600	25	0.0231	[131]
PBI/KOH	40	25	0.09	[133]
PVA/PVP/KOH	----------	25	0.002	[134]
PVA/ PEGDE/KOH	----------	25	0.0015	[134]
PVA/KOH	60 – 100	25	0.000977	[135]
PVA/[Bmim]OH	120	25	0.0196	[136]
Commercial				
Tokuyama / 201A	28	25	0.029	[120], [137]
Solvay / Morgane ADP	150	25	0.051	[138]
Fumatech FAA-3-PK-130	130	25	0.0076	[139]

2.7 Objective of Work

In this work, three interconnected studies have been made. In all of them, Pd nanoparticles were synthesized and tested for the EOR in an attempt to increase the catalytic activity of the catalyst towards ethanol electrooxidation in alkaline media. The main objective of this research was to develop highly active and stable Pd-based nanocatalyst deposited on various supports for the EOR in alkaline media, to study their physicochemical properties, to evaluate their electrocatalytic activity in 1M KOH by means of electrochemical techniques and to evaluate the resulting catalyst in an alkaline ethanol fuel cell.

In order to do so, Pd nanoparticles are deposited on various supports (using two different techniques: metallic ion reduction and atomic layer deposition) having shown promising potential for the EOR such as: SnO_2, CeO_2, TiO_2, TiO_2-nts, SnO_2/TiO_2-nts and graphene. The nanocatalysts were characterized using different physicochemical characterizations such as: X-ray diffraction, X-ray photoelectron spectroscopy, scanning and transmission electron microscopy and atomic force microscopy in order to understand their compositions, oxidation states and morphologies. Electrochemical techniques such as: cyclic voltammetry, chronoamperometry, CO stripping and PdO reduction were used in order to observe the effect of the support on reaction rate of ethanol at the catalyst surface. Also, the effect addition of different Ni content to Pd nanoparticles deposited on graphene will be tested in an attempt to promote the EOR. The ultimate goal was to test the best performing catalyst in an alkaline ethanol fuel cell that was designed and built for this purpose using a commercially available AEM from Fumatech.

Chapter 3 : The Role of Metal Oxide Support on Catalytic Activity of Pd Nanoparticles for Ethanol Electrooxidation in Alkaline Media

3.1 Introduction

The development of highly efficient catalysts for ethanol oxidation in alkaline media can be achieved by different means which does not necessarily include changing the composition of the metal catalyst. As discussed before, the nature of a catalyst's support can have an immense effect on its catalytic behaviour. In this chapter, nanostructured catalytic systems were synthesized by the in-situ deposition of Pd nanoparticles on different metal-oxide particle supports using a simple one-step deposition technique and compared to Pd/C synthesized using the same technique. Catalysts with a high metallic loading of 50 wt%, in order to increase the catalytic system's conductivity, were produced by the reduction of Pd^{2+} ions in an aqueous medium using $NaBH_4$ as a reducing agent obtaining Pd nanoparticles with a narrow size distribution and of similar shape on all supports as assessed by X-ray diffraction (XRD) and transmission electron microscopy (TEM). The X-ray photoelectron spectroscopy (XPS) spectra of Pd3d peaks for all supports have shown that the Pd electron density increases with an increasing reducibility of the support modifying the catalytic activity of the nanocatalysts. The best performing electrocatalyst was found using different electrochemical techniques in alkaline media and was then tested in a direct alkaline ethanol fuel cell (DAEFC) using a commercially available anion exchange membrane (AEM). Results are presented in **Chapter 7**.

3.2 Experimental Section

3.2.1 Nanoparticles Synthesis

The palladium-support nanocatalytic systems were synthesized by in-situ reduction of Pd ions on the nanostructured supports using $PdCl_2$ (Fisher Scientific 99.99 %) as precursor salt and $NaBH_4$ (Acros Organics 98 +%) as a reducing agent. First the Pd precursor salt was dissolved in 5 mL of deionized water (Millipore Milli-Q 18 Ωcm) and 100 µL of HCl (Fisher Scientific 36.5-38%), since $PdCl_2$ is soluble in water only at low pH, to obtain a complete dissolution. After complete dissolution, the volume of the solution was increased to 50 mL with deionized water and one of the following supports was added: carbon black > 99 % (Cabot Vulcan XC72), tin oxide (SnO_2) 99.5 % (NanoArc), titanium oxide (TiO_2) ≥ 96.5 % (Kronos 2073) and cerium oxide (CeO_2) 99.5 % (Alfa Aesar) in order to obtain of nominal loading of Pd of 50 wt% on the support (assuming that all the Pd is deposited on the support). The aqueous mixture of Pd salt and support powder was stirred until a homogeneous suspension was obtained. A 2 wt% aqueous solution of $NaBH_4$ with a stoichiometric excess of 100 % was prepared shortly before the synthesis (in order to prevent hydrogen evolution) which was then added dropwise while the solution was stirred. The addition of $NaBH_4$ to the suspension produced a black colour which was caused by the reduction of Pd^{2+} ions to metallic Pd following **Eq. 3.1**. The resulting suspension was then stirred for 15 min to ensure complete reduction of the Pd^{2+} ions. The catalysts obtained were then washed twice with deionized water and twice with ethanol (Fisher Scientific 99%) the mixture was centrifuged after each washing cycle and the supernatant was removed. After the last wash cycle the particles were dried in a freeze dryer.

$$\boldsymbol{2\,NaBH_4 + Pd^{2+} + 2\,Cl^- \rightarrow 2\,NaCl + Pd_{(M)} + B_2H_6 + H_2} \qquad \mathbf{3.1}$$

3.2.2 Physicochemical Characterizations

3.2.2.1 X-ray Diffraction

XRD patterns of deposited Pd nanoparticles were obtained on a RigakuUltima IV diffractometer using a CuKa X-ray source (40 kV, 40 mA). The measurements were made at a scan speed of 0.075 2θ/min and a scan step of 0.02 2θ between 30 and 75 2θ in order to cover the range including the (111), (220) and (200) peaks of crystalline Pd. The average crystallite size of the Pd nanoparticles was calculated using Scherrer equation based on the (111) peak of Pd and the full width at half maximum (FWHM) of the peak.

3.2.2.2 Transmission Electron Microscopy

TEM measurements were performed on a JEOL JEM-1230 instrument with an acceleration voltage of 100 kV. The catalysts powders were dispersed in alcohol and water through ultrasonication. The catalyst powder solution was dropped onto the copper grid coated with a carbon layer and air-dried for TEM measurements. The average particle size was estimated using ImageJ software by counting at least 300 particles per catalyst.

3.2.2.3 X-ray Photoelectron Spectroscopy

XPS was carried out on a Kratos Axis Ultra DLD instrument equipped with a monochromatic Al Kα source. An appropriate amount of catalyst powder dispersed in ethanol was deposited on a piece of Si substrate and then dried for the XPS analysis. In all cases no Si2p peaks were observed showing that the substrate was covered with a relatively thick layer of catalyst. The Pd3d XPS core level spectrum was deconvoluted using XPS PEAK 4.1 software and a fitting routine that decomposes each spectrum into individual mixed Gaussian-Lorentzian peaks using a Shirley background subtraction over the energy range of the fit. Their deconvolution was performed using doublets with spin orbit splitting 5.3 eV and intensity ratio $Pd3d_{5/2}$:$Pd3d_{3/2}$ = 3:2 while a peak asymmetry was used in the case of the Pd3d peak attributed to the metallic state based on the work of Hufner *et al.* [140], [141]. The peak asymmetry of the metallic state was defined by using a sample of pure Pd after reduction under H_2. The binding energy was calibrated using the C1s peak at 284.6 eV as a reference. The accuracy of measurement of the binding energy is ±0.1 eV while that of full width at half maximum (FWHM) is ±0.05 eV.

3.2.3 Electrochemical Characterizations

All electrochemical characterizations were made using a Bio-Logic potentiostat with the EC lab software package. Those measurements were made in a three electrode electrochemical cell (represented in **Figure 3-1**) where the working electrode was a glassy carbon electrode with a surface area of 0.196 cm^2, the counter electrode was a high surface area platinized platinum mesh and the reference electrode was a mercury/mercury oxide (Hg/HgO) electrode connected to the principal compartment using a Luggin capillary to prevent any disturbance in the electrode vicinity. The electrochemical cell was made of an opaque Teflon cylinder having a diameter of 8.6 cm and a height of 9.4 cm which was emptied out providing a working volume of 550 mL. The electrochemical cell was covered by an opaque Teflon lid in order to control the composition of the atmosphere in the working volume and to prevent any UV radiation from entering the chamber which could influence the catalytic activity of the semi-conductor oxide supports (especially TiO_2 which has been known to oxidize organic species when irradiated with UVA) [142], [143]. All electrochemical experiments were made under inert atmosphere by bubbling nitrogen in the electrolyte prior to characterization to prevent reactions between the electrode and dissolved oxygen. **Figure 3-1** shows the dimensions and the configuration of the electrochemical cell previously described.

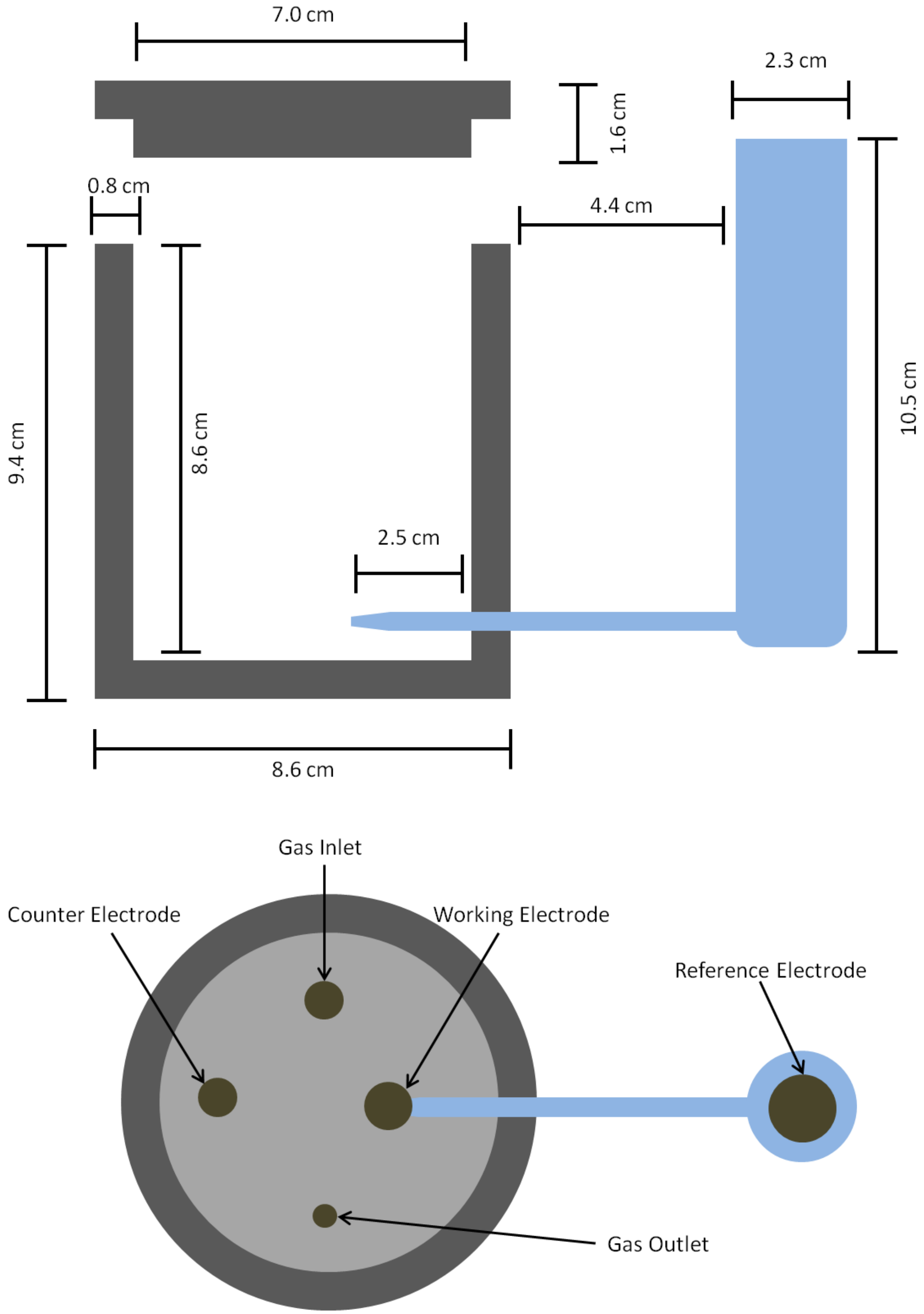

Figure 3-1: Electrochemical cell dimensions and configuration.

For the electrochemical characterizations, a catalyst ink was prepared to deposit nanoparticles on the working electrode for electrochemical measurements. The ink consisted of 6mg of the desired catalyst, 0.6 mL of deionized water (18 MΩ·cm), 60 μL of iso-propanol 99.5 % and 30 μL of 5 wt% Nafion solution (Sigma Aldrich). The ink was sonicated for 10 min to ensure high dispersion and homogeneity, 2.5 μL of the ink was then deposited on the surface of the glassy carbon electrode and air dried for 15 min.

3.2.3.1 Cyclic Voltammetry

Cyclic voltammograms (CV) were made in a solution of 1M KOH between -0.7 and 0.2 V vs. Hg/HgO reference electrode at a scan rate of 25 mVs^{-1}, a potential range that includes hydrogen adsorption/absorption on Pd surface and PdO formation. CVs were also made in a solution of 1 M KOH + 1 M ethanol under the same potential range to observe the catalysts activities for the ethanol oxidation reaction (EOR). In order to compare the activities, the currents observed were normalized by the electrochemical active surface area (ECSA) found using CO stripping. Ten CV cycles were performed for all samples and the last cycle is reported.

3.2.3.2 CO Stripping

The CO stripping experiments made in order to find the electrochemical active surface areas (ECSA) were carried out in a solution of 1 M KOH at a scan rate of 25 mVs^{-1}. First nitrogen was bubbled through the solution for 30 min in order to remove any dissolved oxygen. Then ten cyclic voltammogram (CV) cycles were done in order to obtain a stable and reproducible CV. The potential was then held at -0.55 V vs. Hg/HgO for 30 min while N_2 was bubbled through the solution to have a template of the effect of negative potential hold on the CV scan. Five more CV cycles were then made starting from the holding potential and the first cycle shows the effect of the potential hold in the scan. The potential was then once more held at

-0.55 V for 30 min while bubbling CO for the first 20 min in order to saturate the surface of the Pd nanoparticles with the molecule. Nitrogen was bubbled through the solution for the remaining 10 min to remove any dissolved CO. The potential was then cycled between -0.7 and 0.2 V at a scan rate of 25 mVs^{-1} starting from the holding potential. The CO oxidation peak, found around -0.1 V vs. Hg/HgO on the anodic scan, can then be integrated to find the ECSA of the electrode.

3.2.3.3 Chronoamperometry

Chronoamperometry (CA) measurements were conducted in a solution of 1 M KOH + 1 M ethanol. The potential was first cycled between the same potentials as for the previous electrochemical measurements until a stable CV was obtained. The potential was then held the low current region at -0.6 V on the forward scan for 5 min. The applied potential was then stepped directly to -0.2 V, where a high current density could be observed for all samples, for 1 h in order to study the behaviour and stability of the catalysts during continuous operation.

3.3 Physical Properties of the Synthesized Nanocatalysts

The synthesized catalysts were characterized using various physicochemical techniques in order to determine their physical properties and chemical compositions. This was done in order to explain the difference in catalytic activities between the Pd nanoparticles deposited on the different supports. The characterizations found in this section allow the calculation and observation of the average diameter of the nanoparticles, the crystallinity of the catalysts, their surface chemical compositions and relative electronic densities.

3.3.1 X-ray Diffraction

XRD is a bulk technique that can supply information concerning the structure and composition of the material studied. The position of the observed peaks can be related to the inter-planar distance of the different crystalline planes, using **Eq. 3.2** [16], [144], which will move accordingly in the presence of an alloy or significant quantum effect.

$$\boldsymbol{n\lambda = 2d\sin\theta} \qquad \mathbf{3.2}$$

Where n is an integer usually equal to 1, d is the spacing between the crystalline planes in Å, λ is the wavelength corresponding to the X-ray used which are usually Cu Kα with a wavelength of 1.54 Å and Θ is the incident angle of the rays on the surface of the crystal for n to become an integer.

XRD measurements were taken in order to find the average particle diameter of the Pd nanoparticles which are presented in **Figure 3-2**. It can be observed that the nanostructured Pd particles have a fcc structure due to the presence of the main (111) peak of Pd detected at 40.08 2θ for all the samples which is typical of bulk fcc Pd metal [145]. Two other characteristic Pd peaks can be observed at 46.5 and 68.2 2θ corresponding to (200) and (220) fcc planes, respectively. The positions of the peaks being those of pure Pd crystals shows that the Pd nanoparticles are composed of pure Pd and not PdO or an alloy. All the other, narrower, peaks observed for the spectra of Pd/TiO_2, Pd/CeO_2 and Pd/SnO_2 [73], [146]–[154] can be attributed to the different crystalline planes present in the different oxide supports particles while carbon does not show any peak due to its amorphous nature [155]. The broadening of the XRD peaks of nanoparticles can be attributed to various effects. However, the broadening for nanoparticles larger than 5 nm is mainly caused by the size of the nanoparticles while the other effects can be neglected [156]. The average crystallite diameter can be found using the FWHM of the (111) XRD peak in the Scherrer equation (**Eq. 3.3**) which yields the volume weighted average particle size due to the fact that being a bulk technique the effect of particles containing more matter will be larger than that of particles containing less matter [157]. The crystallite sizes of the particles found from the XRD diffractograms using the Scherrer equation are 7.5, 9.5, 10.8 and 15.2 nm for Pd NPs supported on SnO_2, CeO_2, carbon and TiO_2, respectively.

$$\tau = \frac{K\lambda}{\beta\cos\theta} \tag{3.3}$$

Where τ is the average crystallite size of the nanoparticles in Å, K is a dimensionless shape factor varying with the shape of the particles and is equal to 0.94 for spherical particles, λ is the wavelength corresponding to the X-ray used which are usually Cu Kα with have a wavelength of 1.54 Å, β is the FWHM of the broadened peak in radians and θ is the Bragg's angle position of the peak without taking in account the instrument broadening which will give a slightly smaller particle size than it should.

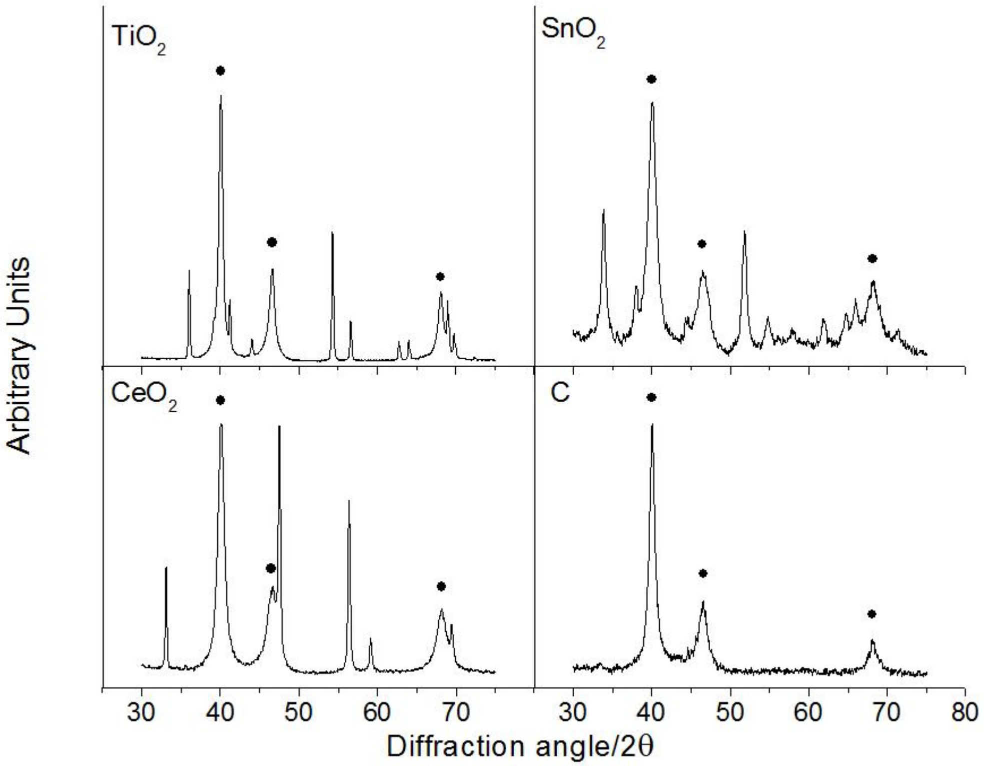

Figure 3-2: XRD patterns of Pd nanoparticles supported on various supports as indicated. Symbol (•) correspond to Pd face-centred cubic (fcc) reflections.

3.3.2 Transmission Electron Microscopy

The magnification of a material using optic microscopy is limited by the wavelength of the photon source used which is typically between 400 and 700 nm (visible light). This magnification can be calculated using **Eq. 3.4.**

$$\boldsymbol{d = \frac{\lambda}{2n\sin\theta}} \qquad \textbf{3.4}$$

Where d is the resolution that can be obtained in nm, λ is the wavelength of the photons hitting the sample, n is the refraction index of the lenses and θ is the angle made by a line going perpendicularly through the center of the lens and the sample and a line going from the sample to the extremity of the lens.

By increasing the energy of the photons, hence decreasing their wavelength, beyond those of visible light it is possible to obtain a much higher magnification. By using a focused beam of X-rays with energies of up to 300 KeV it is now possible to obtain magnifications in the sub-nanometre range using TEM.

In **Figure 3-3** we can observe the TEM micrographs for each synthesized nanocatalyst along with the size distribution of the nanoparticles. It can be observed that CeO_2, carbon and SnO_2 are composed of smaller particles which confers them a large a_s while TiO_2 is composed of larger particles decreasing the surface available for the deposition of the nanoparticles. The synthesized Pd nanoparticles are of spherical shape and well dispersed on all the samples. By using a large amount of Pd nanoparticles (over 300) for each catalyst it was possible to calculate the weighted average diameter of the nanoparticles using **Eq. 3.5**.

The small size of the support particles in **Figure 3-3 a), b) and c)** can block reaction sites on the Pd catalyst by surrounding them reducing the amount of surface available per mass of catalyst in the system causing the mass activity of the catalysts to be lower. This surrounding of the catalyst particles by the support can also cause a diffusion issue preventing the evacuation of products from the vicinity of reaction sites resulting in a lower concentration of reagents near the surface of the catalyst. However, in **Figure 3-3 d)** the nanoparticles are deposited on the surface of the support's particles offering a larger portion of their surface area to the reagents while reducing the resistance to diffusion near their surface.

$$d_{VWA} = \sqrt[3]{\frac{\sum_{i=1}^{n} r_i^3}{n}} \qquad 3.5$$

A comparison between the Pd crystalline sizes found using the XRD spectra using the FWHM of the peaks and the volume weighted average diameters of the Pd nanoparticles on the different support is shown in **Table 3-1**. It can be seen that the size of the nanoparticles, calculated from TEM data, on carbon, CeO_2 and SnO_2 are slightly higher than those calculated using the Scherrer equation while the calculated size of the Pd nanoparticles deposited on TiO_2 is just under the XRD value. Since the particle sizes calculated using XRD and TEM are similar for all the samples, which is too small for the particles to contain more than one crystal, it can be concluded that most of the nanoparticles are mono-crystals confirming the absence of grain boundaries.

Table 3-1: Particle characterizations obtained from XRD and TEM data

Catalyst	Crystalline size (nm)[a]	FWHM (degree)	Particle size (nm)[b]	Standard Deviation (nm)	Percentage of Deviation (%)[c]
Pd/C	10.3	0.82	12.6	3.38	18.3
Pd/SnO_2	7.5	1.18	10.4	2.97	27.9
Pd/CeO_2	9.6	0.93	12.3	3.09	22.0
Pd/TiO_2	15.7	0.58	14.2	5.32	- 10.6

a. Found using Scherrer equation and the FWHM of the (111) peak.
b. Calculated using TEM micrographs.
c. Based on value found from TEM.

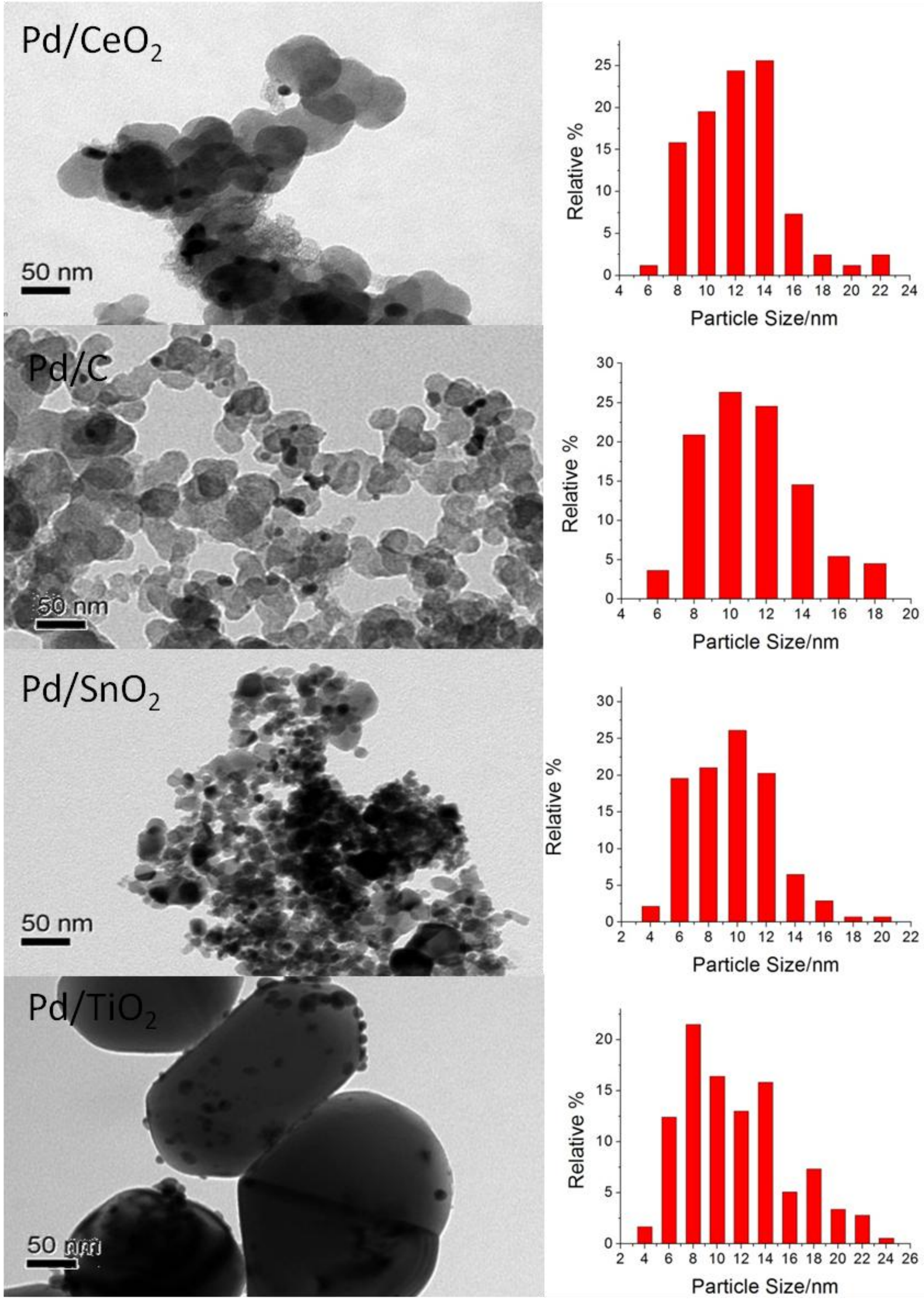

Figure 3-3: TEM images and particle size distribution of the Pd nanoparticles deposited on various supports.

3.3.3 X-ray Photoelectron Spectroscopy

By bombarding a sample with photons having a single, known, wavelength it is possible to eject valence electrons from the surface of the sample. Collecting those valence electrons and calculating their kinetic energy makes it possible to find the amount of energy with which they were bonded to the atom using **Eq. 3.6**.

$$h\nu = E_{kinetic} + E_{binding} + \phi \qquad \textbf{3.6}$$

Where the binding energy ($E_{binding}$) is calculated by subtracting the kinetic energy ($E_{kinetic}$) from the energy of the bombarding photons ($h\nu$) and ϕ is the work function of the spectrometer's detector material which is found and taken into account by instrumental calibration.

Figure 3-4 shows the high resolution Pd3d orbital XPS peak for all four samples. The deconvolution of the Pd3d peaks reveals that the surface layers of the Pd nanoparticles are composed mostly of Pd in the metallic state. However, in the case of Pd/C and Pd/CeO_2, Pd atoms in higher oxidation states and chemical environment are also detected. **Table 3-2** gives a summary of the peaks positions, the FWHM of the deconvoluted peaks, the atomic percentage of atoms in each chemical state and the component to which each peak is assigned.

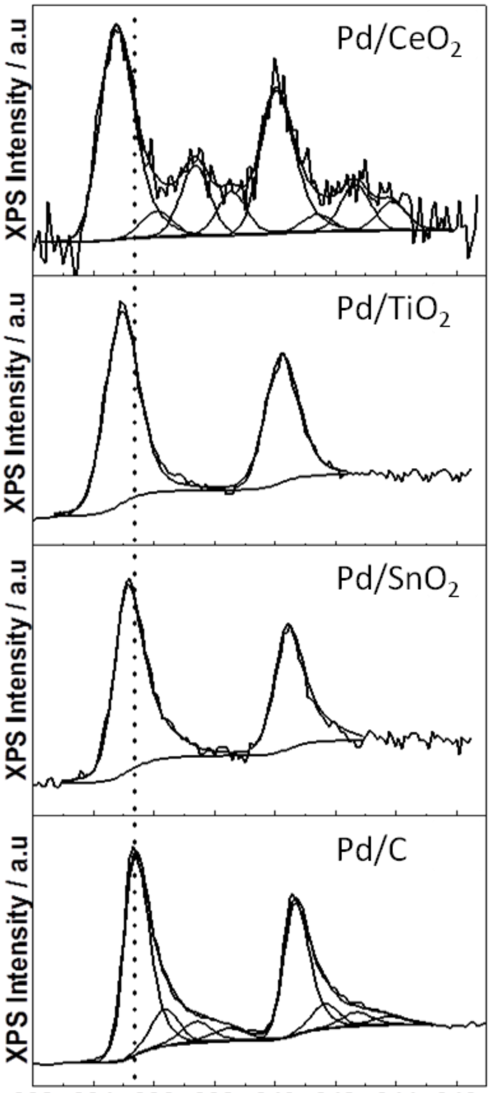

Figure 3-4: Pd3d XPS peak of Pd supported on the different supports.

In the case of Pd/C and Pd/CeO_2, the deconvolution suggests the existence of four distinct peaks situated at 335.4, 336.4, 337.5 and 338.4 eV. The existence of these peaks is supported by their position at the characteristic binding energy of metallic Pd, PdO, PdO_2 and $PdCl_x$, respectively [158]–[161]. The validity of the affirmation of the presence of the four peaks is also supported by the gradual increase in the FWHM of the peaks with increasing oxidation state. The assignment of the Pd-Cl peak positioned at 338.4 eV is supported by the presence of a Pd chloride peak (as shown in **Figure 3-5**) at a binding energy of 199 eV for Pd/C and Pd/CeO_2 while it is absent for Pd/TiO_2 and Pd/SnO_2.The presence of $PdCl_x$ species on the surface of Pd prepared using chlorinated precursors has been reported in literature [162]–[165] and it seems that their presence can be affected by the nature of the support. The removal of chlorine can take place by a reduction pretreatment but still a small amount of chlorine may remain associated [163]. A detailed XPS study of Pd deposited on Fe_3O_4 showed that even after vacuum annealing, chlorine is still attached to the Pd particles [165].

Table 3-2: XPS Pd3d peak data of Pd nanoparticles on various supports

Sample	Pd3d (eV)	FWHM (eV)	Relative content (%)	Assignment
Pd/C	335.4	1.10	71.0	Metallic Pd
	336.4	1.25	13.5	PdO
	337.5	1.35	9.0	PdO_2
	338.4	1.40	6.5	$PdCl_2$
Pd/SnO_2	335.2	1.15	100	Metallic Pd
Pd/TiO_2	334.8	1.2	100	Metallic Pd
Pd/CeO_2	334.6	1.10	64.7	Metallic Pd
	336.1	1.20	9.1	PdO
	337.4	1.25	14.3	PdO_2
	338.4	1.35	9.2	$PdCl_2$

A negative shift of the binding energy of metallic Pd compared to Pd/C can be observed when the nanoparticles are deposited on the surfaced of the metal oxides. More specifically, the metallic Pd peak for Pd/C can be observed at 335.4 eV while it is found at 335.2, 334.8 and

334.6 eV for SnO_2, TiO_2 and CeO_2 respectively. Similar shifts of the Pd3d peak have been reported for Pd deposited on the surface of these oxides [166]. As noted earlier, the analysis of the Pd3d peaks shows that in the case of SnO_2 and TiO_2 supported catalysts the Pd atoms are only present in the metallic state while for the carbon and the CeO_2 supported catalysts, Pd atoms in oxygenated environment (PdO and PdO_2) and in PdClx are also detected. These findings suggest that the nature of the oxide affects the surface composition of the as prepared Pd nanoparticles. However, more studies would be necessary to confirm that the nature of the support plays a role in the chemical composition of the synthesized nanoparticles.

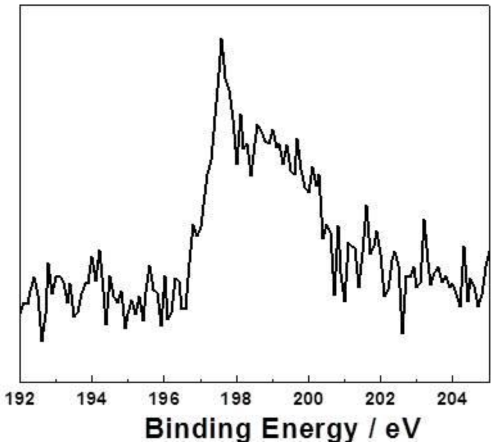

Figure 3-5: Cl2p peak of Pd/C

The XPS spectra of Ce3d, Ti2p and Sn3d are shown in **Figure 3-6** in order to assess their oxidation states. First, in **Figure 3-6 a)**, the Ce3d peak can be observed which gives a rather complex XPS spectrum due to the electron correlation phenomenon. Ce^{4+} has six characteristic peaks (dotted lines) which are known to be situated at binding energies of 882.0, 888.7 and 897.8 eV for the $Ce3d_{5/2}$ peak while the characteristic peaks of $Ce3d_{3/2}$ are separated from their $Ce3d_{5/2}$ counterpart by 18.7 eV towards higher binding energy and are situated at 900.7, 906.9 and 916.1 eV. Ce^{3+} has four different peaks (dashed lines) situated at 880.3 and 885.8 eV for

Ce3d$_{5/2}$ and 18.7 eV higher at 899.1 and 903.5 eV for their Ce3d$_{3/2}$ homologues. The presence of the peaks for Ce^{3+} reveals the presence of cerium atom under the Ce_2O_3 form [167]. The two characteristic Ti2p peaks of Ti are detected at 458.4 and 464.2 eV for Ti2p$_{3/2}$ and Ti3p$_{1/2}$ respectively with a peak separation of 5.8 eV [168] and their positions at higher binding energy than on metallic Ti shows that the oxidation states of the Ti atoms are mostly Ti^{4+}. Finally the characteristic peaks of Sn3d are found at binding energies of 483.8 and 492.4 eV for Sn3d$_{5/2}$ and Sn3d$_{3/2}$ respectively with a peak separation of 8.6 eV. The position of the Sn3d peaks suggests the presence of the Sn atoms primarily in the Sn^{4+} oxidation state [169]. The unusually large FWHM of both Ti2p and Sn3d peaks (>1.4 eV) suggest a shift of the stoichiometry towards lower oxidation states (from MO_2 to MO_{2-X} with X being $0 < X < 1$).

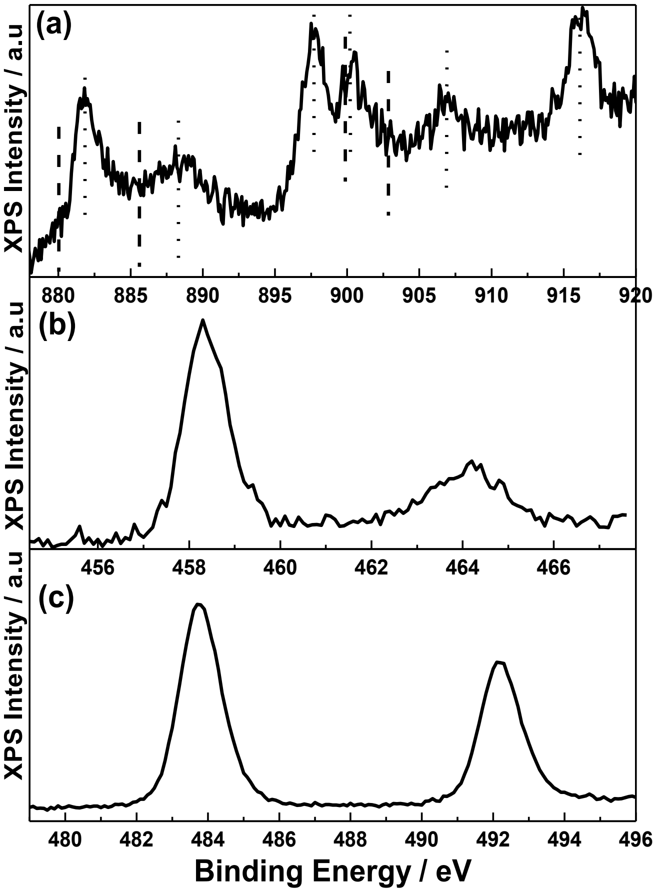

Figure 3-6: XPS peak of: a) Ce3d; b) Ti2p; c) Sn3d.

The most plausible explanation of the observed downward shift in the binding energy of the Pd3d peak is the presence of a metal-support interaction between the support and the Pd nanoparticles where electrons are transferred from the support to the catalyst due to support reduction [170], [171]. Upon contact of two solids with different work functions electrons will be transferred from the solid with a lower work function to the solid with the higher one until the Fermi energy levels of electrons at the interface are equilibrated [172]. Bulk Pd exhibits a work function that is usually found to be between 5.2 and 5.4 eV [173], [174], while it is expected to increase significantly in the case of nanostructured Pd particles as it was shown for Pt in a study presented by Roduner [175]. The work function of SnO_2 has been reported to be around 4.75 eV [176]–[178]. For TiO_2, the work function has been reported to be between 4 and 4.2 eV depending on its crystalline structure and more specifically 4.2 eV for the (110) surfaces of rutile TiO_2 [179]. Finally, the work function of CeO_2 has been reported to be 4.69 eV [180]. The negative shifts of the Pd3d peaks can be explained by an increase of the electron density around Pd nanoparticles due to an electron transfer from the metal oxides with the a lower work function to Pd nanoparticles that happens in order to equilibrate both Fermi levels. The lower the work function of the oxide, the larger would be the Volta potential forcing more electrons to migrate to the Pd inducing a negative charge lowering the binding energy of the electrons of the Pd3d band to the atom's nucleus. Moreover, it is known that in CeO_2 and also in TiO_2 and SnO_2, to a lower extent, the metal sites with oxidation states of 4+ can be reversibly converted to 3+, thus facilitating the release of oxygen vacancy that can interact with Pd nanoparticles increasing their electron density. This change in electron density around Pd nanoparticles will cause a downward shift of the Pd3d peaks on XPS spectra. Both phenomena are suggested to be in part responsible for the shifts of the Pd3d peaks to lower binding energies it is however impossible to assess which of these is dominant with the information obtained.

3.4 Electrochemical Behaviour of the Nanocatalysts

3.4.1 Electrochemical Behaviour in 1M KOH

Cyclic voltammetry in the electrolyte is used to observe at which potential different phenomena will happen on the surface of the electrode containing the studied catalyst. The current obtained from the reaction at the catalyst's surface, positive or negative for oxidation and reduction reactions respectively, are recorded through a potentiostat and plotted as a function of potential difference between the working electrode and the reference electrode. This technique can be useful to detect the formation of an alloy or of a biphase structure by observing peaks shifts, elongation or doublets. It has also been shown [181] that the surface planes or the reaction site coordination also has an effect on the potential at which the different reactions will occur on the surface of metallic electrocatalysts.

Figure 3-7 shows the CVs of the four catalysts in 1 M KOH which correspond to reported CV of Pd in alkaline media with similar electrolyte concentration [26], [59], [66]. Pd nanoparticles are known to have the ability to absorb hydrogen atoms in its bulk structure at low potential [39], [67], [182]–[184], that is why the anodic peak (peak I) situated from the lowest potential boundary up to -0.4 V is attributed to the oxidation of adsorbed and absorbed hydrogen on the surface of Pd nanoparticles. The next peak on the forward scan (peak II), observed between -0.35 V and -0.25 V, is generally attributed to the adsorption of hydroxyl groups on the surface of Pd [16], [39]. Peak III which starts shortly after OH^- adsorption around -0.25 V corresponds to the transformation of the adsorbed species to higher valence oxides (PdO_x) following the reaction pathway shown by **Eq. 3.7 – 3.9** [59]. Due to the fact that the formation of the Pd oxide is a function of both time and potential and that the potential difference is increased continuously over time providing a constant oxidation current peak III is more of a plateau than an actual peak until it later increases at a faster rate due to oxygen evolution. This last region was however avoided in order to limit the crystallographic changes of the Pd nanoparticles [181].

$$\boldsymbol{Pd + OH^- \rightarrow Pd - OH_{ads} + e^-} \qquad \mathbf{3.7}$$

$$\boldsymbol{Pd - OH_{ads} + Pd - OH_{ads} \rightarrow Pd - O_{ads} + H_2O} \qquad \mathbf{3.8}$$

$$\boldsymbol{Pd - OH_{ads} + OH^- \rightarrow Pd - O_{ads} + H_2O + e^-} \qquad \mathbf{3.9}$$

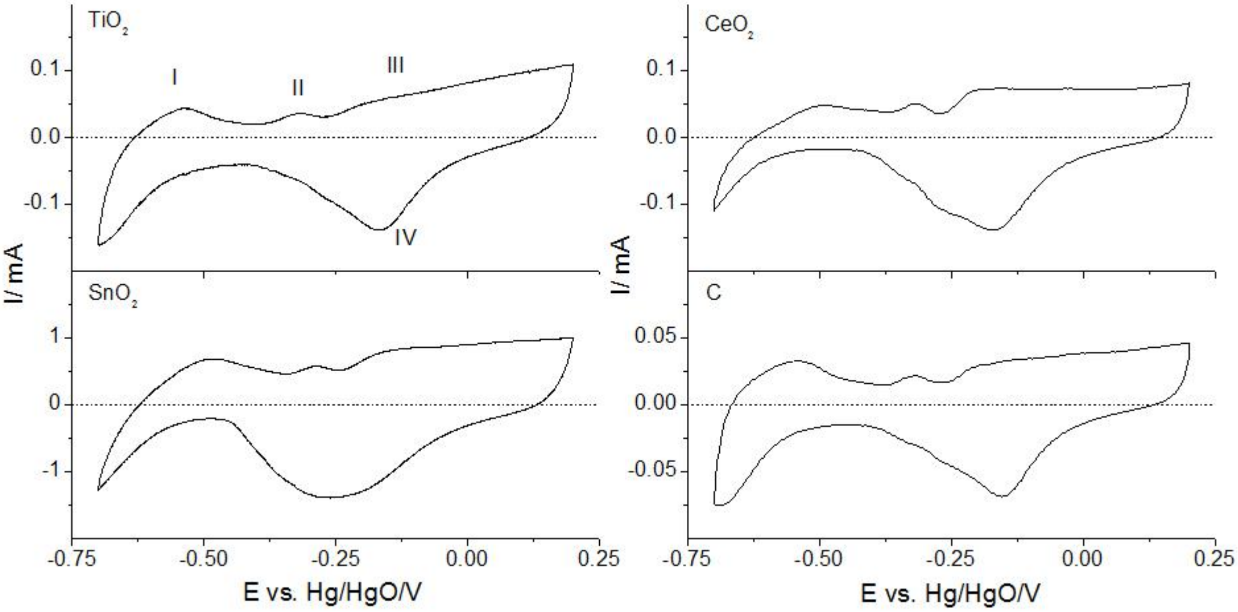

Figure 3-7: CVs of Pd catalysts deposited on the different supports in 1 M KOH. Scan rate 25 mVs^{-1}

The main cathodic peak (peak) IV which has its maximum situated at -0.15 V is caused by the reduction of the PdO$_x$ layer formed on the surface of the metallic Pd nanoparticles during the anodic scan. The shoulders seen on the peak IV can be attributed to the reduction of different oxidation states of Pd atoms on various Pd crystalline planes and on sites with different coordinations. The potential at which the formation/reduction of a metal catalyst oxide was formed/reduced was shown to be affected by the contact of the catalyst with SnO$_2$ [185].

Accordingly, as it can be observed in **Figure 3-7**, the reduction peak of PdO deposited on SnO_2 particles is shifted to lower potential and is broader than the other samples. When the applied potential becomes lower than -0.45 V the cathodic current increases due to a combination of three overlapping phenomena. First, hydrogen is adsorbed on the surface of Pd as a monolayer, then at lower potential Pd diffuses in the lattices of Pd allowing other hydrogen atoms to be adsorbed on the metal surface, finally at even lower potential hydrogen evolution takes place on the surface of the catalyst causing a sharp increase in the observed current. This last effect was mitigated by stopping the cathodic scan at a potential of -0.7 V vs Hg/HgO. Hydrogen absorption into Pd lattice prevents the determination of the ECSA using hydrogen desorption as commonly used for the ECSA determination of Pt electrodes, therefore CO stripping measurements were carried out to evaluate the ECSA of Pd nanoparticles.

3.4.2 Electrochemical Active Surface Area Determination Using CO Stripping

The catalytic activity of a catalyst is calculated in katal (usually abbreviated to *kat*) which is defined as the number of molecules reacted per reaction site per unit of time. By using the ECSA in order to compare the activity of different electrocatalysts it is possible to observe the rate of the reaction in relation with another catalyst without actual activity values. However, other methods such as normalization per mass of geometrical surface allow only the observation of the catalytic properties of the catalyst as a whole and not of individual reaction sites. These latter methods give information as to which catalyst would give the best performance for the lowest cost or amount of material by taking account of the size of the particles, the amount of surface available and how well the reagents/products can diffuse from/to the catalyst from the bulk solution. On the other hand, the normalization of the observed activity of the reaction by

ECSA offers the chance to observe the effect that the catalyst's support has on the actual catalytic activity. Further modification of the catalyst geometry and particle size would then be made to optimize the mass activity of the catalyst while keeping their increased catalytic activity.

There are various methods to calculate the ECSA of a metal catalyst. The most common ones are hydrogen oxidation, carbon monoxide oxidation, metal oxide reduction and double layer capacitance. The more commonly used method is the oxidation of a hydrogen layer formed on the surface of the catalyst, however, the capacity of Pd to absorb hydrogen in its lattice at potentials overlapping the adsorption of hydrogen prevents the use of such a technique. The calculation of the ECSA using the double layer capacitance of a catalyst is possible when using colloids or pure metal but for deposited nanoparticles the addition of the double layer capacitance of the support makes this calculation more complicated. The use of the reduction of a monolayer of metal oxide is possible in these conditions but it is less precise, takes more time and the data analysis is more complicated. For these reasons, the oxidation of a monolayer of carbon monoxide (CO stripping) was used to determine the ECSA of the different samples.

First, the potential applied to the sample is cycled between the same potential as for CV in 1 M KOH until a stable CV is obtained. The potential applied is then kept to a point where hydrogen will be oxidized and CO molecules will poison the catalyst when it is in the electrolyte solution. By increasing the potential of the electrode saturated with CO the molecules will be oxidized and removed from the surface of the catalyst. By integrating the oxidation peak observed using **Eq. 3.10** and knowing that the charge required for the electrooxidation of a full monolayer of CO on the surface of a Pd surface is 420 μCcm^{-2} [54], [186] it is possible to find the ECSA (using **Eq. 3.11**) of the electrode which corresponds to the real Pd surface area that is available for catalytic reaction. Holding the potential does not only cause the adsorption of CO but also a charging of the double capacitance layer of the catalyst. In order to find which part is caused by the oxidation of CO the potential was held for the same amount of time than for CO stripping in the presence of N_2 in order to charge the double capacitance layer and observe the CV response. **Figure 3-8** shows the CO stripping data obtained for Pd/CeO_2. The full grey line represents the stable CV cycle obtained before the CO stripping experiments. The dashed grey line shows the CV cycle after the potential was held in N_2 atmosphere depicting the effect of the charging of the double capacitance layer on the current recorded by the potentiostat. The full black line is the first cycle after the potential was held in the presence of CO and the difference between this cycle and the cycle after the potential held in a N_2 atmosphere is caused by the CO oxidation. The dashed black line is the second cycle after CO oxidation which shows, by its similarity to the stable cycle, that all the carbon monoxide was completely removed during the first forward scan.

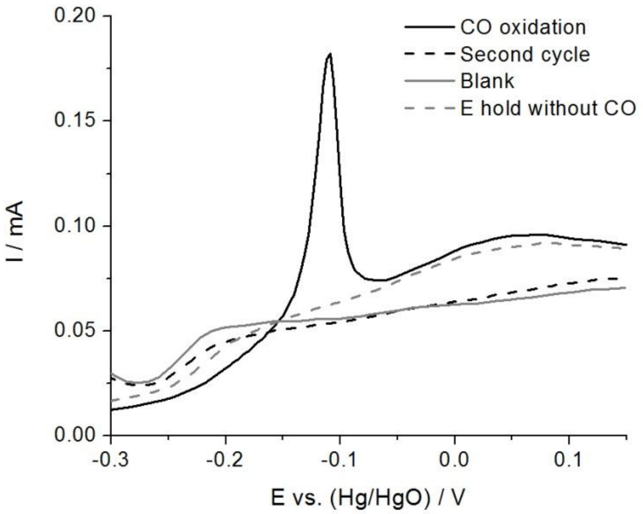

Figure 3-8: CO Stripping of Pd/CeO_2 where are shown the first and second cycle, the double layer capacitance effect and a stable CV.

$$Q = \frac{\int_{E_1}^{E_2} I_{CO\ Stripping} dE - \int_{E_1}^{E_2} I_{DLC} dE}{v} \tag{3.10}$$

$$ECSA = \frac{Q}{420 \, {}^{\mu C}/_{cm^2_{Pd}}} \tag{3.11}$$

Where Q is the charge calculated from the CV in µC, $I_{CO\ Stripping}$ is the current of the scan corresponding to the CO stripping region in mA, I_{DLC} is the current caused by the double capacitance layer in mA, E is the potential difference in V and ν is the scan rate in $mVcm^{-2}$.

Figure 3-9 shows the first and second CV cycles of CO oxidation in 1 M KOH on the surface of the four Pd nanocatalysts. The CO oxidation peak can be observed between – 0.2 V and 0 V on all samples. The charges observed under the CO stripping curves (highlighted area in **Figure 3-9**) for CeO_2, TiO_2, carbon and SnO_2 calculated using **Eq. 3.10** ranged from 0.15 mC to 0.39 mC. The calculated charge and ECSA of the catalysts and the a_s of the support are summarized in **Table 3-3** for each sample. It can be observed that the ECSA is not affected by the a_s of the support on which it is deposited. The currents observed for ethanol electrooxidation were normalized per the ECSA found using this technique.

Table 3-3: ECSA of the 4 different catalysts and physical properties of the supports.

Catalyst	**CO Stripping Charge / mC**	**ECSA / cm^2**	**Support particle size / nm**	**a_s / m^2g^{-1}**
Pd/C	0.101	0.24	50	237
Pd/SnO_2	0.063	0.15	22 - 43	20-40
Pd/TiO_2	0.104	0.24	>200	< 5
Pd/CeO_2	0.164	0.39	15 - 30	35-50

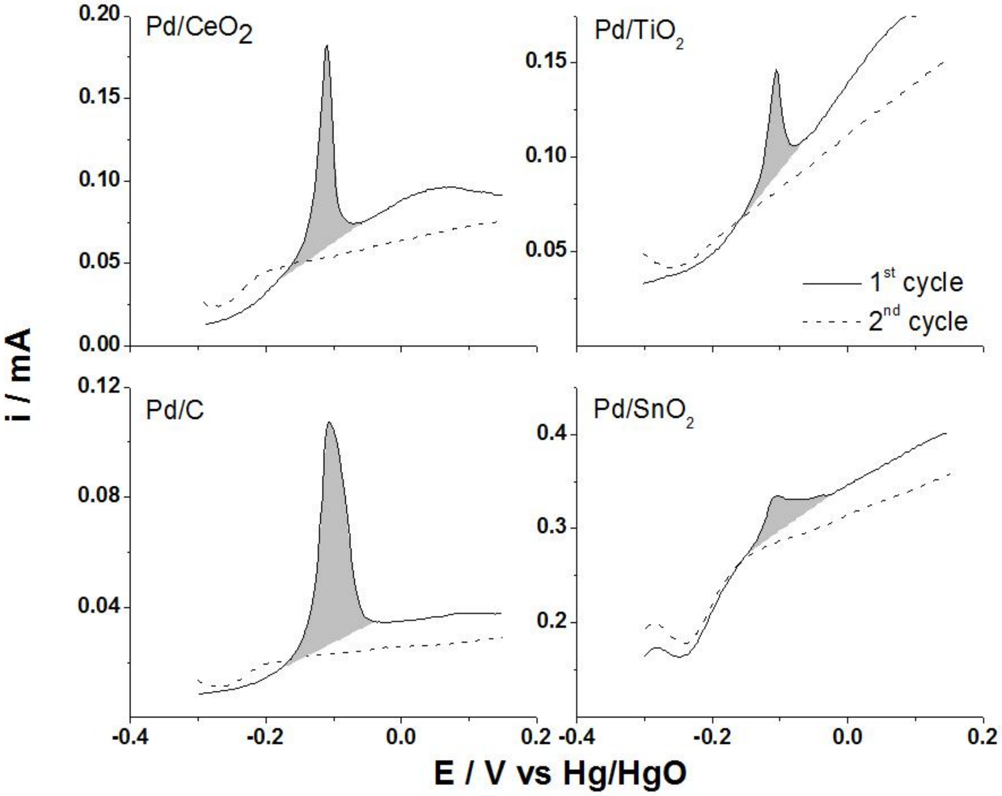

Figure 3-9: The first and the second cycle (forward scan) of CO stripping voltammograms for the different Pd catalysts. The peak area used for ECSA calculation is highlighted.

3.4.3 Electrooxidation of Ethanol on the Surface or the Nanocatalysts

Cyclic voltammetry in the presence of a fuel in an electrolyte makes it possible to observe how the fuel reacts on the surface of an anode catalyst. When the ethanol oxidation current is normalized by ECSA the catalysts can be compared in terms of the reaction rate per units of Pd surface. An increase in this activity for nanoparticles synthesized using the same technique would suggest a promoting effect caused by the catalyst support.

Figure 3-10 shows a stable cycle (10th) of CVs recorded in 1 M KOH + 1 M ethanol normalized by the ECSAs calculated in **Section 3.2.3.2** which are presented in **Table 3-3** for each nanocatalyst. It is possible to observe that Pd/C has a lower maximal current density on the forward scan while Pd/CeO_2 and Pd/TiO_2 have much larger current densities with Pd/SnO_2

situated at an intermediate level. Goodenough et al. [187] suggested that the peak observed on the reverse scan is caused by the removal of partially oxidized intermediates formed on the surface of the catalyst. Therefore, the ratio of the intensity of the ethanol oxidation peak on the forward scan to the intensity of the backward scan (I_f/I_b) gives a gross approximation of the amplitude of the surface coverage of the catalyst by carbonaceous species after the anodic scan [188]. A low I_f/I_b would indicate that the catalyst shows an accumulation of adsorbed intermediates on its surface leading to a lower stability during constant operation due to poisoning of reaction sites by strongly adsorbed carbonaceous species. On the other hand, a higher I_f/I_b would indicate that the electrode is less prone to be poisoned by strongly adsorbed intermediates probably due to lower adsorption strength. It can be observed in **Table 3-4**, along with other characteristics of the CVs in 1 M KOH + 1 M ethanol, that while Pd/CeO_2 has a I_f/I_b comparable to that of Pd/C, Pd/TiO_2 and Pd/SnO_2 have a much higher I_f/I_b than Pd/C showing that both of these catalysts are less prone to being poisoned leading to a lower amount of poisoning and a theoretically higher stability during long term operation. This higher ratio may be due to a metal support interaction effect, which weakens the adsorption strength of ethanol and intermediate species on the Pd surface [48], which can provide oxygenated species for the oxidation of adsorbed molecules.

Table 3-4: Summary of electrochemical parameters from CVs in 1 M C_2H_5OH + 1 M KOH solution

Catalyst	I_f/I_b	Onset potential / V vs Hg/HgO	Current density at -0.2 V / $mAcm^{-2}$	Maximum peak position / V vs Hg/HgO
Pd/C	0.73	-0.512	8.1	-0.111
Pd/SnO_2	0.97	-0.607	17.3	-0.083
Pd/TiO_2	1.03	-0.613	21.3	-0.102
Pd/CeO_2	0.68	-0.596	18.1	-0.025

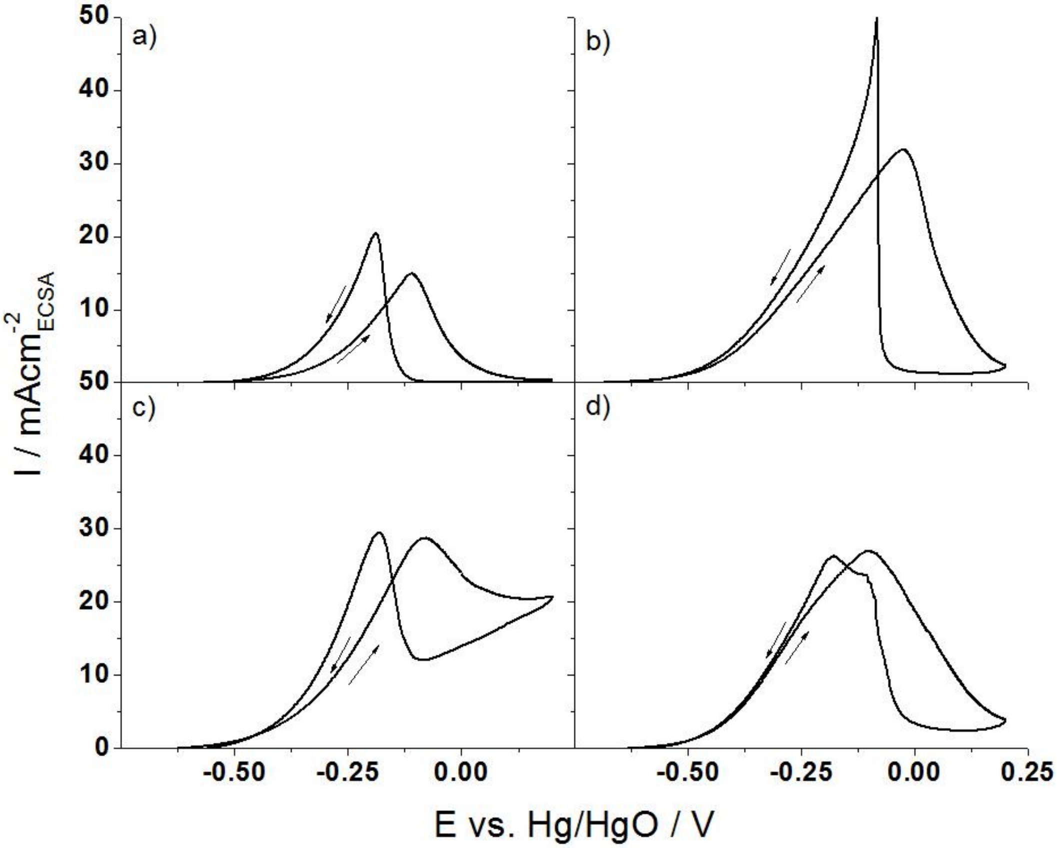

Figure 3-10: CVs of Pd catalysts in 1 M KOH + 1 M ethanol at a scan rate of 25 mV s^{-1}: a) Pd/C; b) Pd/CeO$_2$; c) Pd/SnO$_2$; d) Pd/TiO$_2$. Current densities are given per ECSA.

Figure 3-11 shows the LSV of the four catalysts in the potential region of -0.65 V and -0.15 V which is the potential of interest for fuel cells where the potential difference between the electrodes is still significant enough to have high power density. Pd/C has the lowest current density per ECSA between all the samples in the whole potential range showing that the reaction rate of ethanol oxidation on its surface is the lowest of all the synthesized catalysts. The current density of Pd/TiO$_2$ and Pd/CeO$_2$ catalysts is the same up to -0.43 V. However, Pd/TiO$_2$ has the highest current densities than all other catalysts at higher anodic potentials. The EOR onset potential of Pd/C is found around -0.512 V while it is significantly more negative at -0.596, -0.607 and -0.613 V for Pd/CeO$_2$, Pd/SnO$_2$ and Pd/TiO$_2$, respectively. This decrease in onset potential indicates that the overpotential of oxidation of ethanol on the surface of the catalysts is much lower than that of carbon. This lower potential is probably caused by the lower adsorption strength of ethanol, a higher coverage of the catalyst surface by hydroxyl groups and from the oxidation of adsorbed molecules using oxygenated groups supplied by the support at the 3-phase boundary.

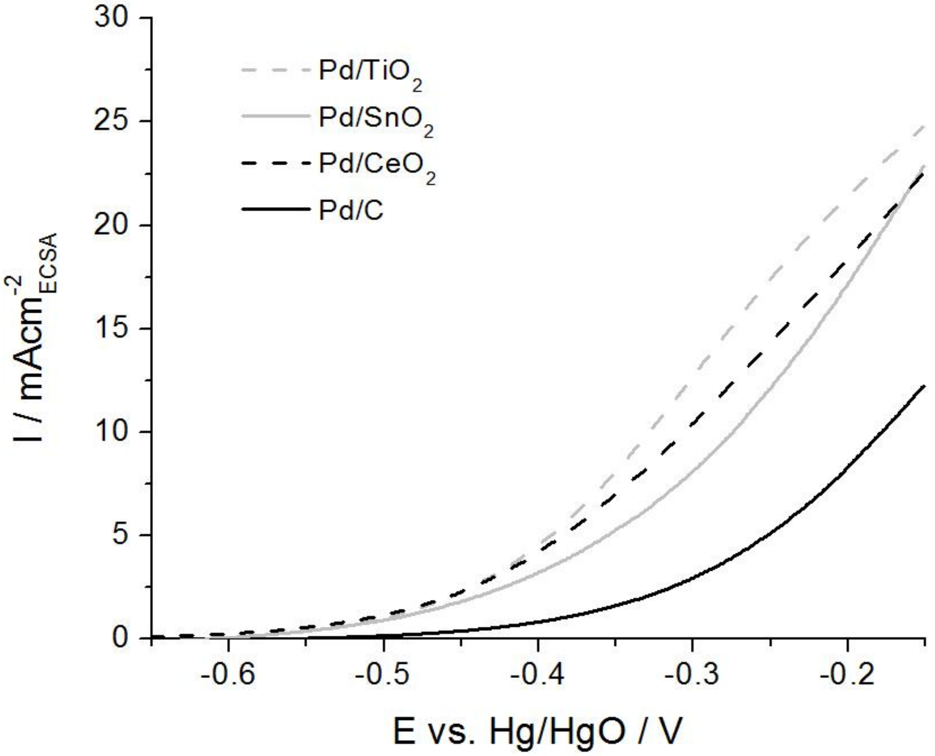

Figure 3-11: Linear sweep voltammetry of the different catalysts in 1 M KOH + 1 M ethanol at a scan rate of 25 mVs^{-1}.

It is known that in alkaline media adsorbed carbonaceous species such as ethanol and its oxidation intermediates reacts with neighbouring hydroxyl species adsorbed on the surface of the catalyst. This effect has been shown in a few studies where the adsorption strength of ethanol on metal surfaces was shown to be weakened by a neighbouring hydroxyl group. Indeed, Chibani et al. [189] have shown that the adsorption energy of ethanol was lowered from -0.34 eV to

-0.89 eV on Pt sites neighbouring an adsorbed hydroxyl group. This drop in adsorption energy is attributed to a hydrogen bond formed between the adsorbed hydroxyl group and the hydroxyl group present on the ethanol molecule reducing the electron density of the adsorbed ethanol molecule hence modifying its attraction with the metal catalyst. A similar phenomenon has been simulated by Kavanagh et al. [31] who obtained a value of -0.95 eV for the adsorption of the combined molecule on the surface of Pt (111). The similarity between Pt and Pd (being a transition metal of the same family) suggests that a similar effect would be observed on a Pd surface.

The increase in current density observed for the EOR on the catalysts deposited on the metal oxides supports can be in part attributed to a higher coverage of their surface by hydroxyl species. This higher coverage by hydroxyl groups can be either on the Pd nanoparticles due to a lower Pd electron density caused by the metal support interaction (as discussed in **Section 3.3.3**) leading to a faster adsorption of hydroxyl groups or it can be caused by an increase in hydroxyl groups on the surface of the support near the metal-support interface which could react with an ethanol molecule on a neighbouring active catalyst reaction site. As a matter of fact, rutile TiO_2 has been shown to offer a very high density of hydroxyl groups on its surface in alkaline media being able to reach up to $6.2*10^{14}$ atom cm^{-2} [78]. This also suggests that rutile TiO_2 would have a more beneficial effect on the catalytic system than anatase TiO_2 as it can have a hydroxyl group surface density of more than 4 times higher [78], [79]. The hydroxyl group surface densities of SnO_2 and CeO_2 were experimentally found to be 3.4 and $4.3*10^{14}$ atom cm^{-2} respectively [190]. It is observed that the activity of the catalyst increases with a higher concentration of hydroxyl groups on the surface of its support.

3.4.4 Chronoamperometry

Chronoamperommetry is used in electrochemistry to obtain information on the behaviour of a catalyst under constant potential in the operating media and the reaction rate on its surface. A constant potential in the region of interest is applied and the current obtained is recorded and plotted over time. This technique can give different information on the behaviour of the catalysts in the solution under this potential. For example, a higher current density per ECSA for a catalyst signifies that the molecules attached to the surface are oxidized and replaced at a faster rate than on samples showing a lower current density. Also, the amplitude of the derivative of the curve of current density versus time (di/dt) is a good indication of the stability of the catalyst as a higher absolute value could indicate a catalyst that could be either unstable in the operating media at the potential applied or slowly becoming covered by strongly adsorbed carbonaceous intermediates reducing the amount of reaction sites available (poisoning).

The chronoamperograms of the four synthesized catalysts in a solution of 1M KOH and 1M ethanol under an applied potential of -0.2 V vs Hg/HgO for 1 h are presented in **Figure 3-12** while their current densities and di/dt after 1h can be found in **Table 3-5**. The current density observed for Pd/C is significantly lower than all the other metal-oxide deposited Pd catalyst for the whole hour of operation. It is also possible to observe that the current density recorded is not stable after an hour and still decreases at a constant rate. This behaviour is expected for Pd deposited on carbon black as it was shown that carbon black was not very stable in an alkaline [191] environment meaning that the catalyst will be degrading over time slowly losing its catalytic activity. Poisoning of the catalyst surface may also play an effect in this constant decrease in current density as it was shown previously that the I_f/I_b ratio was low compared to Pd/TiO_2 and Pd/SnO_2 suggesting a higher level of poisoning. Pd/SnO_2 shows a relatively low current density compared to the other metal oxide containing catalysts but its stability is reached fast (about 1000 s) after which no decrease in current density can be observed. The high stability of the catalyst makes it a good candidate for potential long term application. The current density of Pd/CeO_2 is higher than the previous two catalysts. However, its current density continues to decrease at a constant rate after the first hour and will most likely drop below that of Pd/SnO_2 after a few hours showing a limited stability for ethanol oxidation. In this case the constant decrease in activity after the first hour is most likely due to gradual poisoning of the surface of the catalyst by carbonaceous intermediate as it was suggested by the low I_f/I_b since CeO_2 is known to have a high stability in alkaline media [192], [193]. Finally, Pd/TiO_2 has the highest current density of all the samples during the full hour of operation and shows a good stability towards the end of the test period. This high current density and stability makes Pd/TiO_2 the best candidate for fuel cell applications. It can be observe that the current density of the different catalysts containing metal-oxides after prolonged operation increases following the surface density of hydroxyl groups on the support.

Table 3-5: Properties of the chronoamperograms for all catalysts

Catalyst	di/dt / $mAcm^{-2}_{ECSA}h^{-1}$	Current density at -0.2 V after 1 h / $mAcm^{-2}$
Pd/C	2.16	3.9
Pd/SnO_2	0	5.6
Pd/TiO_2	0.72	10.8
Pd/CeO_2	1.80	8.8

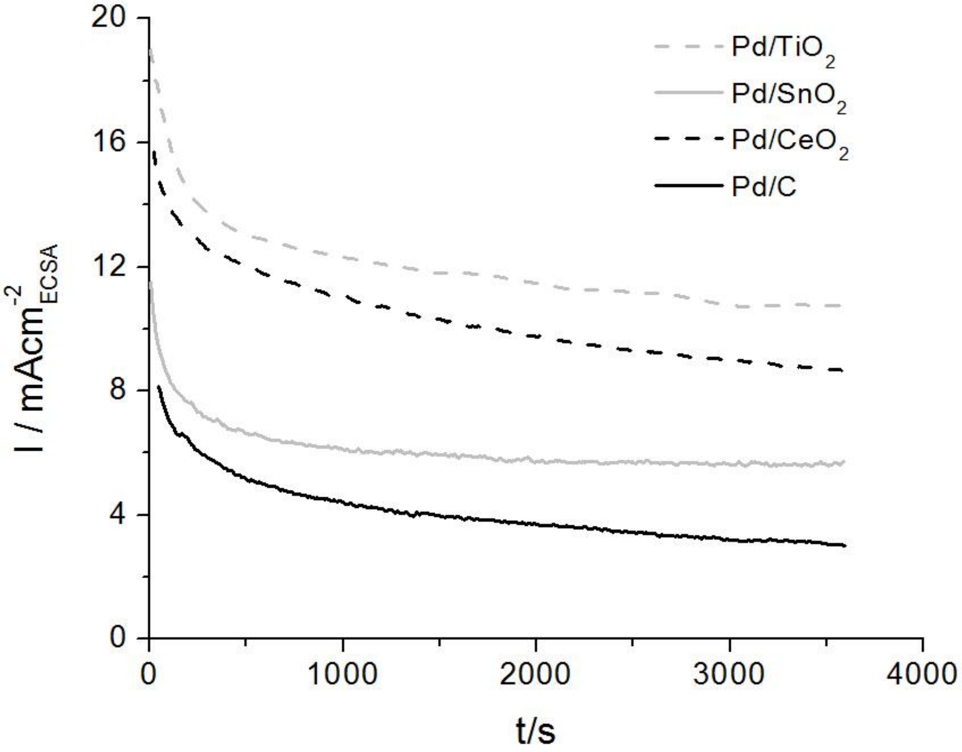

Figure 3-12: Chronoamperograms of Pd catalysts at -0.2 V vs Hg/HgO in 1 M KOH + 1 M ethanol.

3.5 Conclusions

The results presented in this study show that the metal oxide supports have a promoting effect on the electrocatalytic activity of Pd for the EOR. A simple synthesis method was used to prepare Pd nanoparticles, which were deposited in-situ on the surface of different reducible metal oxides (CeO_2, TiO_2 and SnO_2) and on a conventional carbon support. XRD showed that the synthesized Pd nanoparticles have an fcc structure similar to bulk Pd. TEM micrographs helped to confirm the crystalline size found using XRD which ranged between 7 and 15 nm. The XPS spectra of the supported Pd demonstrated a shift to lower binding energy of the Pd3d peak for Pd NPs deposited on oxides and this shift increases as the reducibility of the oxide support increases as $SnO_2 < TiO_2 < CeO_2$, due to a charge transfer from the oxide supports to Pd nanoparticles resulting in a higher electron density in the Pd nanoparticles. It was found that the current density of ethanol electrooxidation on Pd deposited on these oxide supports was up to twice as large as for Pd/C. The oxide-supported Pd nanoparticles also show a higher stability during constant potential operation indicating increased EOR kinetics. These increases in activity are proposed to be caused by a joint effect. First, the EOR would be promoted by an increase in the surface density of hydroxyl groups either on the surface of the Pd nanoparticles or at the metal-support interface and by oxygen ions provided by the reducible oxides. Secondly, the modification of the Fermi level of Pd caused by a larger Volta potential between Pd nanoparticles and their oxide supports than between Pd and carbon resulting in a higher electron density of the Pd nanoparticles would modify the adsorption strength of the ethanol molecules and the oxidation intermediates resulting in a change of reaction rate on the surface of the catalyst. Overall, it was found that TiO_2 offered the highest catalytic activity with a high stability making it a good candidate for alkaline ethanol fuel cells.

3.6 Acknowledgements

I would like to acknowledge Dr. Chialiang Sun and his team (Chang Gung University in Taiwan) for the TEM and XPS measurements were performed in their facility. I also acknowledge Dr. Spyridon Ntais (University of Ottawa) for the interpretation and analysis of the XPS data.

Chapter 4 : Atomic Layer Deposition of Pd Nanoparticles on TiO_2 Nanotubes for Ethanol Electrooxidation in Alkaline Media

4.1 Introduction

In the present chapter Pd nanoparticles were grown on the surface of titanium dioxide nanotubes (TiO_2-nts) using atomic layer deposition (ALD) and the obtained samples were tested for their activity towards the electrooxidation of ethanol in alkaline media. In the previous chapter it was shown that TiO_2, used as a support, could increase the activity of Pd nanoparticles for the EOR due to an increase in electron density of Pd caused by a relatively large Volta potential. Ti can be oxidized electrochemically in a controlled manner in order to form a highly uniform three dimensional array of nanotubes. This structure offers a theoretically very high surface area available for metal catalyst deposition due to its morphology. It is expected that, using ALD, a thin, uniform, layer of metallic Pd could be deposited on all the surfaces of the TiO_2-nts offering a high electrochemical active surface area (ECSA) possessing a high electrochemical activity towards the ethanol oxidation reaction (EOR) due to a metal-support interaction mechanism. By varying the Pd loading on the synthesized electrodes an optimal Pd loading can be obtained. Also, in order to improve the catalytic activity, the structure of the supports can be modified by annealing the obtained nanotubes in air in order to increase its crystallinity. The physical properties of the synthesized catalysts were studied using various physicochemical techniques such as scanning electron microscope (SEM), transmission electron microscope (TEM), atomic force microscope (AFM) and X-ray diffraction (XRD). The activities of the catalysts toward the EOR were studied using cyclic voltammetry and chronoamperometry in an alkaline media containing a constant concentration of ethanol and were normalized by ECSA and geometrical surface area (GEO) in order to assess the activity of individual sites and of a fixed geometrical surface which is more of a practical approach.

4.2 Experimental Section

4.2.1 Nanocatalysts Synthesis

4.2.1.1 TiO_2 Nanotubes Formation

The TiO_2-nts catalyst supports were electrochemically grown from a titanium foil (Advent, 95.6 % purity) in the presence of fluoride ions in an aqueous electrolyte. The TiO_2-nts were grown in a Teflon electrochemical cell using a 3-electrode configuration with a potential/galvanostat (Modulab Solartron Analytical). A Pt mesh was used as the counter electrode while a mercury/mercury sulphate reference electrode ($Hg/HgSO_4$) and a Ti foil of 2 cm X 2 cm X 0.1 cm were used as reference and working electrode respectively. The electrolyte in which the TiO_2-nts were grown was composed of a buffer solution that was made as a solution containing 1 M of NaOH and 1 M of H_3PO_4. The intake of fluoride ions was made by the addition of 0.5 wt% of HF to the buffer solution. The TiO_2-nts were grown at room temperature under an applied potential difference of 20 V between the counter and the working electrodes. The period of anodization was 1 h in order to grow nanotubes with lengths of about 1 μm.

The TiO_2-nts as formed were amorphous. An annealing post-treatment carried out at 450°C in air for a period of 2 h forced them to transfer to the anatase configuration making them polycrystalline and giving them a higher electronic conductivity. Both as grown (amorphous) and polycrystalline TiO_2-nts were studied as catalysts support for ethanol electrooxidation on Pd nanoparticles in alkaline media.

4.2.1.2 Atomic Layer Deposition of Pd nanoparticles

The catalysts were synthesized by ALD in a Fiji 200 reactor from Ultratech/Cambridge Nanotech. Pd clusters were deposited from palladium hexafluoroacetylacetone ($Pd(hfac)_2$) (STREM Chemicals, 99 % in purity) and formalin (formaldehyde 37 wt% in methanol, Sigma Aldrich). The Pd external canister was maintained at 90°C and it was connected to an Ar booster in order to improve the vapour content of $Pd(hfac)_2$ while the formalin canister was kept at ambient temperature due to its high vapour pressure. The pulsing of Ar directly into the Pd canister allows a better vapourization of the precursor and a better transport of the species toward the reaction chamber. The tube leading from the canister to the reaction chamber was maintained at 150°C while the chamber temperature was kept at 200°C. The gas vector for the purge of the reaction chamber was Ar (Linde, 5.6 in purity).

The ALD sequence, in exposure mode, was 0.25 s pulse Ar with booster in the $Pd(hfac)_2$ canister to increase the airborne concentration of $Pd(hfac)_2$ which was followed by 1 s of pulsing Pd in the reaction chamber where it was exposed to the substrates for 30 s and any unreacted material was pumped out of the reaction chamber for 15 s. Formalin was then pulsed for 3 s in the reaction chamber and let react for 15 s before being evacuated from the reaction chamber for 15 s. The overall process takes about 80 s per cycle. The supports were exposed to reagents for a total of 100 to 1000 cycles. The deposition of Pd nanoparticles has been performed on both TiO_2-nts and flat Si (100) substrates in order to facilitate some characterizations.

4.2.2 Physicochemical Characterizations

4.2.2.1 Scanning Electron Microscopy

The morphology and shape of Pd nanoparticles were characterized by scanning electron microscopy (SEM) using a JEOL 6320F microscope. The Pd/TiO_2-nts samples were inserted as is in the SEM instrument after being thoroughly washed using a pure ethanol solution.

4.2.2.2 Transmission Electron Microscopy

TEM and high resolution transmission electron microscopy (HRTEM) measurements were performed on a JEOL 6320-F instrument. A few drops of ethanol were deposited on the surface of the Pd/TiO_2-nts which was subsequently scratched in order to separate the nanotubes from the surface of the Ti plate. A drop of the ethanol solution containing the broken nanotubes was pipetted from the Ti plate and deposited on a copper grid coated with a carbon layer and air dried.

4.2.3 Electrochemical Characterizations

The electrochemical characterizations were performed using a BioLogic potentiostat/galvanostat with the EC lab software package. The characterizations were performed in 1 M KOH to observe the behaviour of the catalysts in the electrolyte and in 1 M KOH + 1 M ethanol to assess their catalytic activities towards the EOR. The current density obtained from CV and CA in 1 M KOH + 1 M ethanol were normalized by the ECSA and by the geometrical surface area exposed to the solution for comparison. The characterizations were made in a small cylindrical Teflon electrochemical cell of an internal height of 2.2 cm and diameter of 2.6 cm for a total capacity of 11.7 mL whose layout can be seen **Figure 4-1**. The working electrode was exposed to the solution at the bottom of the cell and the connection was made from underneath by an Ag wire. The reference electrode used was a mercury/mercury oxide (MMO) electrode

(20 Mol %) (Koslow) while the counter electrode was a large surface area platinized Pt mesh. All electrochemical experiments were made under inert atmosphere by bubbling N_2 in the electrolyte prior to characterization in order to prevent reactions between the electrode and dissolved oxygen. The scan rate used for cyclic voltammetry was 25 mVs^{-1} unless otherwise stated. Chronoamperometry measurements were made by holding the potential at -0.6 V vs. MMO for 5 min before jumping directly to -0.2 V for 1 h. The ECSA was determined by the integration of the reduction peak of a monolayer of PdO from the surface of the catalysts in H_2SO_4 0.5 M using a mercury/mercury sulphide (MSE) reference electrode.

4.2.3.1 Cyclic Voltammetry

CVs were made in a solution of 1 M KOH between -0.7 and 0.4 V vs. Hg/HgO, a potential range that includes hydrogen adsorption/absorption on Pd surface and PdO formation. CVs were also made in a solution of 1 M KOH + 1 M ethanol under the same potential range to observe the catalysts activities for the EOR. In order to compare the activities, the currents observed were normalized by the ECSA found using PdO reduction and by the geometrical surface area exposed. Ten CV cycles were performed for all samples using a scan rate of 25 mVs^{-1} and the last cycle is reported.

4.2.3.2 PdO Monolayer Reduction

The PdO reduction took place in a solution of 1 M H_2SO_4 due to the fact that the potential at which PdO reduction and hydrogen adsorption take place overlap on the surface of Pd in an alkaline medium while they happen at distinct potential in acidic media [194]. To obtain the plot of the charge of the reduction peak vs the maximum potential the maximal potential applied was varied between 0.8 and 1.6 V vs MSE. For all the potential range the lower bound was kept at 0.0 V. First, the potential was cycled 5 times between 0 and 0.8 V were the potential was then held for 120 s after which it was cycled back to 0 V. The potential was then held at 0.1 V higher for 120 s and cycled back. This method was repeated until a maximum potential of 1.6 V vs MSE was reached.

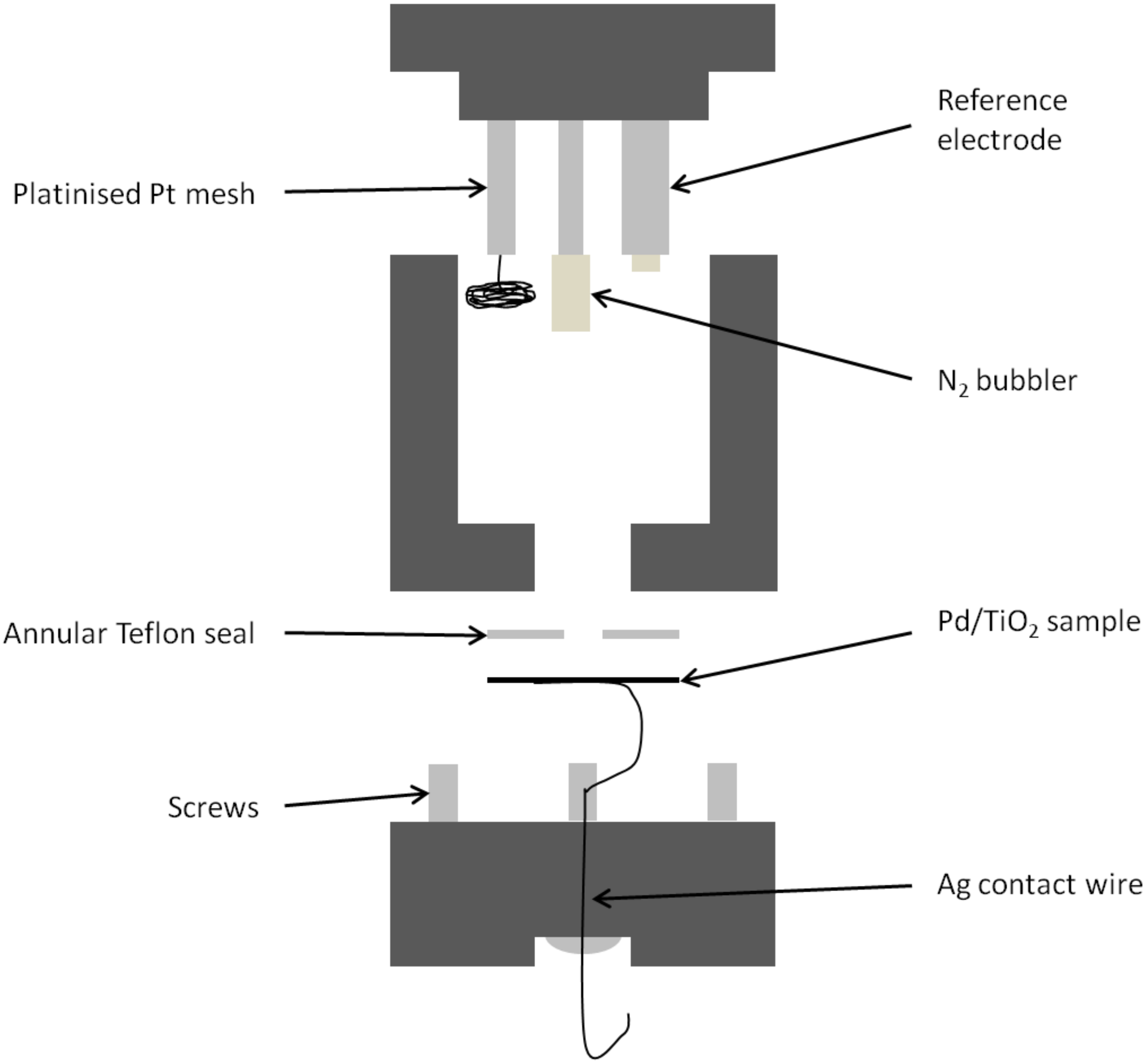

Figure 4-1: Electrochemical cell layout.

4.3 Physical Properties of Nanocatalysts

4.3.1 Atomic Layer Deposition of Pd Nanoparticles

ALD is a thin film deposition technique that can be used to cover a substrate uniformly and with very high control. It is a self limiting technique in the sense that two separate steps are necessary for the growth of a monolayer of the desired deposit. The substrate is exposed to a first precursor which will saturate the surface of the substrate with a single layer. This precursor is then ejected from the chamber which is purged with an inert gas (usually argon) to remove any remaining precursor. A second precursor is inserted in the reaction chamber which will react with the adsorbed monolayer and adsorb onto the surface creating new reaction sites for the first precursor. The chamber is then evacuated and purged once more. This cycle is repeated over and over and by varying the number of cycles it is possible to control with high precision the amount of material deposited on the substrate.

Figure 4-2 a) shows the mass gain of the initial growth phase of Pd deposited by ALD using a quartz crystal microbalance (QCM). At a low number of cycles, a non-linear low growth can be observed which progressively increases until it reach a constant growth rate at a higher number of cycles. This low mass gain at low cycles has been attributed to the long nucleation phase of Pd and the poisoning of the substrate surface by the precursor ligands [195], [196]. **Figure 4-2 b)** shows a close-up of one complete cycle of ALD which can be separated in four distinct steps.

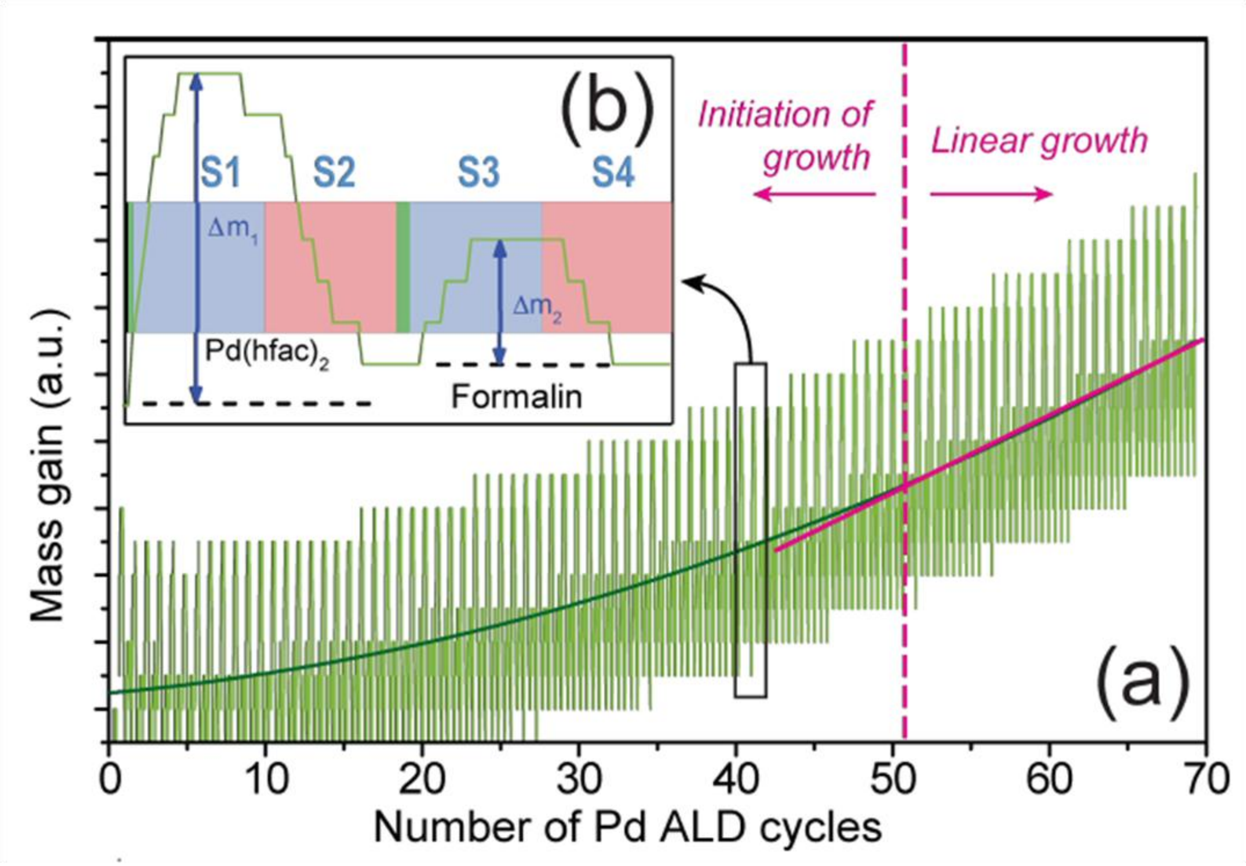

Figure 4-2: In-situ QCM measurements of the initial growth phase of Pd mass gain during the ALD process a) a general evolution and b) a single ALD cycle [195]**.**

The mass gains and losses observed during a single ALD cycle of Pd deposition can be attributed to the reactions in the four steps represented in **Figure 4-3**. For the first deposition cycle $Pd(hfac)_2$ will react with an hydroxyl group on the surface of the oxide (to increase these number of reactive sites a pretreatment with hydrogen peroxide is often used) where the Pd atom is attached to the oxygen of the hydroxyl group while the hydrogen leaves as a H-hfac specie resulting in the molecule observed in step 2. The surface is then exposed to a second precursor (formaldehyde) in step 3 by which Pd(hfac) is reduced. In step 4 H_2, CO and H-hfac are released leaving a –Pd–H termination where $Pd(hfac)_2$ can react again in subsequent cycles.

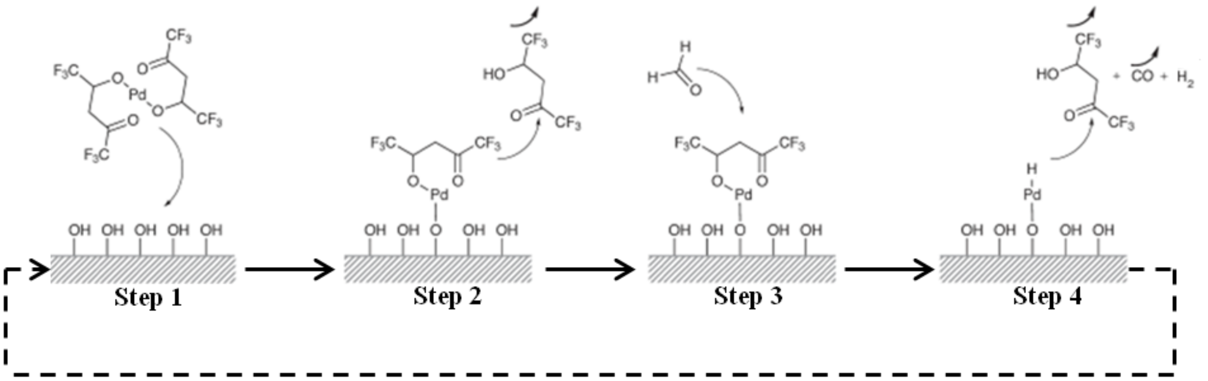

Figure 4-3: Representation of the 4 steps of ALD deposition of Pd using Pd(hfac)$_2$ and formaldehyde [195].

4.3.2 TiO_2 Growth and Geometry

Highly organized and well defined TiO_2 nanotubes can be synthesized in liquid media in the presence of fluorine ions by applying a potential difference between a counter electrode and a Ti foil. The morphology of the TiO_2-nt can be affected by various factors such as the current applied which will affect the thickness of the oxide layer, the viscosity of the electrolyte which will affect the shape and length of the nanotubes and the time of anodization which will also affect the length of the nanotubes until steady state is reached. By manipulating these variables, it is possible to control the growth and geometry of the nanotubes [197].

Figure 4-4 represents the evolution of TiO_2 from the metallic Ti foil to fully grown TiO_2-nts supported on Ti foil. The formation of TiO_2-nts is represented by three characteristic regions in the chronoamperogram of the Ti foil anodization as shown in **Figure 4-5**. In the first region at the very beginning of the anodization a layer of TiO_2 following **Eq. 4.1** [198], [199] is formed at the surface of the Ti foil and the sharp decrease in current observed is caused by an increasing resistivity of the thickening oxide layer. The thickness of the layer formed at an applied potential of 20 V is around 50 nm [200]. After the formation of this initial oxide layer, the ions in the solution will migrate through this oxide layer to react at the oxide-metal interface. The Ti^{4+} ions migrate from the oxide-metal interface to the electrolyte where they are dissolved.

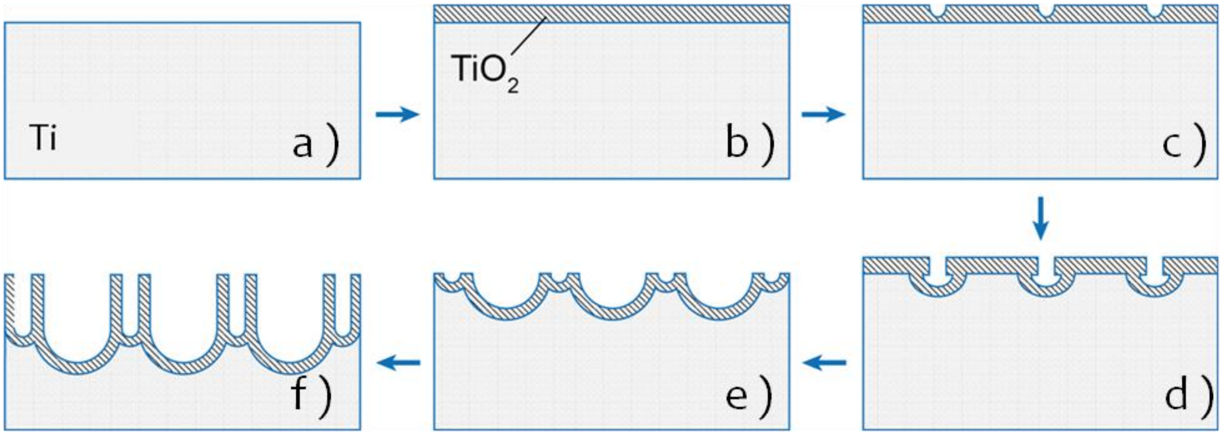

Figure 4-4: Evolution of the TiO_2 layer on the surface of the Ti foil during anodization [198].

It is at this point that the fluorine ions come into play to induce the tubular shape observed in TiO_2-nts. Those ions will start etching the surface of the oxide layer in the electrolyte and those sites will act as the starting points for the formation of the nanotubes. This etching of the TiO_2 surface by fluorine ions can be represented by the reaction showed by **Eq. 4.2** [198], [199]. The distance between the metal surface and the electrolyte will be lower where the etching of the oxide surface has started to take place reducing the resistance to the current between the electrolyte and the metal. It is at this stage that the phase II of **Figure 4-5** takes place. The increase in current is caused by the increase in ion transfer through the oxide layer due to this decrease in resistance. By increasing the rate of ion transfer near those points of etching they become a preferential point for future reaction with the electrolyte creating holes in the oxide surface as shown in **Figure 4-4 c)**. The oxide layer under the points of etching will then start to go deeper in the Ti film creating vertical tunnels in the Ti film coated with a layer of TiO_2 as shown in **Figure 4-4 d)**.

$$Ti + 2H_2O \rightarrow TiO_2 + 4e^- + 4H^+ \tag{4.1}$$

$$TiO_2 + 6F^- + 4H^+ \rightarrow TiF_6^{2-} + 2H_2O \tag{4.2}$$

When the pores have reached the depth of the oxide layer we enter the phase III of **Figure 4-5** where the current decreases slowly and will eventually reach a steady state. When the depth of the nanotubes is small the rate of etching by fluorine ion is faster than the rate of Ti^{4+} leaving the metal-oxide interface allowing the progression of the phenomenon deeper in the metal foil. When the TiO_2-nts reach a certain depth an equilibrium is reached between the rate of Ti^{4+} leaving the metal-oxide interface and the rate of etching at the surface of the oxide layer due to diffusion restriction [198], [199]. At this point a longer anodization time will not lead to longer nanotubes but only to a constant dissolution of the nanotubes surface with an increasing nanotubes depth.

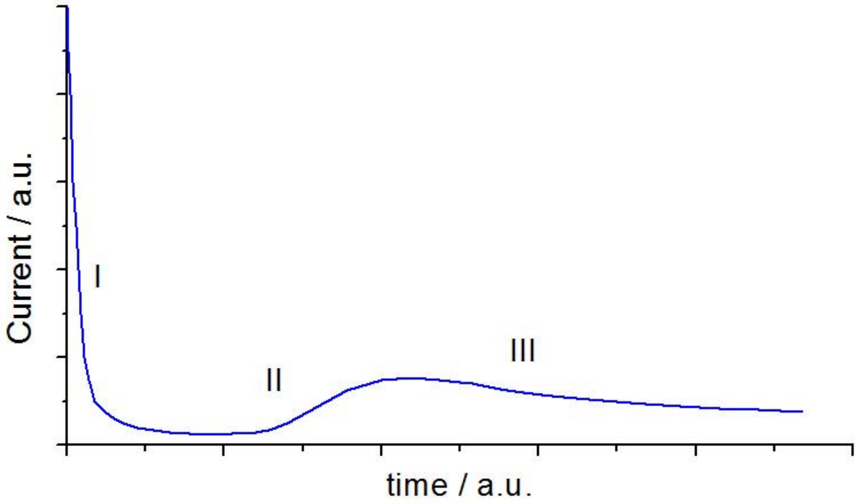

Figure 4-5: Representation of the current obtained during anodization of the Ti foil to produce TiO_2-nts using arbitrary units with the 3 characteristic regions identified.

4.3.3 Microscopy

4.3.3.1 Bare TiO_2-nanotubes

Bare TiO_2-nts were grown by anodization of a Ti foil in aqueous solution and were analysed using SEM and TEM microscopes. These images are shown in **Figure 4-6** and allow us to observe the morphology of the grown nanotubes both from the surface and from their profile.

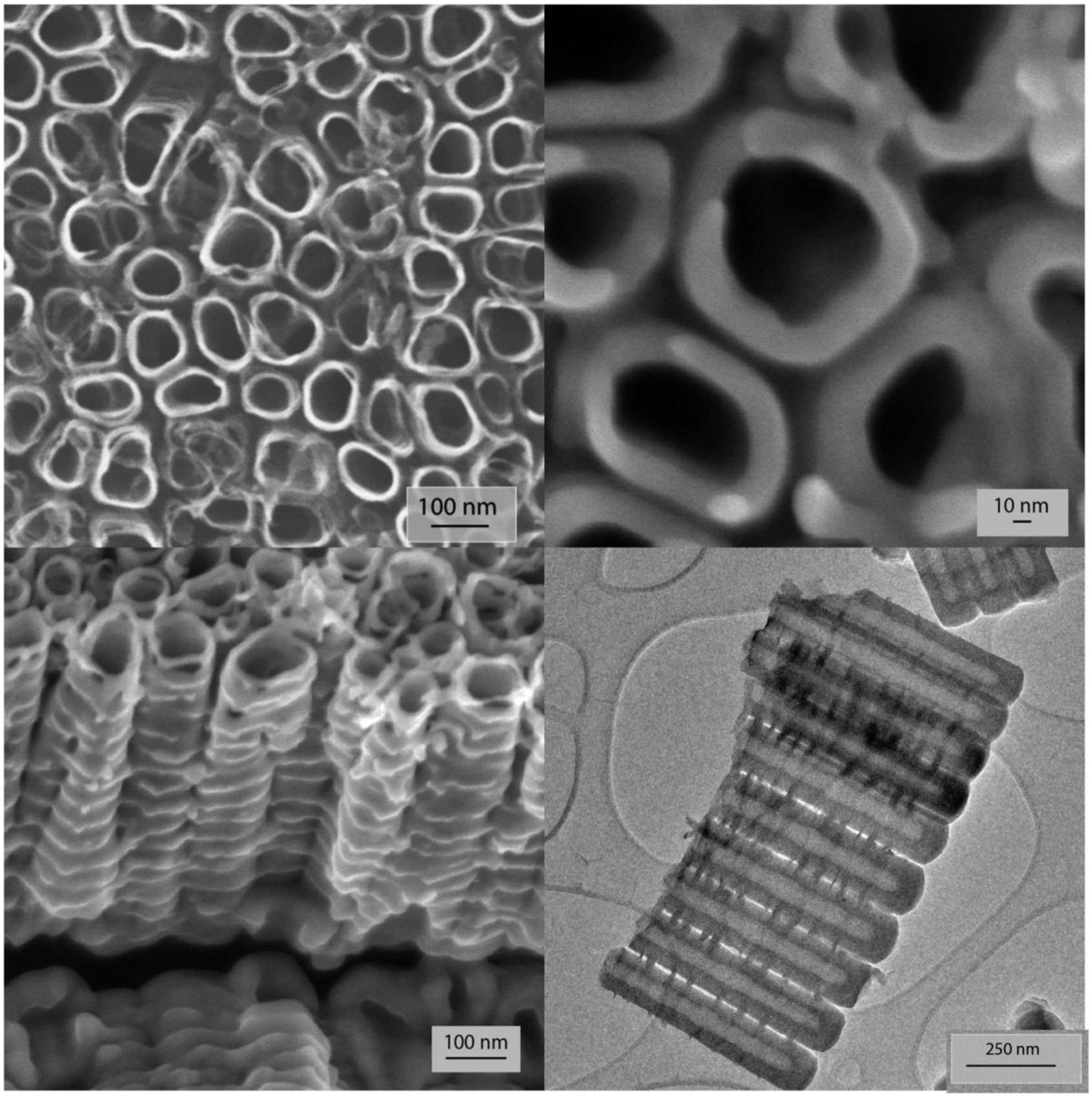

Figure 4-6: (top left) Top view of as grown TiO_2-nts using SEM, (top right) Close-up of top view of as grown TiO_2-nts using SEM, (bottom left) Side view of the as grown TiO_2-nts using SEM and (bottom right) Side view of the bottom part of a broken section of as grown TiO_2-nts using TEM.

Figure 4-6 a) and b) show the configuration of the nanotube array from a top view at two different magnifications. In these images it is possible to observe that the nanotubes opening are well defined with an average internal diameter estimated to be about 70 nm with an average wall thickness of around 15 nm giving them an external diameter of roughly 100 nm which is characteristic of the electrolyte used and applied potential [200]. A large amount of interstitial space can also be observed providing a very high theoretically available surface for catalyst deposition. **Figure 4-6 c)** shows the nanotubes arrays from a side view still attached to the Ti surface. A well defined tubular shape can be observed for each individual nanotube with ripples on their surface connecting them together. The length of the nanotubes has been measured to be approximately 1µm which is not observed on this image due to the camera angle. **Figure 4-6 d)** shows a TEM image form the side of the bottom part of a single layer of nanotube connected in a chain by small interstitial bridges. The round bottom of the nanotubes is characteristic of the oxide-metal interface while the lighter portion in the middle of the nanotubes shows that the interiors of the nanotubes are well defined all the way to their bottom.

Figure 4-7 compares the geometry of the TiO_2-nts before and after annealing in air at 450°C for 1 h. There is no significant difference in the geometry of the nanotubes caused by annealing as predicted by previous research [201]–[203]. However, while the geometry of the nanotubes is not affect various studies have shown the apparition of a crystalline phase (anatase) at temperatures exceeding 300°C from an amorphous configuration [199], [201]–[203]. The anatase phase of TiO_2 is known to offer larger electronic conductivity than an amorphous phase [199] by increasing the electron transport and possibly the reaction rate at the surface of the catalyst. Annealing at temperatures higher than 600°C shows the formation of a rutile phase but the TiO_2-nts were shown to collapse at such temperatures [199], [201]–[203] due to a sintering process [199].

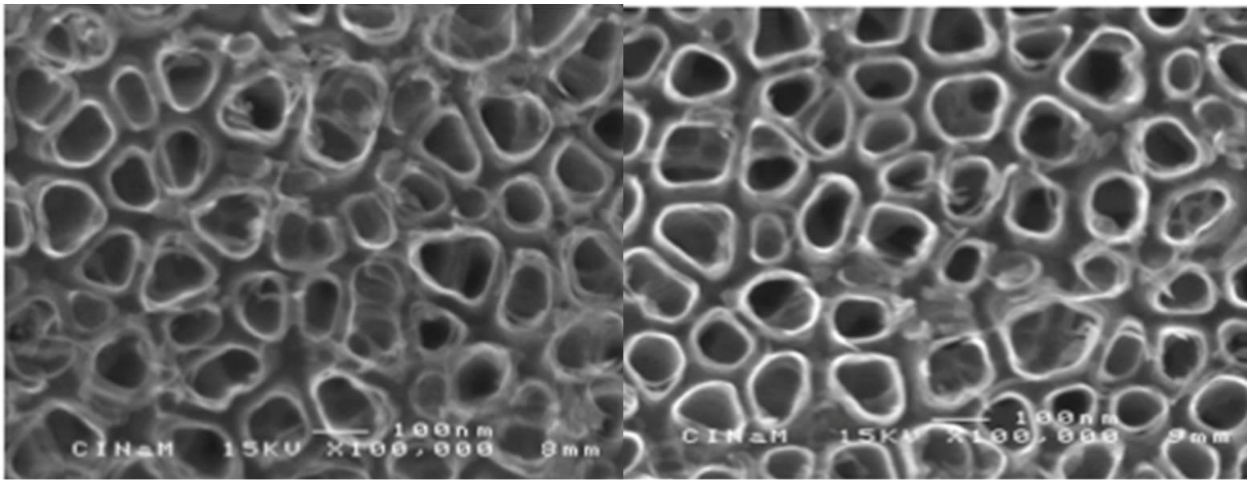

Figure 4-7: Bare TiO_2-nts grown for 1 h under a potential of 20 V as grown (left) and annealed (right)

4.3.3.2 Pd/TiO_2-nanotubes

After the synthesis of the TiO_2 nanotubes Pd nanoparticles were grown using ALD with loading varying between 100 and 900 ALD cycles of Pd on both as grown and annealed TiO_2. **Figure 4-8 a) to f)** shows SEM pictures of the deposition of Pd nanoparticles with an increasing amount of ALD cycle corresponding to 100, 400, 500, 700, 800 and 900 cycles respectively. It is possible to observe that the size of the nanoparticles is very small for a low number of cycles and seem to grow from nucleation sites rather than by the formation of a complete surface layer. An increase in the number of ALD cycles results, as expected, in an increase in Pd particle size. Up to 700 cycles the particles are still spherical and distinct from one another. At loading starting at 800 cycles the nanoparticles loses their general shape due to contact and agglomeration with neighbouring particles which causes growth restrictions. The growth of the nanoparticles past 700 ALD cycles and the particle agglomeration seems to cause a blockage of the interstitial space between the nanotubes and of a part of the Pd nanoparticles surfaces reducing significantly the surface area for catalytic reaction.

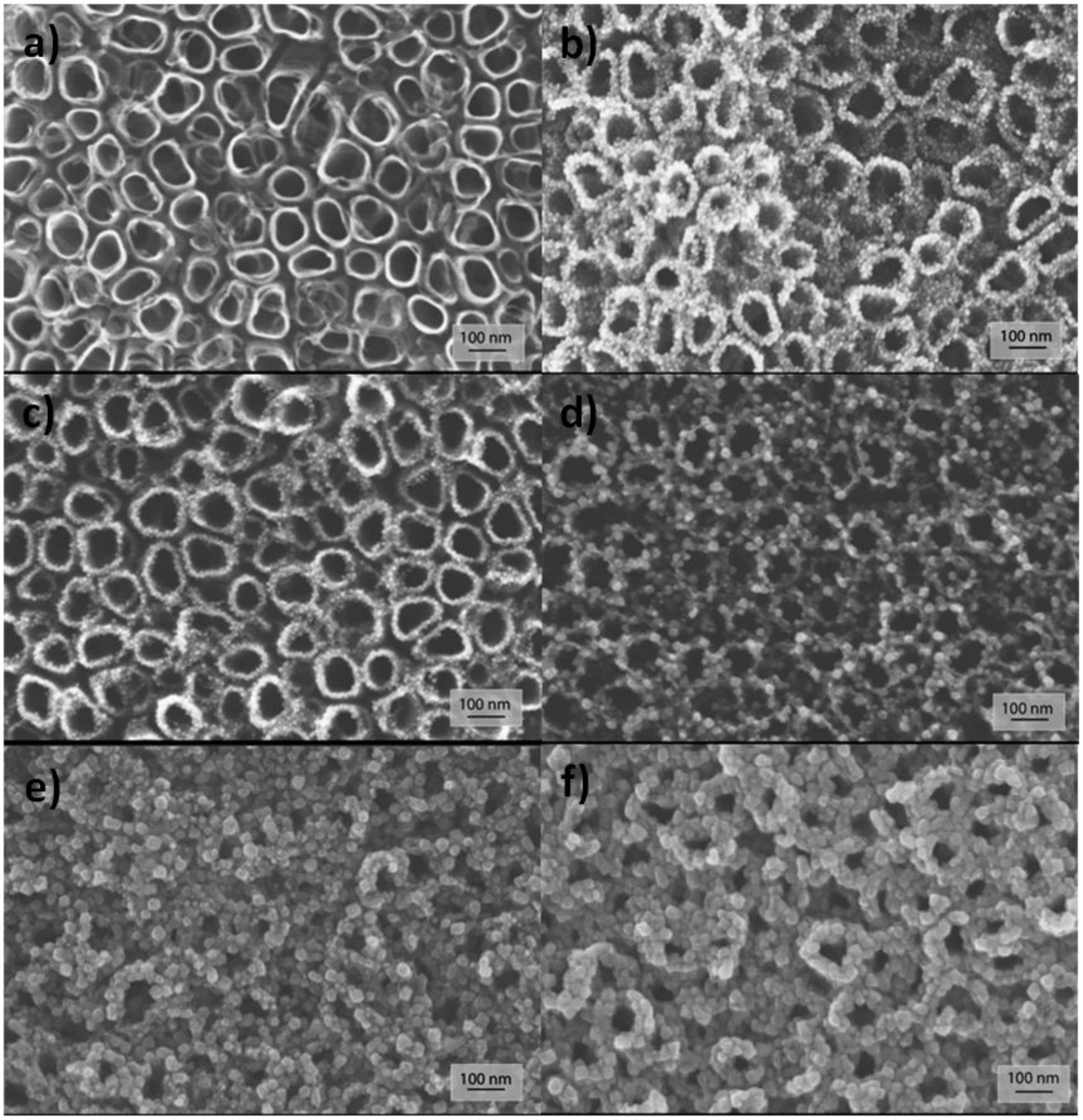

Figure 4-8: SEM of the deposition of Pd on the surface of TiO_2-nts with different number of Pd ALD cycle: a) 100 cycles, b) 400 cycles, c) 500 cycles, d) 700 cycles, e) 800 cycles and f) 900 cycles

Figure 4-9 shows a side view of a bundle of TiO_2 nanotubes on which high loading of Pd was deposited. A very uniform and complete coverage of the TiO_2 surface by Pd nanoparticles can be observe on all the length of the exterior walls of the TiO_2-nts. This complete coverage supplies a surface area available for catalytic reaction orders of magnitude higher than the geometry available from the top of the nanotubes. However, a very high Pd loading will eventually block the interstitial and inter-particle spaces causing a decrease of ECSA as predicted from the observation of **Figure 4-8**.

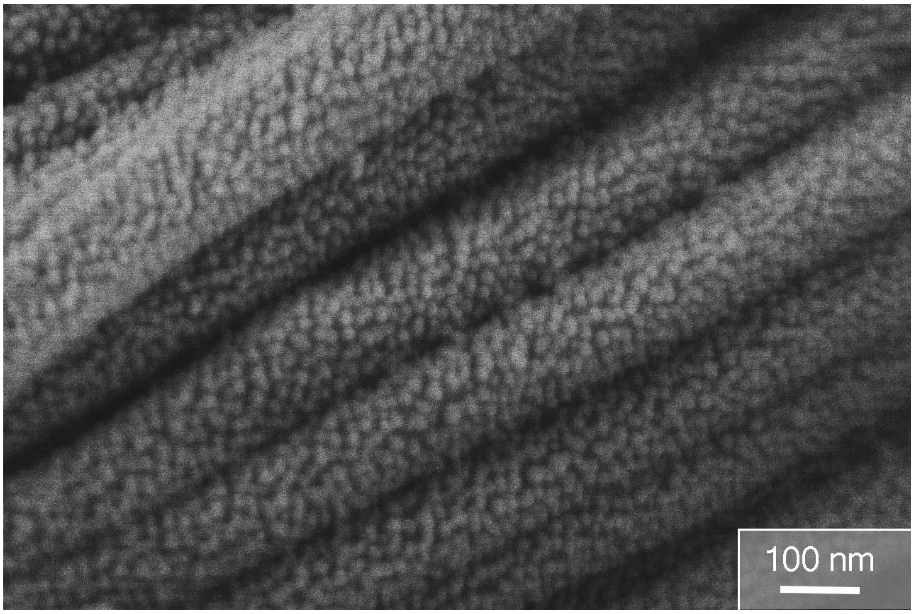

Figure 4-9: SEM picture of Pd/TiO_2 900 Pd ALD cycles deposited on the exterior of a bundle of TiO_2-nts.

As it was observed in **Figure 4-7** the annealing of the TiO_2-nts has no effect on their geometry. In **Figure 4-10** are compared a sample of TiO_2-nts as grown and a sample of TiO_2-nts annealed both with an identical deposition of 500 Pd ALD cycles. No difference can be observed on the morphology of the Pd nanoparticles deposited on their surface. The homogeneity, coverage extent and particle size of the deposited particles seem to be identical on both supports with a large coverage that continues deeper in the TiO_2-nts matrix. The expected effect of the annealing of the TiO_2-nts on the EOR over the Pd nanoparticle is an increase in catalytic activity of Pd due to an increase in electrical conductivity of the oxide caused by its crystalline structure. The higher conductivity of the support is expected to allow an easier transport of electrons through the circuit accelerating the reaction at the cathode which uses these electrons.

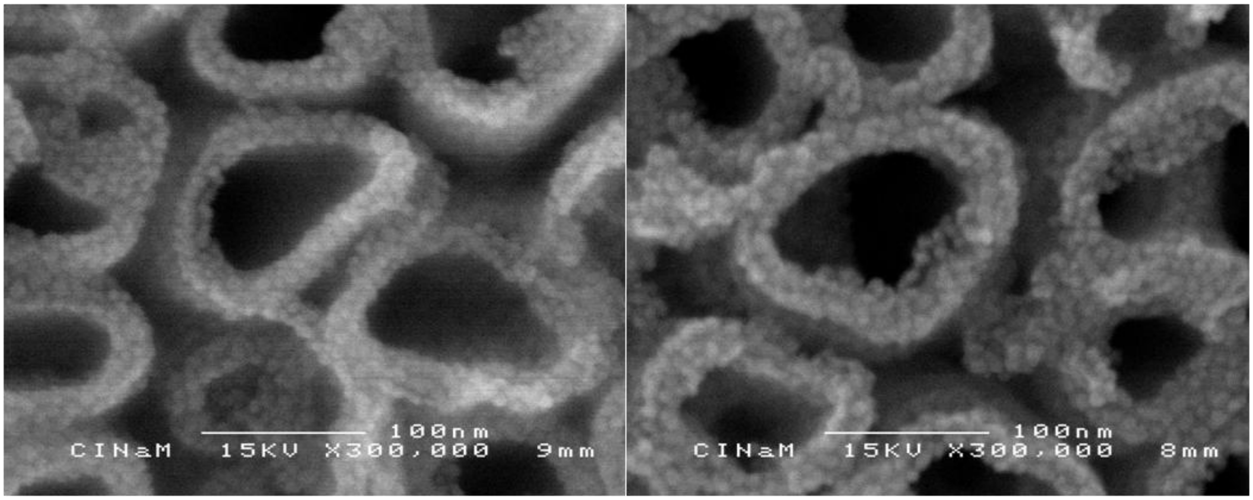

Figure 4-10: Comparison between Pd/TiO_2-nts 500 cycles on as grown TiO_2-nts (left) and on annealed TiO_2-nts (right).

By using TEM it is possible to observe the density of the samples which allows the differentiation between the oxide material (light) and the more dense metallic particles (dark). **Figure 4-11 a)** shows a TEM image of a detached Pd layer from the top of TiO_2-nts. The well defined edges of the Pd nanoparticles shows that the Pd layer is composed of a single layer of interconnecting nanoparticles that follow the geometry of the TiO_2-nts on which they are grown. **Figure 4-11 b)** shows the very bottom of the TiO_2-nts where they used to be attached to the Ti substrate. This picture shows that the deposition of the nanoparticles is made all the way to the bottom of the nanotube hence covering the entire available surface of the oxide structure. A TEM image of the side view of a single TiO_2 nanotube is represented in **Figure 4-11 c)** where a high homogeneity of the nucleation sites can be observed throughout the exterior surface of the nanotubes while the position (inside or outside) of the particles is not discernible. **Figure 4-11 d)** shows a HRTEM of a Pd nanoparticle deposited on TiO_2. It is possible to observe the (111) crystalline plane of the Pd crystal.

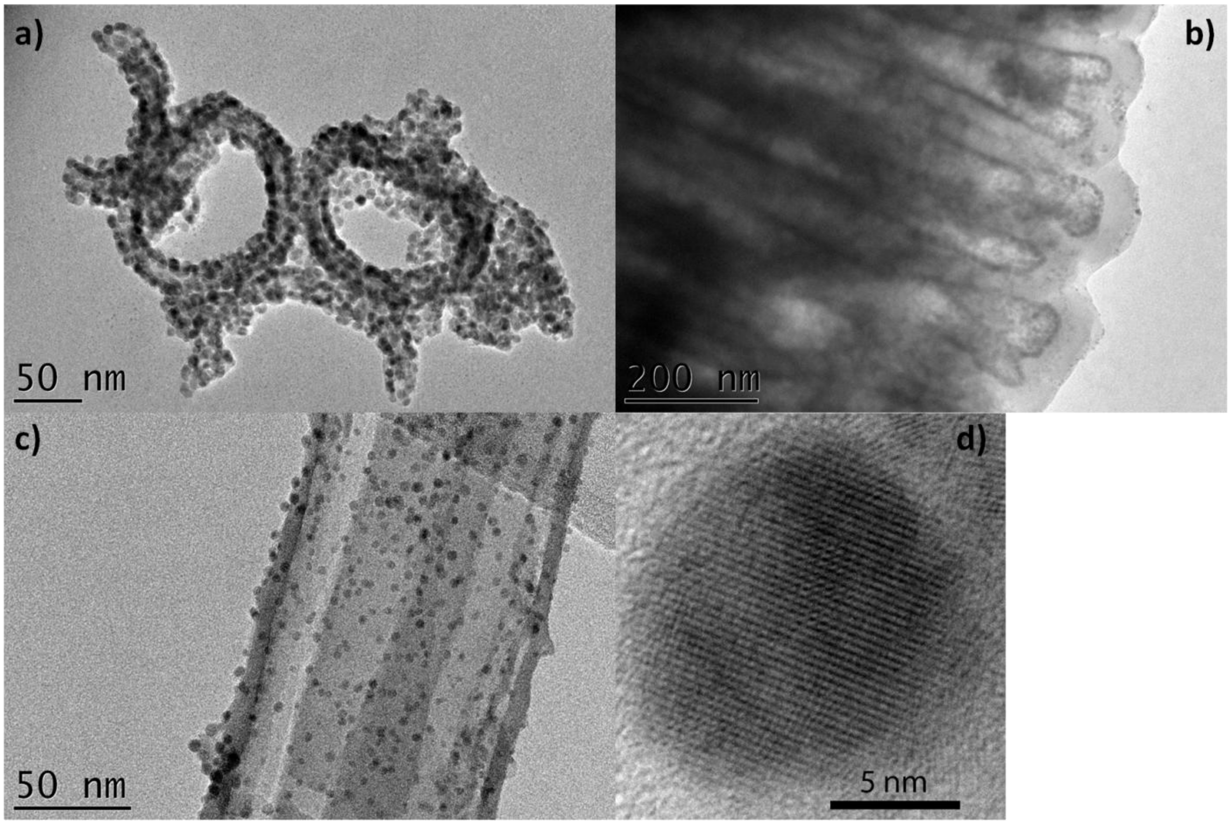

Figure 4-11: TEM pictures of Pd deposited on TiO_2-nts. A) a detached layer from the top of the nanotubes, b) see-through of the bottom of the nanotubes, c) close-up of a single nanotube and d) HRTEM of a single Pd nanoparticle

From the SEM pictures it is possible to approximate the diameter of the Pd nanoparticles. **Figure 4-12** shows the size distribution of the nanoparticles for loadings of 400 to 900 Pd ALD cycles. The average size of the nanoparticles increases with an increase in Pd loading as expected caused by further deposition of Pd atoms during each ALD cycle. The mean particle diameter and the standard deviation for each sample are shown in **Table 4-1**.

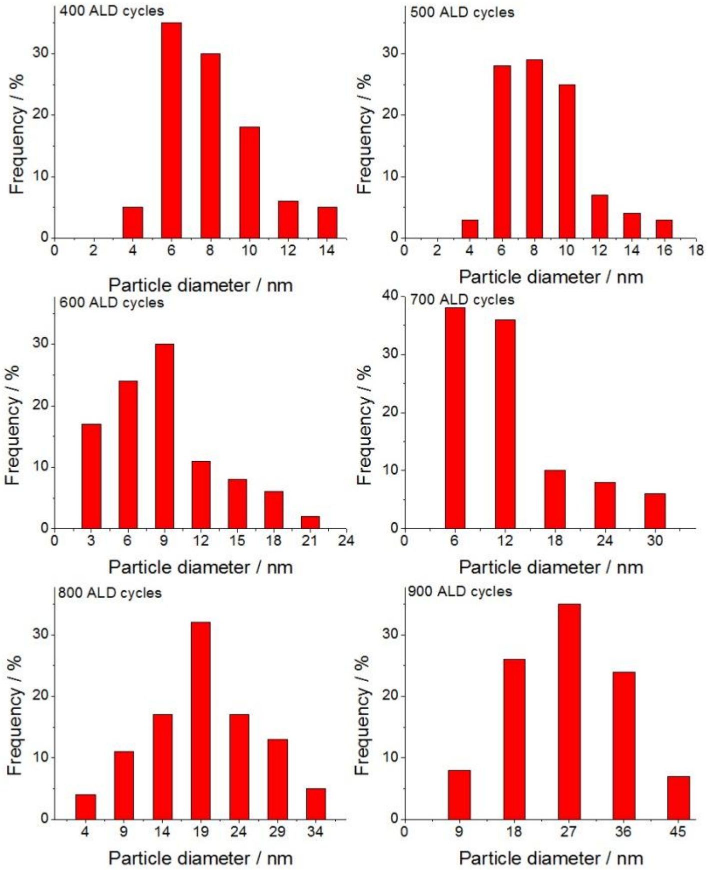

Figure 4-12: Size distribution of Pd nanoparticles for samples with 400 to 900 ALD cycles.

Table 4-1: Pd particle average diameter and standard deviation for loadings between 400 and 900 Pd ALD cycles calculated from the TEM micrographs

ALD cycles	**400**	**500**	**600**	**700**	**800**	**900**
d_{AVG} / nm	7.9	8.5	8.7	12.2	19.2	26.6
Standard deviation / nm	2.4	2.6	4.5	7.4	7.3	9.5

4.4 Electrochemical Behaviour of the Nanocatalysts

By using electrochemical techniques it was possible to further characterize the synthesized catalysts and observe how certain reactions happen at their surfaces. The potential of formation of PdO layers and their reduction along with the same phenomenon for hydrogen was studied and compared between samples deposited on as grown and annealed supports. The

ECSA was also determined for a fixed geometrical surface area using the charge observed for the reduction of PdO in acidic media in order to compare the catalytic activity of the different samples. It is also possible to observe if the EOR is facilitated by the structure, morphology and composition of the TiO_2 support by observing the overpotential needed for its oxidation.

4.4.1 Pd Behaviour in 1M KOH

Cyclic voltammetry in an electrolyte without the presence of the fuel can give diverse information on the properties of a catalyst. In **Figure 4-13** is represented the CVs in 1 M KOH of similar loadings of Pd deposited on the different TiO_2-nts supports. The CVs of the samples on the two supports have a similar general shape where different oxidation/reduction peaks can be observed at similar potentials.

By going from left to right on the anodic scan and then back to the original point on the cathodic scan it is possible to observe between -0.7 and -0.5 V the desorption of adsorbed and absorbed hydrogen on the surface of Pd (at this potential most of the desorption peak is caused by adsorbed hydrogen but lower potential would result in a larger absorption of hydrogen). Further on, centered between -0.4 and -0.3 V, are small peaks caused by surface oxidation of Pd caused by the adsorption of OH^- species from the electrolyte and further oxidation to PdO following **Eq. 3.7 to 3.9.** It can be observed that peak Pd/TiO_2-nts Ann does not have a well defined PdO onset potential and the oxidation of Pd on this sample seems to be more gradual but still as present as on the other which is confirmed by the presence of a reduction peak on the anodic scan. Further increase of current after the initial PdO formation peak is due to the formation of the PdO layer which is a function of time and potential as explained in **Section 4.2.3.2**.

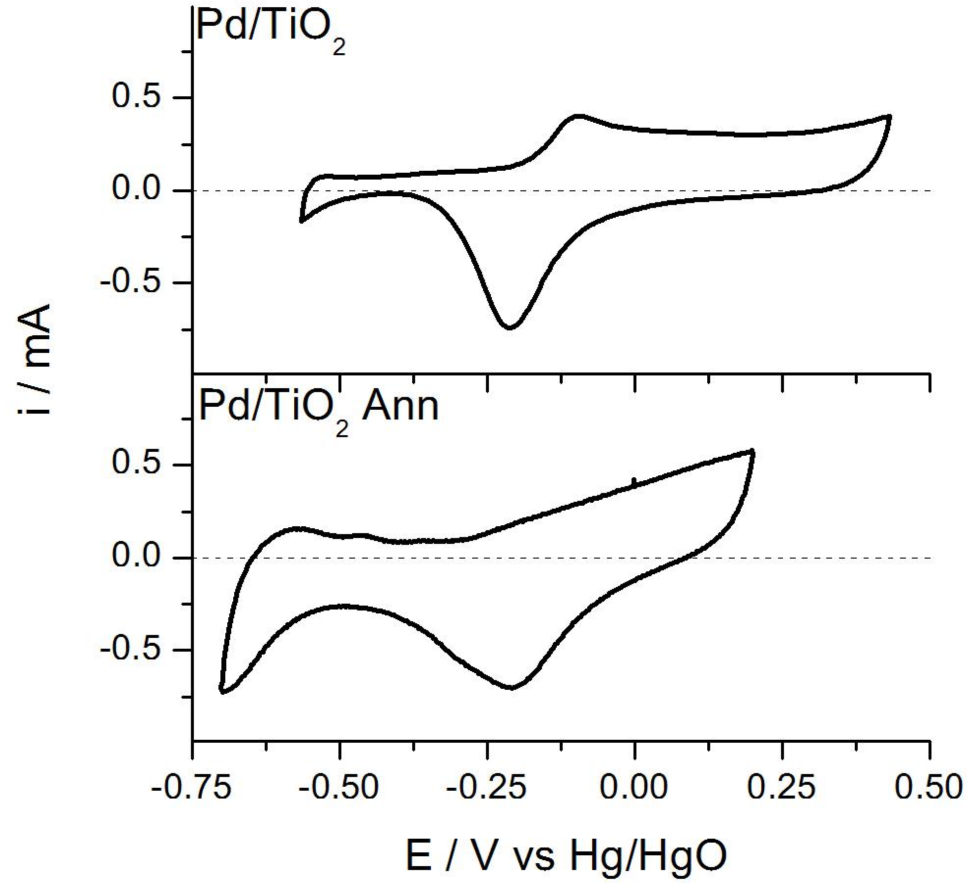

Figure 4-13: Behaviour of Pd 500 cycles in 1M KOH during cyclic voltametry.

When the scan is reversed the potential decreases rapidly due to a fast decay of the formation of the PdO layer and a change of charge in the double capacitance layer. At lower potential (between -0.2 and -0.3 V) the reduction peak of the PdO layer formed on the forward scan is observed. In theory it is possible to use this peak when a full monolayer of PdO is formed in order to obtain the ECSA of a catalyst. However it is difficult to do so in alkaline environment as explained in **Section 4.2.3.2**. The distance on the x-axis between the position of the Pd oxidation and Pd reduction peaks shows the reversibility of the reaction which is lower for a smaller distance. While the oxidation peak on the Pd/TiO$_2$-nts sample is not well defined an inflection point situated at -0.3 V marks the onset of the Pd oxidation process. It can therefore be observed that the Pd oxidation process is more reversible on the annealed sample, a phenomenon that is probably caused by an increased electrical conductivity of the support providing and removing electrons at an accelerated rate with less resistance. At potentials lower than -0.5 V, hydrogen gets adsorbed on the surface of the catalyst before migrating in the particle lattices.

4.4.2 Electrochemical surface area of Pd/TiO_2 nanotubes catalyst

CO stripping proved ineffective to find the ECSA of the different Pd/TiO_2 samples due to either a geometrical effect of the electrochemical cell preventing the contact between the CO in solution and the surface of the working electrode at the bottom or to an electronic effect preventing the adsorption of CO on the Pd surface. Consequently, another method had to be used. While a few other methods are available to find the ECSA of Pd surfaces, the reduction of a PdO monolayer is the one that is the most documented. To obtain this monolayer one has to increase to a potential high enough in the oxidation region before reverting back to negative potentials. While it is possible to operate in alkaline media, a deconvolution of the PdO reduction and hydrogen adsorption peak is necessary due to the overlap of these phenomena resulting in a loss of precision. This problem can be mitigated when operating in acidic media. The problem with this technique is that at low potential only a partial monolayer is obtained while high potential there is the possibility of the formation of the higher valence oxides (PdO_x $x>1$). Rand et al. [204], [205] have shown that the formation of a monolayer of PdO on a Pd surface is a function of time and potential [206]. This means that by holding the potential at a at increasing maximum value for a set amount of time before scanning back to the PdO reduction region it is possible to observe a trend in the charge of the PdO reduction peak. **Figure 4-14** [205]shows that the trend observed will form a plateau, positioned at different potential ranges for different holding time, corresponding to the formation of a complete monolayer of PdO. The range of potential where this plateau is observed corresponds to that stated for the formation of a full oxide monolayer on Pd by various sources [204], [205], [207]–[210].

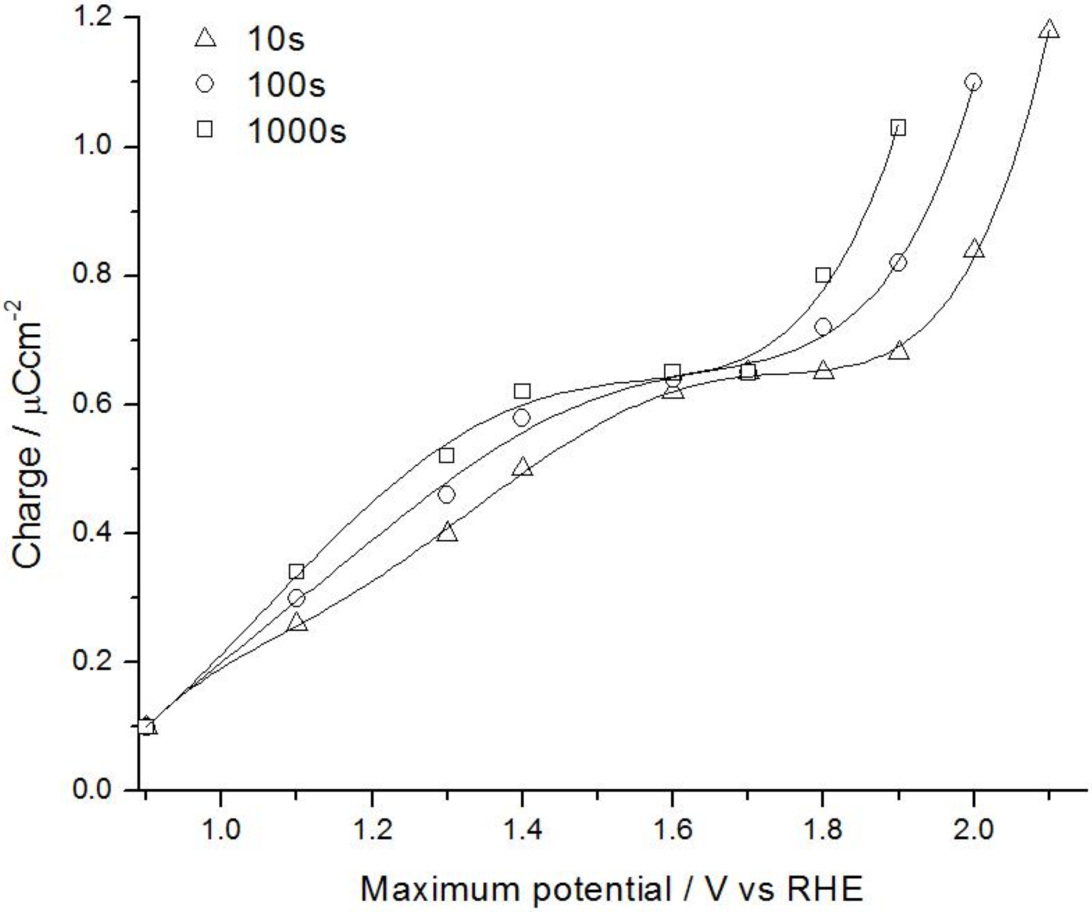

Figure 4-14: Charge of PdO reduction vs the maximum anodic potential at different holding times [205]**.**

After varying the maximum potential of the CV scans for the same sample after holding the potential at this point for 120 s the PdO reduction peak charge was calculated for each max potential using **Eq. 3.10**. Knowing that the charge necessary to remove a full monolayer of PdO is 424μ Ccm^{-2} [205]–[209], [211], [212] the surface area corresponding to a theoretical PdO monolayer could be calculated using **Eq. 3.11** and the corresponding charge density. A graph as seen in **Figure 4-15** was then produced where a plateau corresponding to the ECSA could be observed.

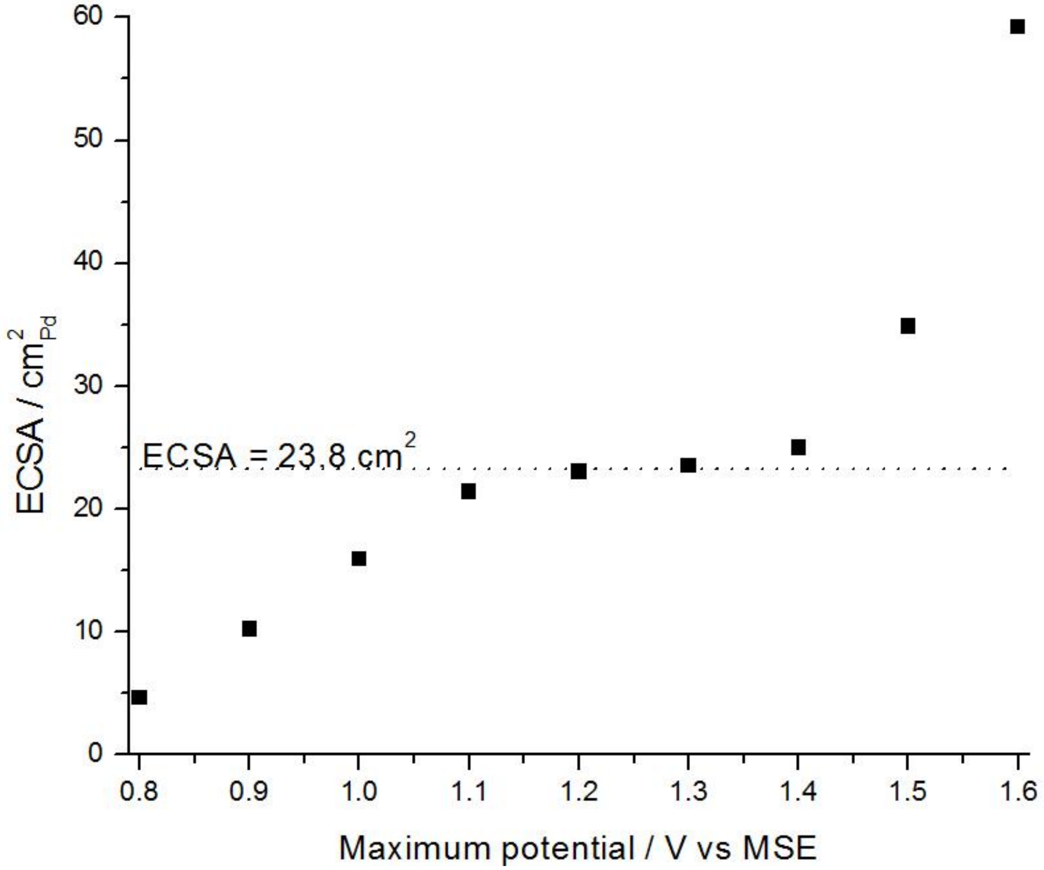

Figure 4-15: Example of a graph of PdO reduction charge vs the potential hold (Sample Pd/TiO_2 Ann 500 Pd ALD cycles)

The ECSAs obtained this way for all the active samples are displayed according to their support in **Table 4-2**. It can be seen that the ECSA calculated of the Pd/TiO_2-nts as grown and annealed samples are very similar which is in accord with the observation made from **Figure 4-10** that there is no visible difference between the morphologies of the Pd deposition on both supports. No response from the Pd particles was observed for any samples having a lower Pd loading than 500 ALD cycles for both support suggesting that the annealing of the samples does not have an effect on the activity threshold loading of Pd of the catalysts. The fast decrease in the calculated ECSA at high loading for all samples is caused by the blockage of large amounts of interstitial spaces caused by the increasing size of the Pd nanoparticles as it was observed in **Figure 4-8**.

Table 4-2: ECSA (cm^2_{Pd}) off all working samples found using PdO reduction in 1 M H_2SO_4 for a geometrical surface area of 0.126 cm^2

Pd ALD cycles	TiO_2	TiO_2 Ann
500	23.5	23.8
700	26.5	27.4
900	7.2	6.7

4.4.3 Catalysts Activities for the Ethanol Oxidation Reaction

The activities of the synthesized catalysts with different Pd loadings on the four different TiO_2-nts supports towards the EOR were studied in an aqueous solution of 1 M KOH + 1 M ethanol. Their activities are compared after being normalized using two conventional ways. Firstly, they are normalized using their ECSA in order to compare the change in catalytic activity of the Pd nanoparticles caused by the support modifications. Secondly, they were normalized by their 2D geometric surface area as this is the principal limitation in practical applications.

Figure 4-16 shows the current density observed normalized by GEO (top) and ECSA (bottom) of 500 to 900 cycles of Pd deposited on the bare nanotubes as grown (left) and annealed (right). For Pd deposited on the as grown nanotubes, normalisation by GEO shows that an increase in Pd loading increase the activity of the samples for the EOR until a maximum is reached causing the currents observed to drop suddenly to low values. This sudden drop is attributed to the diminished Pd surface area available when the Pd nanoparticles become large enough to block the interstitial spaces and even the mouths of the nanotubes leaving only a two dimensional reaction surface, which can be confirmed by the data observed in **Table 4-2**. While the differences between the intensities are not as large, the same trend can be observed when the current recorded are normalized by ECSA. This can potentially be caused by a higher conductivity of the sample with increasing Pd loading. At higher Pd loading, the coverage of the

TiO_2-nts is so high that it forms a full layer on the top of the nanoparticles reducing the amount of metal-support interface and with it the catalytic activity of the Pd surface due to a reduction in OH^- supply from the support.

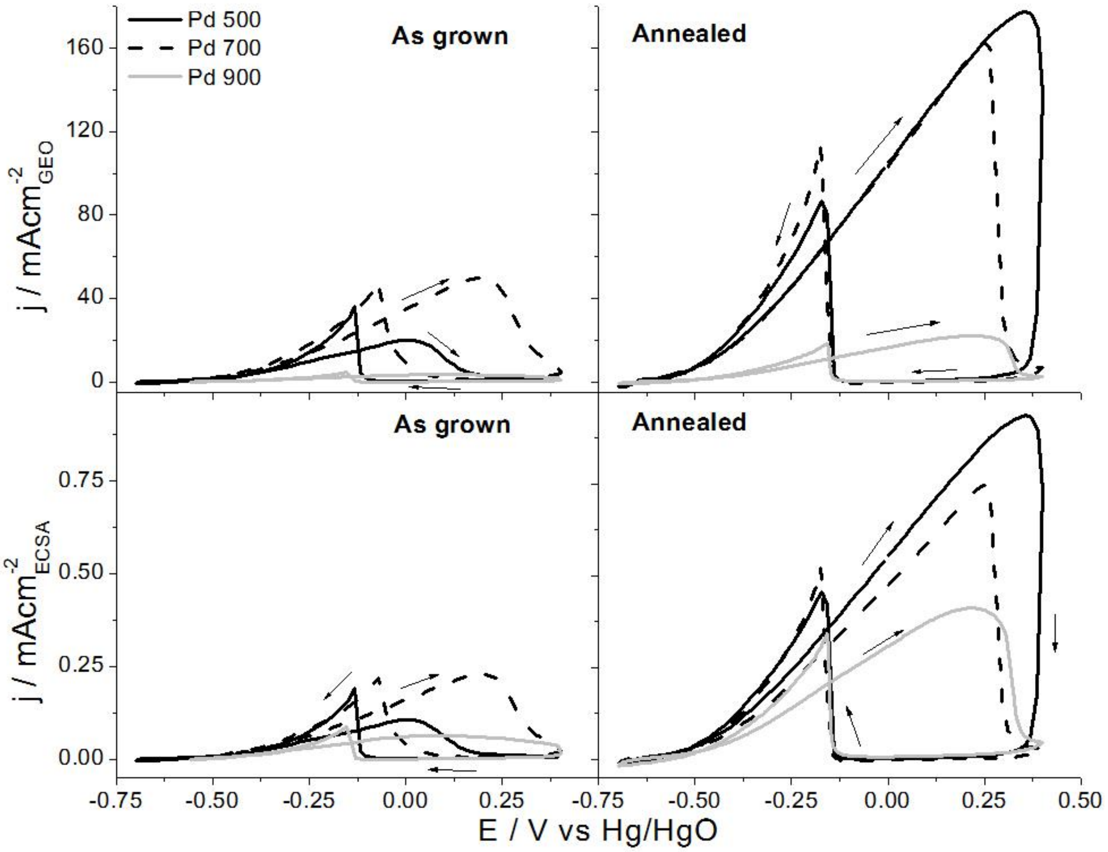

Figure 4-16: CV in 1 M ethanol + 1 M KOH of Pd/TiO_2-nts 500 to 900 Pd ALD cycled AG (left) and Annealed (right) normalized by GEO and by ECSA

For the samples deposited on the surface of annealed nanotubes it can be observed that the activity by GEO is identical for samples containing lower loadings of Pd. Once again, the activity by GEO decreases sharply at higher Pd loading caused by pore blockage. Since the samples with 500 cycles have a lower ECSA than the samples with 700 cycles as seen in **Table 4-2** it can be supposed that there is an electronic effect promoting ethanol oxidation on the Pd surface which is not present on the as grown samples. When the currents are normalized by ECSA a constant decrease in current per unit of Pd surface with an increasing Pd loading can be observed further supporting the presence of an electronic effect cause by the contact between the Pd nanoparticles and the annealed TiO_2-nts caused by the difference in work functions as proposed in **Chapter 3**. This effect would be more pronounced on annealed sample due to their higher electronic conductivity. The amplitude of this effect would decrease with increasing particle size caused by a lower influence in the Pd electron density for the same amount of charge transferred in larger nanoparticles. Overall, it can be seen that the crystallization of the TiO_2-nts has an important beneficial effect on the activity of the Pd/TiO_2-nts samples for all the range of Pd loadings studied.

4.5 Conclusions

Pd nanoparticles were grown using ALD, a highly controlled and precise deposition technique, on the surface of as grown and modified TiO_2-nts grown by anodization of a Ti foil in an aqueous environment. The TiO_2-nts were modified by annealing the nanotubes in air to increase their crystallinity and electronic conductivity. The annealing of the samples was shown to cause a sharp increase in the activities of the catalysts for the EOR which is attributed to an increased electron density in the Pd (due to the Volta potential difference) caused by an enhanced electronic conductivity of the supports. It was found that a minimal loading of 500 ALD cycles of Pd was necessary to obtain an electrocatalytic response. With careful adjustments of the electrode configuration it would be possible to maximize the activity by adjusting the nanotubes length and optimizing the Pd nanoparticles sizes. Overall, Pd/TiO_2-nts Ann is shown to be a promising catalytic system for ethanol oxidation in alkaline media.

4.6 Acknowledgements

I would like to acknowledge Dr. Lionel Santinacci and his group (Centre Interdisciplinaire de Nanoscience d'Aix-Marseille (CINaM)) who allowed us to use their

equipment and material to synthesise the catalysts presented in this chapter. Also, the TEM and SEM measurements were performed by his group.

Chapter 5 : Atomic Layer Deposition of Pd/SnO_2 Nanostructures on TiO_2 Nanotubes for Ethanol Electrooxidation in Alkaline Media

5.1 Introduction

SnO_2 has been showed to have a beneficial effect on the catalytic activity of supported Pd as discussed in **Section 2.2.2.2** and in **Chapter 3**. Therefore, it was theorized that the deposition of a thin and even SnO_2 layer on the surface of titanium dioxide nanotubes (TiO_2-nts) before the deposition of Pd nanoparticles could improve the catalytic activity of the latter due to a metal-support interaction effect. It is with this goal in mind that a thin SnO_2 layer was deposited using atomic layer deposition (ALD) on both as grown (AG) and annealed (Ann) TiO_2-nts prior to the deposition of Pd with loadings ranging between 100 and 1000 ALD cycles. These new nanocatalysts were characterized using physicochemical and electrochemical techniques in order to test their catalytic activities towards the ethanol oxidation reaction (EOR) by geometrical and real surface area.

5.2 Experimental Section

5.2.1 Nanocatalysts Synthesis

The TiO_2-nts catalyst supports were grown and annealed using the techniques described in **Section 4.2.1.1**.

5.2.1.1 Atomic Layer Deposition of SnO_2 Layer

The catalysts were synthesized by ALD in a Fiji 200 reactor from Ultratech/Cambridge Nanotech. The nanolayer of SnO_2 was deposited on the surface of the TiO_2 nanotubes using tetrakisdimethylamido tin (TDMASn) (Strem Chemicals Inc.) and hydrogen peroxide. The TDMASn canister was maintained at a temperature of 110°C and an Ar booster was used to increase the airborne concentration of TDMASn in the canister allowing a better transport of the reagent to the canister. The H_2O_2 canister was kept at ambient temperature during deposition. The tube leading from the canister to the reaction chamber was maintained at 150°C while the chamber temperature was kept at 200°C. The gas vector for the purge of the reaction chamber was Ar.

The ALD sequence was 0.25 s pulse Ar with booster in the TDMASn canister to increase the airborne concentration of TDMASn which was followed by 1 s of pulsing TDMASn in the reaction chamber where it was exposed to the substrates for 10 s and any unreacted material was pumped out of the reaction chamber for 15 s. H_2O_2 was then pulsed for 1 s in the reaction chamber and let react for 10 s before being evacuated from the reaction chamber for 15 s. The time necessary for each cycle was about 1 min. The TiO_2-nts were exposed to reagents for a total of 75 cycles for the samples on which Pd was subsequently deposited. Other samples were exposed to 50 to 150 ALD cycles and studied using an atomic force microscope (AFM) but were not used for Pd deposition. The deposition of SnO_2 has been performed on both TiO_2 nanotubes and flat Si (100) substrates in order to observe them using AFM.

5.2.2 Atomic Layer Deposition of Pd Layer

The Pd layer was deposited after the deposition of the SnO_2 layer using the procedure described in **Section 874.2.1.2.**

5.2.3 Microscopy

The morphology and shape of Pd nanoparticles were characterized using the instrument and method described in **Section 4.2.2.1**.

In parallel with the deposition of SnO_2 on the TiO_2-nts the oxide layer was also deposited on an adjacent silicon substrate (100). The deposition of SnO_2 on the silicon substrate was analysed using a non-contact AFM using a XE 100 instrument from Park Systems. This was done to observe the surface configuration of the SnO_2 nanolayer.

5.2.4 Electrochemical Characterizations

The electrochemical characterizations not described in this section were performed using the equipment, methods and parameters described in **Section 4.2.3**.

Chronoamperometry (CA) measurements were conducted in a solution of 1M KOH + 1 M ethanol. The potential was first cycled between -0.7 and 0.2 V vs Hg/HgO until a stable cyclic voltammogram (CV) was obtained. The potential was then held in the low current region at -0.55 V on the forward scan for 5 min. The applied potential was then stepped to -0.2 V, where a high current density could be observed for all samples, for 1 h in order to study the behaviour and stability of the catalysts during continuous operation

5.3 Physical Properties of Nanocatalysts

5.3.1 Atomic Layer Deposition of a thin SnO_2 Layer

The process for the deposition of SnO_2 from ALD using TDMASn and H_2O_2 is similar the deposition of Pd (described in **Section 4.3.1**) and can also be described using 4 steps as shown in **Figure 5-1**. During the first deposition cycle TDMASn will react with a hydroxyl group on the surface of the oxide where the Sn atom will attach to the oxygen of the hydroxyl group while the hydrogen leaves as an H-TDMA species resulting in the attached molecule observed in step 2. The surface is then exposed to a second precursor (hydrogen peroxide) in step 3 by which TDMASn is reduced which releases 3 more H-TDMA molecules (step 4) and leaves the Sn atom bonded to 3 oxygen atoms on the surface and a free hydroxyl group which is the reaction site for the next ALD cycle. (A more thorough description of the ALD process is described in **Section 4.2.1.2**).

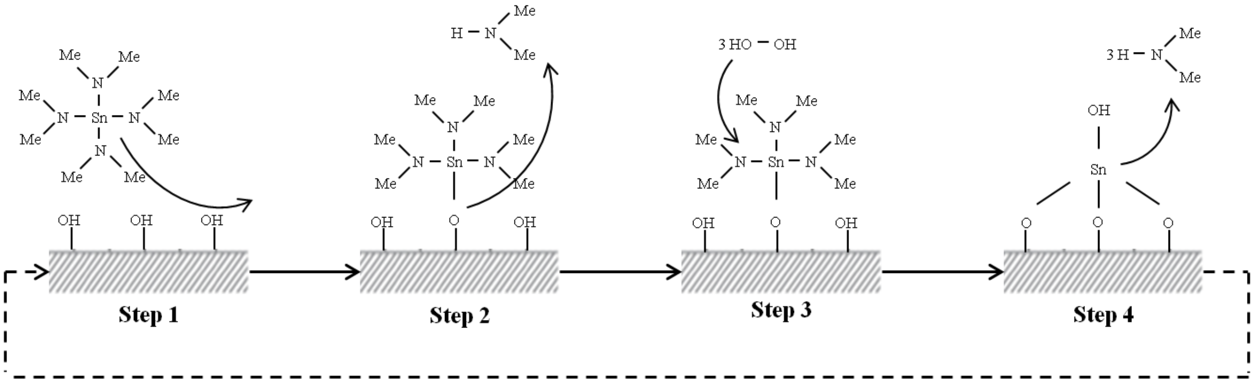

Figure 5-1: Representation of the 4 steps of ALD deposition of SnO_2 using TDMASn and hydrogen peroxide [213]**.**

5.3.2 Microscopy

5.3.2.1 SEM Measurements of SnO_2/TiO_2-nanotubes

A thin layer of SnO_2 was deposited using the previously described method on the surface of both the as grown and annealed TiO_2-nts before the deposition of Pd nanoparticles by ALD. This modification was made in the hope of increasing the electrochemical activity of the Pd nanoparticles for the EOR. Indeed, the addition of Sn or SnO_2 to a Pd catalyst has shown an increase in catalytic activity due to an electronic effect caused by a metal-support interaction [70], [72], [73].

In **Figure 5-2** we can observe the evolution of the deposition of SnO_2 on the surface of the TiO_2-nts from bare nanotubes to nanotubes covered with 100 ALD cycles of SnO_2. It can be observed that the growth of SnO_2 on the nanotubes is much faster than that of Pd and that the coverage resembles more a uniform film than the growth of nanoparticles from nucleation points as observed for the deposition of Pd. It can also be seen that a high number of deposition cycles rapidly form a thick layer of SnO_2 blocking interstitial spaces and even entire nanotubes causing a reduction in the available surface area available for subsequent Pd deposition.

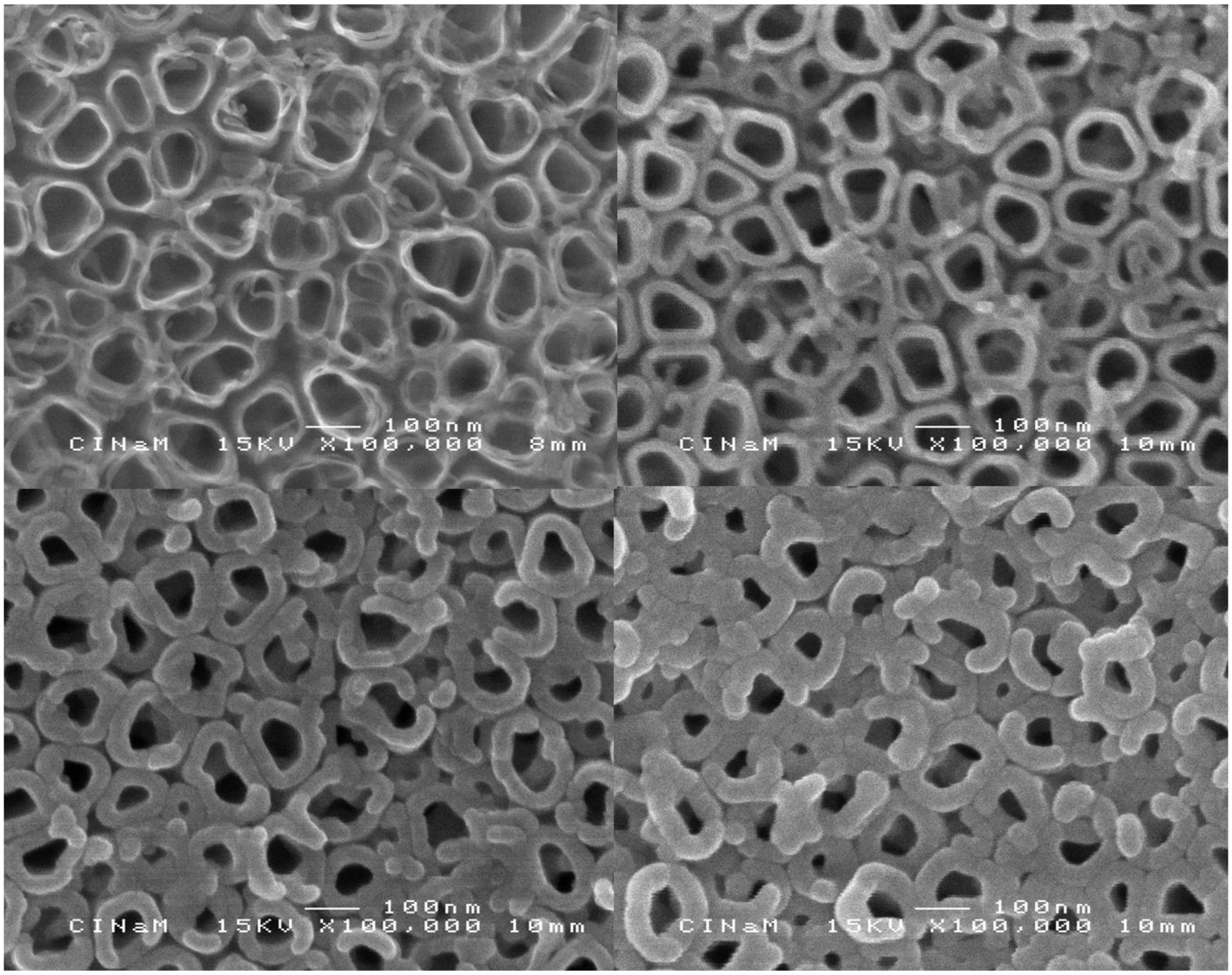

Figure 5-2: Bare TiO_2 nanotubes (top left) and 50, 75 and 100 cycles of SnO_2 deposited on TiO_2-nts (top right, bottom left and bottom right respectively).

5.3.2.2 AFM Measurements of SnO_2/TiO_2-nanotubes

The SnO_2 layer deposited on the TiO_2-nts was simultaneously deposited on the surface of a smooth Si (100) surface in order to observe its morphology. By using AFM it is possible to assess the morphology of a surface by scanning it with a probe and observing the force of atomic repulsion between the probe and the surface. This technique permits to assess the morphology of a theoretically flat surface. **Figure 5-3** represents the data obtained from an AFM instrument by scanning a region with dimensions of 3 μm X 3 μm. It can be observed that the Si substrate on which the SnO_2 was deposited has a very smooth surface while the roughness of the surface seems to increase with increasing SnO_2 loading. The roughness of the surface, corresponding to the standard deviation, of the deposited layer with an increasing thickness was obtained using the Gwyddion software and is depicted in **Figure 5-4** where it can be observed that the bare Si substrate has a very low roughness which is about 1 Å. A constant increase in roughness can be observed with an increasing deposited layer between 0 and 150 ALD cycles as can be observed by the high R^2 value obtained from a linear fitting of the data points which is equal to 0.976. Even though it increases, the magnitude of the roughness remains low compared to the size of the TiO_2 nanotubes meaning that the morphology of the SnO_2 surface will follow that of TiO_2-nts.

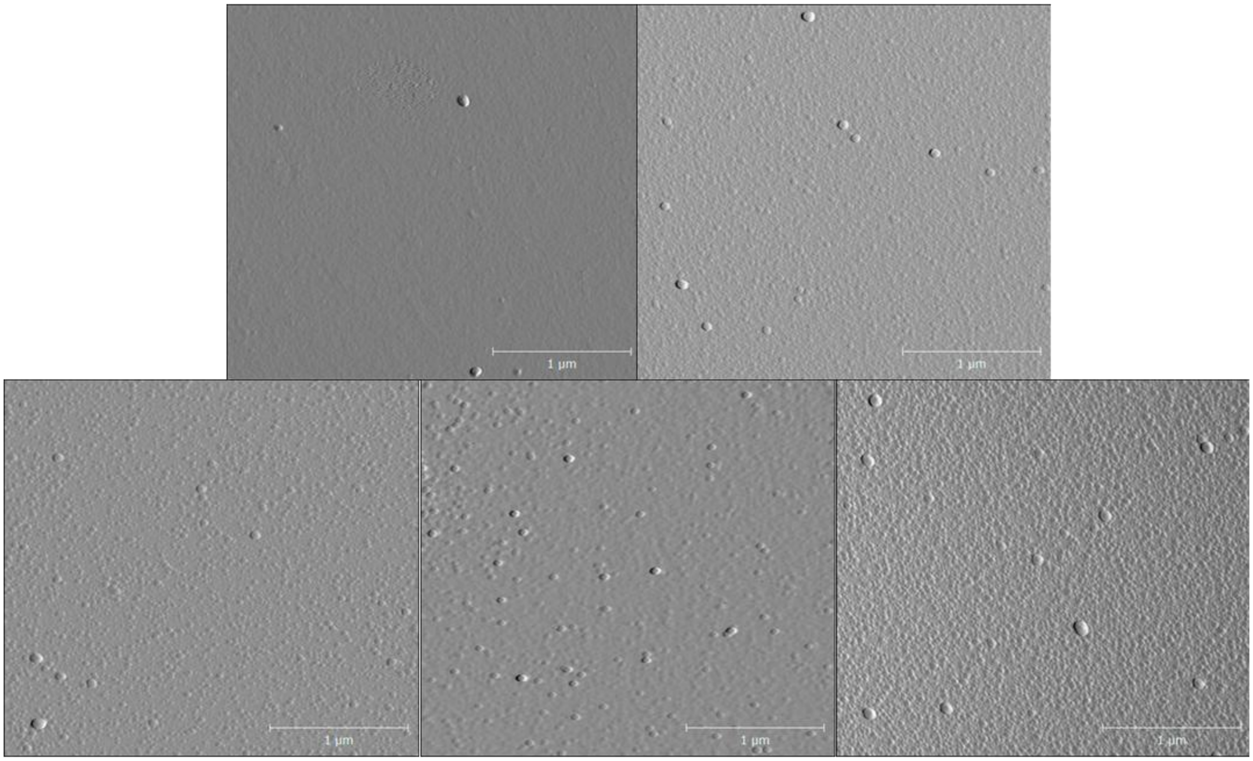

Figure 5-3: AFM images of SnO_2 deposited on the surface of a smooth Si surface. 0, 50, 75, 100 and 150 ALD cycles of SnO_2 deposition from left to right, top to bottom.

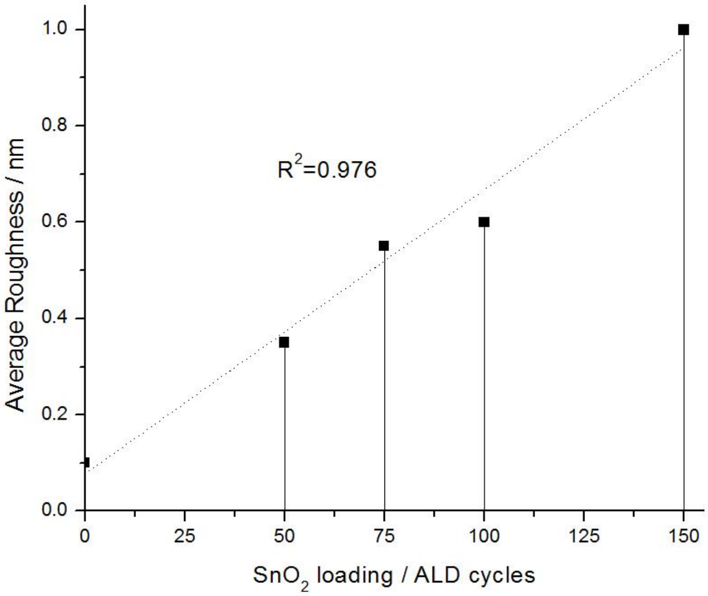

Figure 5-4: Average roughness of different loadings of SnO_2 deposited on the surface of a Si flat surface using ALD

5.4 Electrochemical Behaviour of the Nanocatalysts

By using electrochemical techniques the behaviour of the synthesized samples in solution with and without fuel was assessed. The samples containing SnO_2 both as grown and annealed TiO_2-nts were compared to that of Pd deposited on bare TiO_2-nts. The electrochemical active surface area (ECSA) was found using the charge observed for the reduction of a full monolayer of PdO and was used to normalize current in order to observe the effect of the support on the catalytic activity of the Pd nanoparticles. CA was used to observe the stability of the synthesized samples under fuel operating conditions which was compared to samples without SnO_2.

5.4.1 Pd Behaviour in 1M KOH

In **Figure 5-5** the behaviour of one of the samples for each different support type containing the same Pd loading in 1 M KOH are compared. In **Section 4.4.1** the phenomena causing the different peaks obtained on the CVs were discussed. Henceforth, in this section only the difference between the behaviours observed and their proposed reason will be discussed. It can be observed that for both samples containing SnO_2 the capacitance layer (which can be found around -0.4 V is thicker. Also, it can be seen that (as it was the case for annealed samples without SnO_2) that the potential difference between the PdO formation and reduction potentials is smaller than the as grown samples, an effect that is attributed to a higher conductivity of the TiO_2 support.

5.4.2 Electrochemical surface area of $Pd/SnO_2/TiO_2$ nanotubes catalyst

The ECSAs obtained by the reduction of a monolayer of PdO from the surface of the catalyst were calculated using the technique presented in **Section 4.4.2**. All the ECSAs obtained this way are displayed according to their support and Pd loading in

Table 5-1. While the minimum Pd loading necessary in order to observe an electrochemical response for Pd/TiO_2-nts without SnO_2 was 500 ALD cycles, activities for loadings as low as 300 and 100 cycles were observed for $Pd/SnO_2/TiO_2$-nts as grown and $Pd/SnO_2/TiO_2$-nts annealed respectively. The fast decrease in the calculated ECSA at high loading for all samples is once again caused by the blockage of large amounts of interstitial spaces caused by the increasing size of the Pd nanoparticles. The ECSA calculated for the samples with Pd supported on SnO_2/TiO_2-nts is very similar to those measured in the absence of SnO_2. However, when the Pd is deposited on the surface of SnO_2/TiO_2-nts annealed the ECSA calculated is significantly lower (45 % lower) than when Pd is deposited on the surface of the other supports. This observation suggests that there is a difference in the deposition process of a thin layer of SnO$_2$ using ALD when using an annealed support versus an as grown support. This could be explained by a faster growth of the SnO$_2$ layer on annealed samples resulting in a larger amount of interstitial space blocked for similar SnO$_2$ loadings.

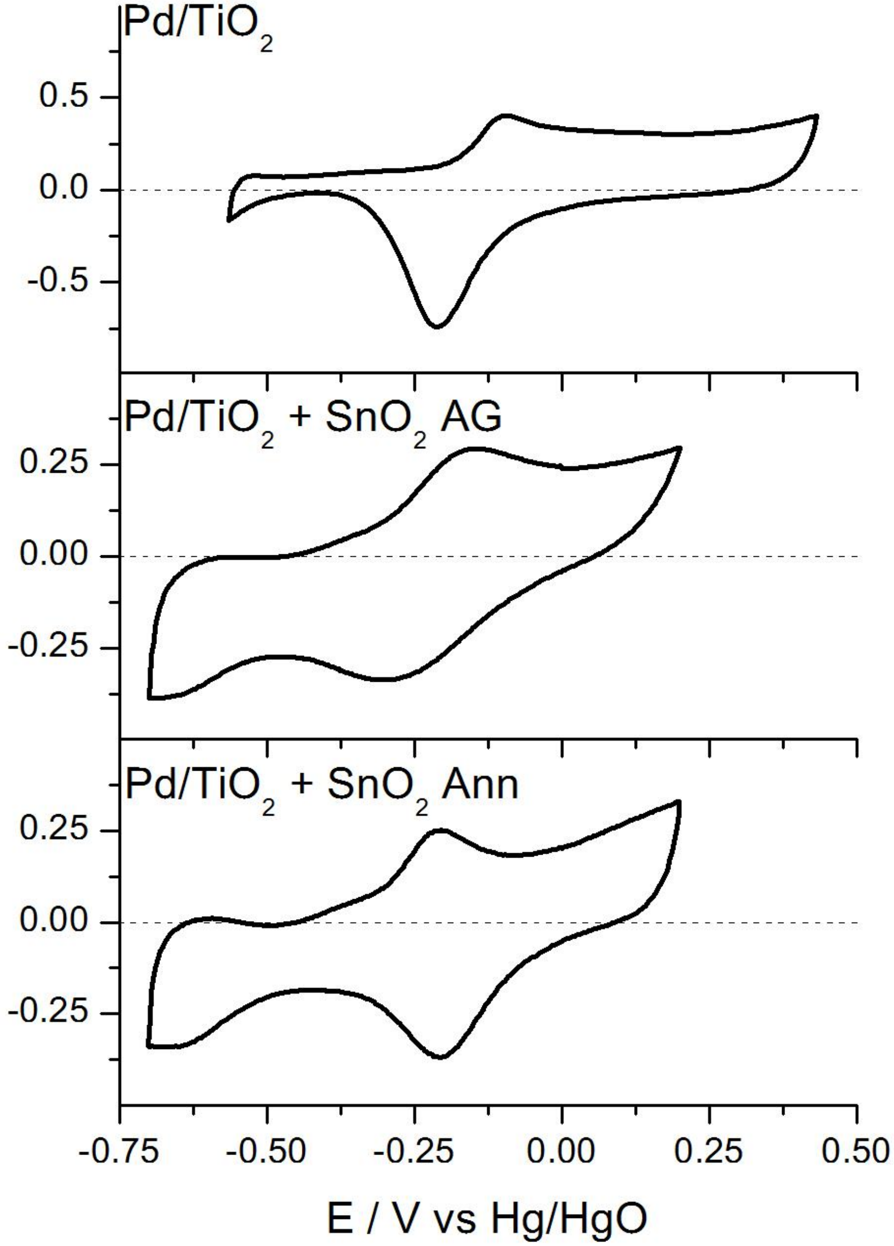

Figure 5-5: Cyclic voltammetry of Pd 500 ALD cycles in 1 M KOH , 25 mVs^{-1}

Table 5-1: ECSA (cm^2_{Pd}) off all working samples found using PdO reduction in 1 M H_2SO_4 for a geometrical surface area of 0.126 cm^2

Pd ALD cycles	Pd/SnO_2/TiO_2-nts AG	Pd/SnO_2/TiO_2-nts Ann
100	------------	2.4
200	------------	14.0
300	17.2	14.8
500	25.1	13.5
600	24.8	14.3
800	7.1	14.6
1000	5.9	0.9

5.4.3 Ethanol electrooxidation on Pd/SnO_2/TiO_2 nanotubes catalysts

Figure 5-6 compares the activity towards the EOR of samples containing 300 to 1000 ALD cycles of Pd deposited on TiO_2-nts + 75 cycles of SnO_2 as grown (left) and annealed (right). The current is normalized by geometric surface area (GEO) and ECSA. By normalising by the geometrical area of the exposed electrode the activities of the Pd deposited on the annealed samples are larger than on as grown samples for loadings below 800 cycles. The maximum current density is observed for the sample having a loading of 500 cycles of Pd for the annealed samples while it is situated at a higher loading of 600 Pd cycles for the as grown samples. It can be seen that there is a sharp decrease in activity of both types of catalysts when reaching a loading somewhere in between 600 and 800 Pd cycles. This drop in current density happens a little earlier than on the samples without SnO_2 which is expected since the amount of Pd needed to cover the pores of the nanotubes is lower due to the increase in thickness of the walls caused by the deposition of the SnO_2 layer. As on the samples without SnO_2 an increase in current density is observed on the annealed samples attributed, to an increased electronical conductivity of the TiO_2-nts.

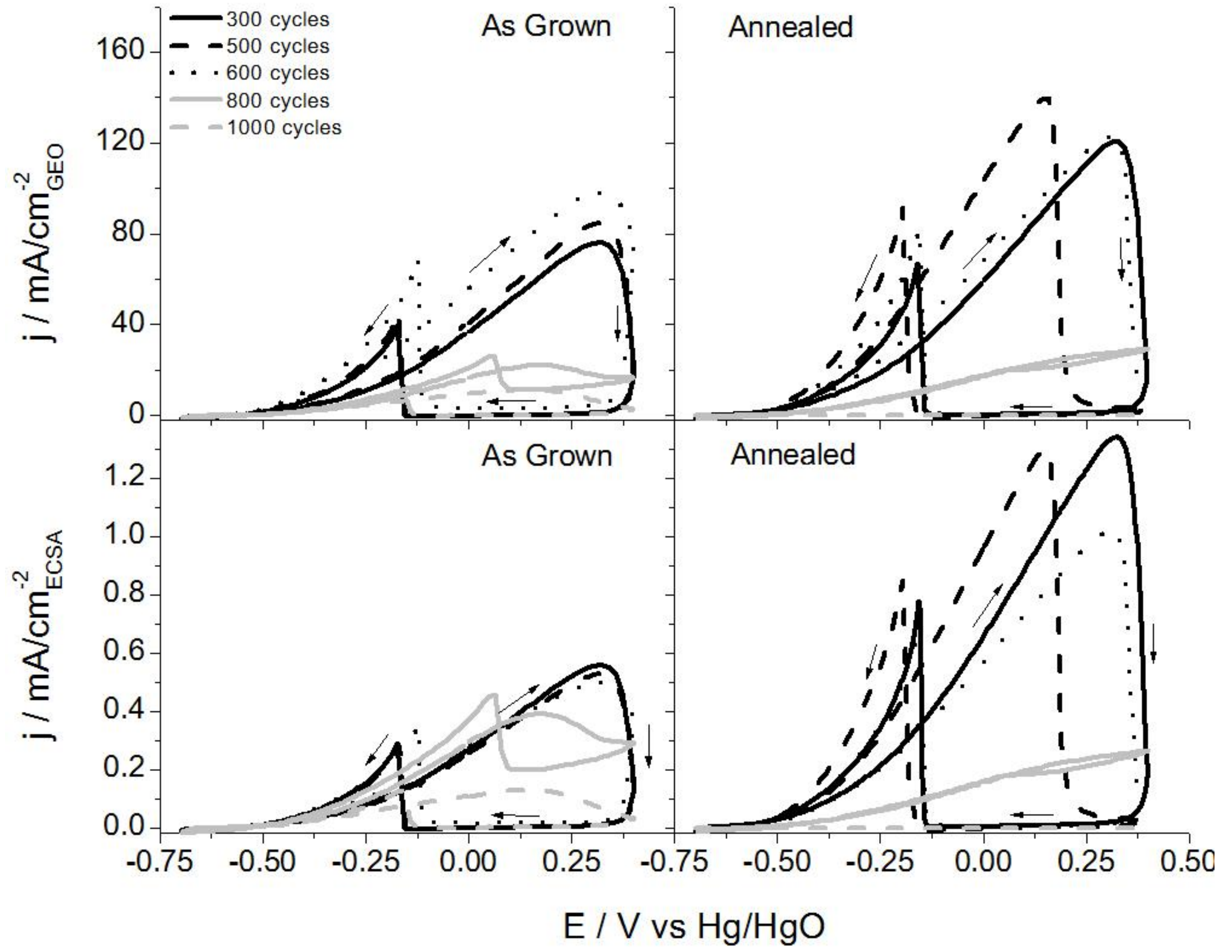

Figure 5-6: CV in 1 M ethanol + 1 M KOH of Pd/TiO_2-nts + 75 ALD cycles of SnO_2 300 to 1000 Pd ALD cycles AG (left) and Annealed (right) normalized by GEO and by ECSA

When the currents are normalized by ECSA it can be observed that for the as grown sample the activity of the catalysts stays similar until a loading over 600 cycles is reached. After this point the activity starts to decrease sharply probably due to a reduction in amount of metal-support interface. When the Pd/SnO_2/TiO_2-nts annealed samples are normalized by ECSA their activity is significantly higher than their as grown counterparts. This is attributed to an increase in electron density caused by the larger conductivity of the support. The point at which the activity starts to decrease seems to be in between 500 and 600 Pd ALD cycles which could be caused by reduced porosity caused by thicker SnO_2 layer.

Figure 5-7 compares all the samples with the same loading of Pd (500 cycles) (including those of **Chapter 4**) deposited on the as grown and modified TiO_2-nts in 1 M KOH + 1 M ethanol. The current is normalized by GEO and ECSA with a close-up on the increasing section of the forward scan which is the potential region of interest when operating in a fuel cell environment. It can be observed that no matter how the samples are normalized, Pd deposited on as grown TiO_2 nanotubes have a much lower onset potential for the EOR. The addition of SnO_2 to as grown nanotubes shows a significant increase on the activity of the Pd towards the EOR while the onset potential of the reaction does not seem to be significantly affected. This effect is probably caused by an increased number of oxygenated species provided by the support to the catalyst particles at the metal-support interface compared to bare nanotubes.

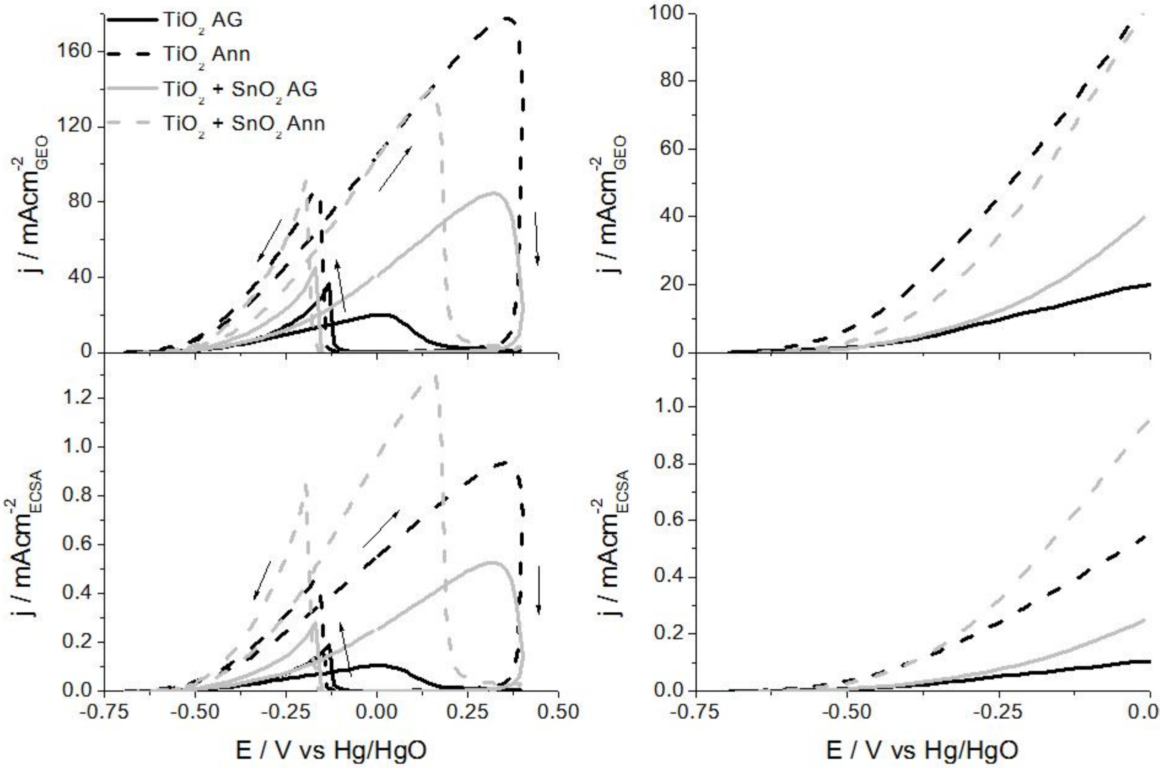

Figure 5-7: Cyclic voltammetry in 1 M ethanol + 1 M KOH of Pd/TiO_2-nts 500 cycles deposited on the different TiO_2-nts normalized by ECSA and GEO. Full cycle (left) and linear sweep valtammetry (LSV) of the increasing section of the anodic scan (rigth).

The annealing of the TiO_2-nts has shown to cause a further increase in catalytic activity. Also, the lower onset potential caused by annealing the samples is attributed to an electronic effect causing an increase in the Pd electron density due to a higher electronic conductivity of the supports. Normalising the samples on both annealed supports by ECSA shows that the rate of reaction on the surface of the sample containing SnO_2 is higher while they have a similar activity by GEO due to a lower ECSA.

In **Figure 5-8** is shown the maximal current density of all samples (including those of **Chapter 4**) tested normalized by ECSA. For the Pd/TiO_2-nts as grown and annealed samples it can be observed that the activity threshold loading is in between 400 and 500 Pd ALD. The addition of the SnO_2 layer on the TiO_2-nts shows a decrease in the Pd loading corresponding to the activity threshold which is found to be 300 ALD cycles for the as grown samples while it is even lower for the annealed samples at a mere 100 cycles. For the as grown samples the maximum current density is found just above the activity threshold while it is situated around 200 cycles for the annealed samples. The decrease in activity for loadings lower than 200 cycles for the Pd/SnO_2/TiO_2-nts samples is explained by the decrease in the activity of the catalysts for the EOR on smaller nanoparticles caused by the high amount of OH^- groups attached to the nanoparticle surface blocking adsorption sites for ethanol molecules [22].

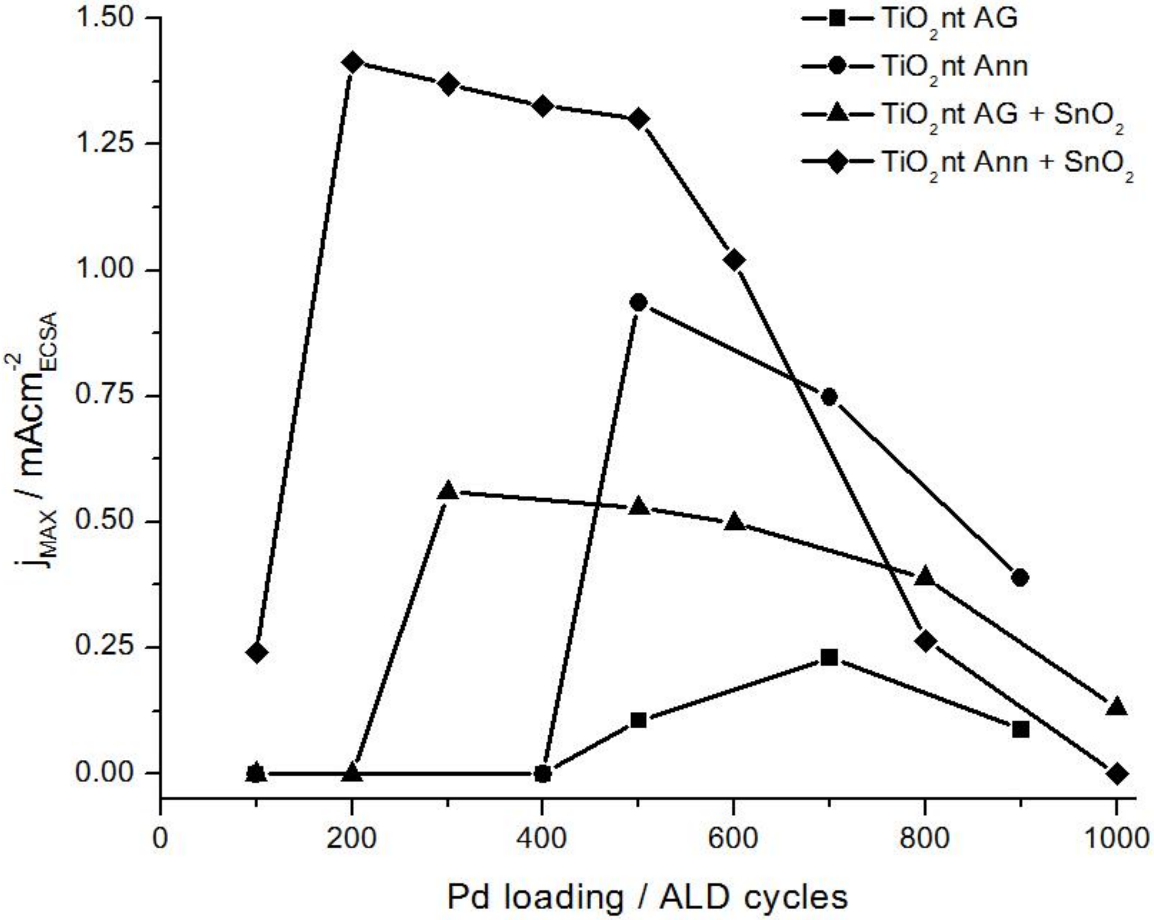

Figure 5-8: Maximum current normalized by ECSA of all different support (AG, Annealed, 75 SnO$_2$ cycles and 75 SnO$_2$ cycles + Annealed) versus number of Pd cycles.

5.4.4 Pd/TiO$_2$ Nanotubes Stability

The stability of the samples with all Pd loadings on the different supports in an ethanol containing solution was tested by chronoamperometry and the results are presented in **Figure 5-9** normalized by GEO and ECSA (data for Pd/TiO$_2$-nts as grown is not available). It can be observed that at high Pd loadings the stable current density for all supports is low due to a smaller ECSA per geometrical surface area and to a lower electronic effect with increasing particle size. Samples having lower Pd loadings had a higher stability than those with higher loadings for all types of supports. This characteristic was shown by a lower di/dt after the hour of operation.

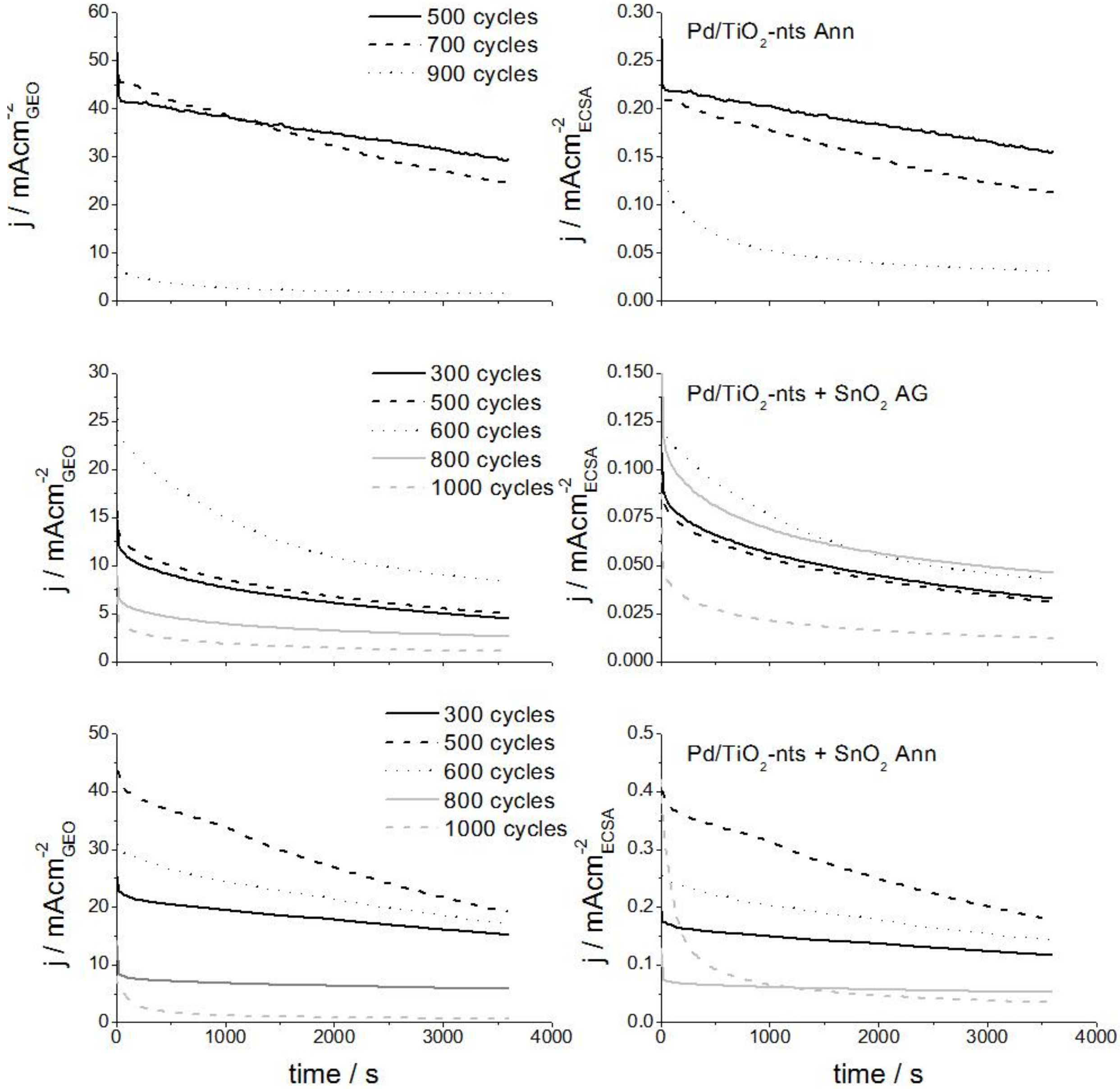

Figure 5-9: Current densities observed over 1 h of operation at a potential of -0.2 V vs MMO normalized by ECSA and GEO for all samples deposited on TiO_2-nts, SnO_2/TiO_2-nts and SnO_2/TiO_2-nts Annealed

The stabilities of samples containing the same loading of Pd on different supports are compared in **Figure 5-10** along with the steady-state current after 1 h of all the active samples (data for Pd/TiO_2 as grown is not available). It can be observed that the current density expressed by GEO for the Pd/TiO_2-nts annealed sample is higher than the others but falls below the Pd/SnO_2/TiO_2-nts annealed when normalized by ECSA due to a smaller real surface area of that electrode. It can also be observed that the stabilising current per GEO has a maximum at around 500 to 600 Pd ALD cycles after which it decreases for all samples. This current is shifted to higher loading for Pd/SnO$_2$/TiO$_2$-nts as grown when normalized by ECSA while it is unchanged for the other catalysts.

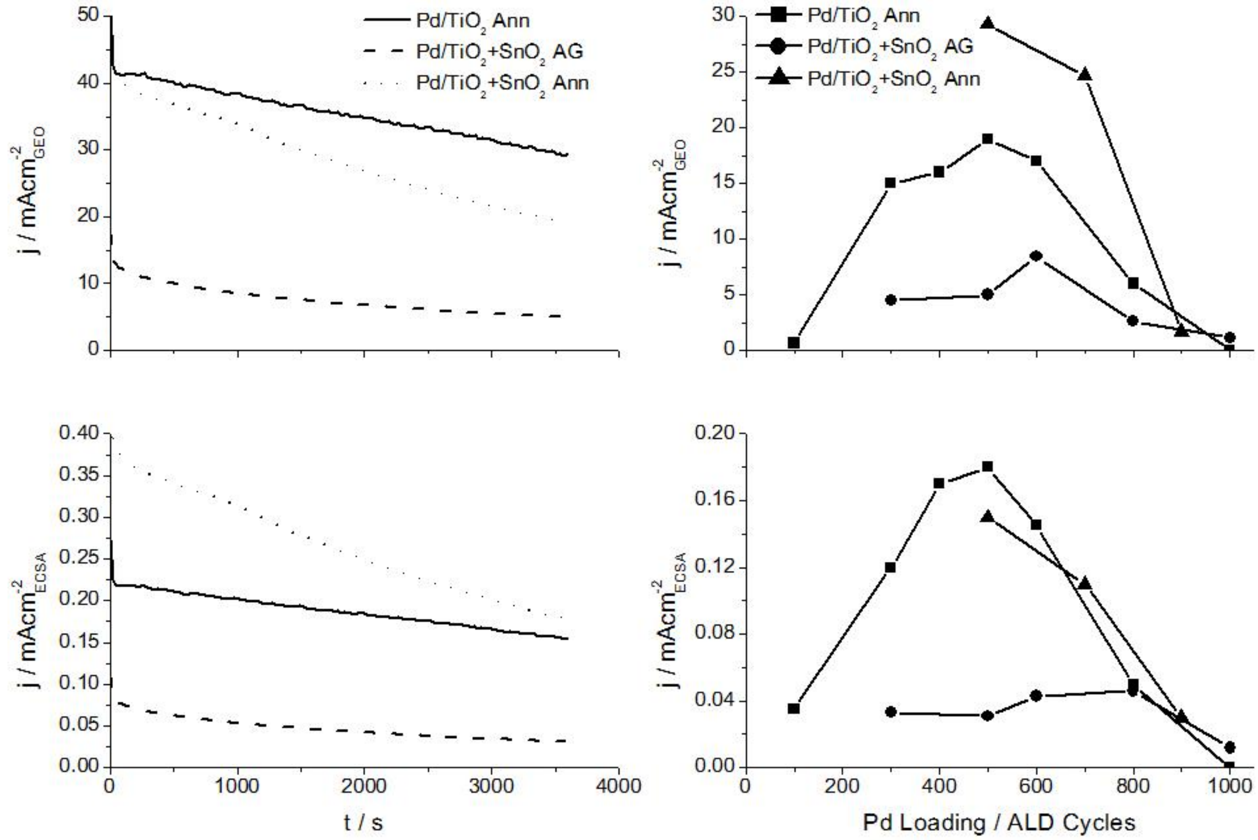

Figure 5-10: Comparison of the current density observed for the samples deposited on TiO$_2$-nts, SnO$_2$/TiO$_2$-nts and SnO$_2$/TiO$_2$-nts Annealed with a loading of 500 Pd ALD cycles at a potential of -0.2 V vs MMO for 1 h (left). Current measured after 1 h at a potential of -0.2 V vs MMO for all samples deposited on TiO$_2$-nts, SnO$_2$/TiO$_2$-nts and SnO$_2$/TiO$_2$-nts + Annealed (right)

5.5 Conclusions

In this chapter, Pd nanoparticles were grown using ALD on the surface of as grown and annealed TiO$_2$-nts covered by a thin SnO$_2$ deposited by ALD. The amounts of Pd nanoparticles deposited on the surface of the supports were varied between 100 and 1000 ALD cycles. These catalysts were tested for the EOR and their activity and stability were compared to similar samples without the SnO_2 layer (samples from **Chapter 4**). Both the addition of SnO_2 and the annealing of the TiO_2-nts before deposition have shown to increase the catalytic activity of the samples towards the EOR. The beneficial effect of the SnO_2 layer has been attributed to a supply of oxygenated species from the support to neighbouring Pd reaction sites accelerating the EOR process. The annealing of the TiO_2-nts was shown to decrease the onset potential of the EOR. A Pd loading of 500 to 600 Pd ALD cycles was shown to have the highest activity after 1 h of operation for the nanoparticles. The support showing the highest promotional effect is Pd/SnO_2/TiO_2-nts. However, its low real Pd surface area caused by a pore blocking effect of the SnO_2 layer limits the activity obtained by GEO. With careful adjustments of the electrode configuration, it would be possible to maximize the catalysts activity by adjusting the SnO_2 layer thickness and optimizing the Pd nanoparticles sizes. Overall, Pd/SnO_2/TiO_2-nts shows to be a promising catalytic system for ethanol oxidation in alkaline media

5.6 Acknowledgements

I would like to acknowledge Dr. Lionel Santinacci and his group (Centre Interdisciplinaire de Nanoscience d'Aix-Marseille (CINaM)) who allowed us to use their equipment and material to synthesise the catalysts presented in this chapter. Also, the AFM and SEM measurements were performed by his group.

Chapter 6 : Pd_xNi_{1-x} (x=1, 0.9 and 0.7) Supported on Sulphonated Graphene for Ethanol Electrooxidation in Alkaline Media

6.1 Introduction

As discussed in the **Section 2.2.1.1** various metals have been suggested to be combined with Pt and Pd catalysts in order to obtain an increased catalytic activity towards the ethanol oxidation reaction (EOR). Out of those metals, Ni is a cheap and widely available metal that has shown to have a good promotion effect on the reaction of ethanol on Pd and Pt based catalysts. On the other hand, graphene was shown to be an excellent support in the promotion of the EOR for Pd and Pt-based nanocatalysts due to its large a_s reaching 2600 m^2g^{-1}, as discussed in **Section 2.4.** Also, further improvement has been showed to be possible by surface modification of the graphene sheet providing higher particle dispersion and an increased promotion effect. In this Chapter, Pd and Pd_xNi_{1-x} (with X = 0.9 and 0.7) are deposited on sulphonated graphene (sG) and their activity towards the EOR is assessed through electrochemical techniques. Promotional effects of both the support and the presence on Ni are observed and their causes are tentatively explained. As this is a work in progress, additional physicochemical characterizations are necessary to fully understand the promotional effects.

6.2 Experimental Setup

6.2.1 Nanoparticles Synthesis

The Pd_xNi_{1-x} nanoparticles supported on sG were synthesized using the technique and reagents described in **Section 3.2.1** by using sG (synthesized by our collaborators at the Chang Gung University in Taiwan) as the support instead of a metal oxide. The addition of the Ni phase was made by the addition of a Ni salt ($Ni(NO_3)_2$*$6H_2O$ 99.9985 % (metal basis)) to the aqueous solution along with the Pd salt before reduction. The Pd nominal loading was kept at 20 wt% of the total mass of the catalyst for all Ni loading. The synthesized catalysts were Pd/C, Pd/sGraphene, $Pd_{90}Ni_{10}$/sGraphene and $Pd_{70}Ni_{30}$/sG

6.2.2 Physicochemical Characterizations

6.2.2.1 Transmission Electron Microscopy

Transmission electron microscopy (TEM) measurements were performed on a JEOL JEM-1230 instrument with an acceleration voltage of 100 kV. The catalysts powders were dispersed in alcohol and water through ultrasonication. An appropriate amount of the catalyst powder solution was dropped onto the copper grid coated with a carbon layer and air-dried for TEM measurements.

6.2.3 Electrochemical Characterizations

All electrochemical characterizations were made using the same equipment, techniques and parameters described in **Section 3.2.3**.

6.3 Physicochemical Characterizations

In order to understand the composition of the synthesized catalysts and to explain how the type of support used and the Ni concentrations affect their catalytic activity it was planned to characterize the nanocatalysts using physicochemical techniques. TEMs of the supported nanoparticles were made to observe the morphology of the catalysts. As this is a work in progress further characterizations using X-ray diffraction (XRD) and X-ray photoelectron spectroscopy (XPS) are planned in order to observe the crystal structure and the oxidation state of the different metal catalysts, respectively.

As described in the introduction (**Section 6.1**) graphene has an exceptionally large specific surface area (a_s) reaching values up to 2600 m^2g^{-1} [54], [92], [99], which offers an increased surface area for catalyst deposition. In **Figure 6-1** are represented two TEM micrograph with different magnification of a bare sG sheet. In the low magnification picture it is possible to observe the approximate size of the nanosheets measuring a few micrometers in both directions. The high transparency of the sG sheet confirms its monoatomic thickness with the darker regions being folds in its structure.

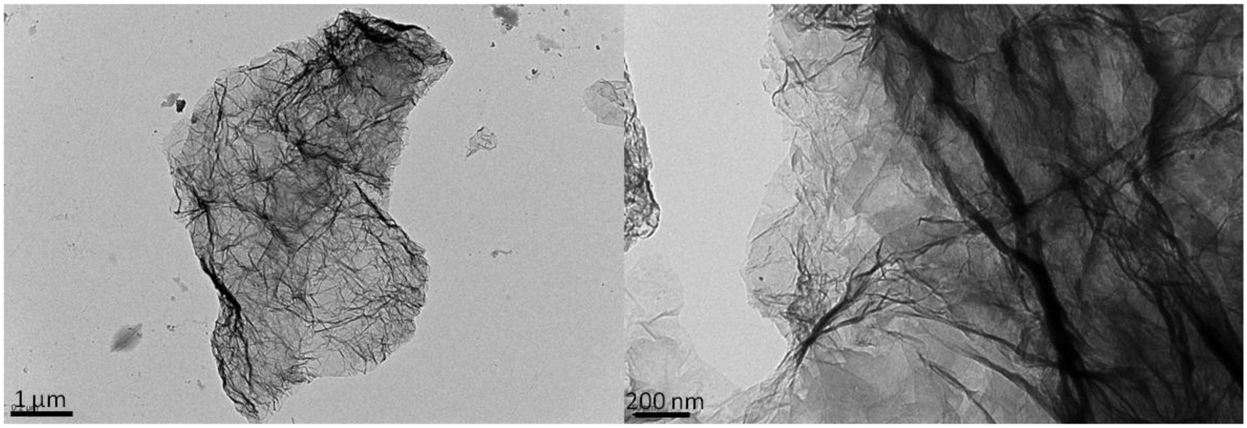

Figure 6-1: Low (left) and high (right) resolution TEM of single bare sulphonated graphene nanosheet

The TEM micrographs represented in **Figure 6-2** were made after the in-situ deposition of the Pd and PdNi nanoparticles. Starting with Pd/C it can be observed that while carbon black offers a theoretically high a_s its actual surface area is reduced by agglomeration of carbon nanoparticles blocking inter-particles space and reducing the amount of a_s available for catalyst deposition. Also, it can be seen that the Pd nanoparticles synthesized on carbon black have the tendency to form aggregates reducing the area available for ethanol oxidation and lessening the promotional effect of the support by reducing the three-phase boundary. When we look at the same Pd nanoparticles deposited on sG nanosheets it is easy to observe that the sG sheets do not have the same tendency to stick together as carbon black nanoparticles do. This property reduces the amount of a_s of the support lost by inaccessible surface area favoring an increased dispersion. As a result, it can be observe that a very low amount of Pd nanoparticles agglomeration and a homogeneous dispersion is present on the Pd/sG catalyst increasing the possible utilisation of the Pd surface. However, the addition of Ni salt during the synthesis seems to promote the agglomeration of the catalysts nanoparticles and even stray agglomerate of nanoparticles can be observed. While Ni was expected to increase the activity of the support, this high level of agglomeration will reduce the mass efficiency of the catalyst and the support promoting effect.

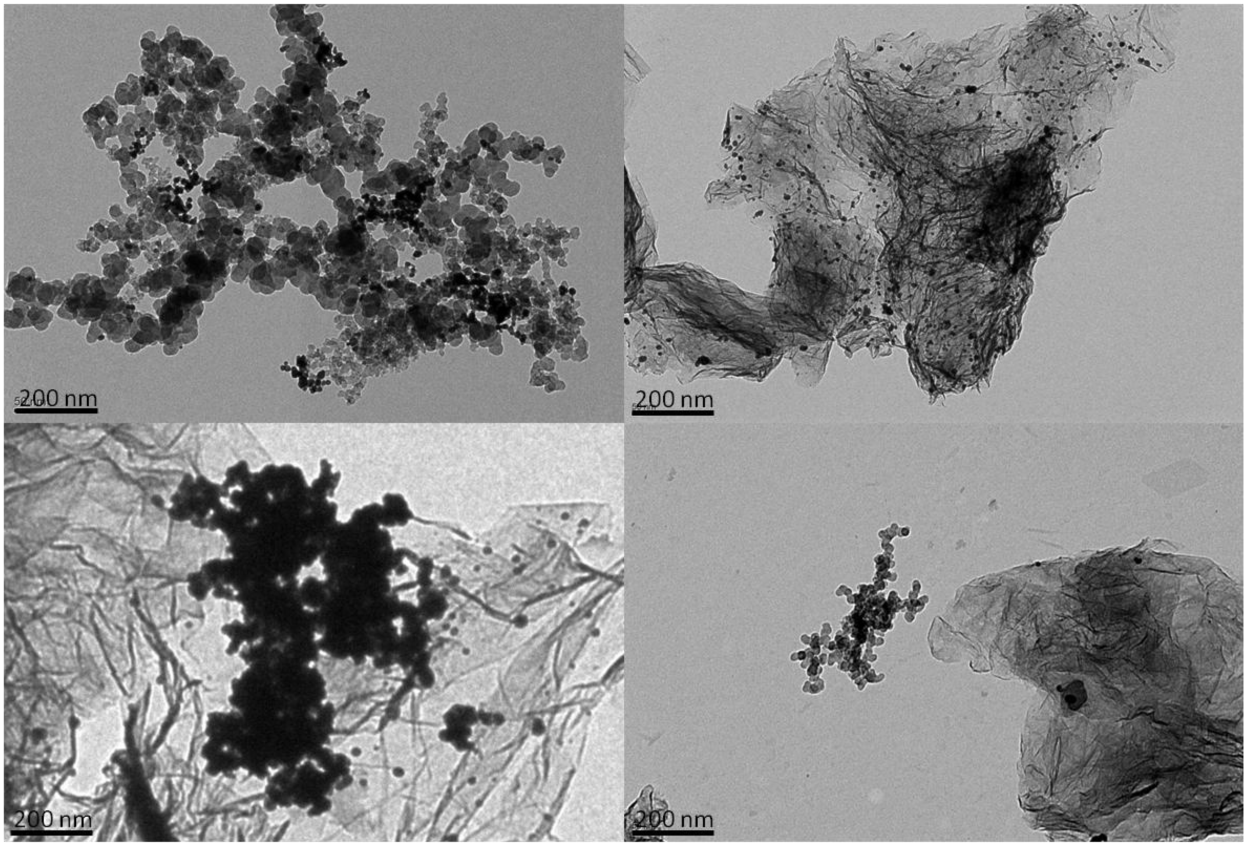

Figure 6-2: TEM of the different deposited nanoparticles: Pd/C (top left), Pd/sG (top right), $Pd_{90}Ni_{10}$/sG (bottom left) and $Pd_{70}Ni_{30}$/sG (bottom right)

6.4 Electrochemical Characterizations

By doing electrochemical characterizations, using a conventional three-electrode electrochemical cell, it was possible to assess the difference and catalytic activity and stability of the samples for ethanol electrooxidation. By normalising the obtained currents by electrochemical active surface area (ECSA) it is possible to compare the reaction rate at the surface of the metal catalysts. Usually, the physicochemical characterizations of the nanocatalysts would help to explain the difference observed in activity and stability between the samples. However, the lack of those prevents us to explain all the observed phenomena. Some speculation based on literature and TEM will be offered to explain the different behaviours.

6.4.1 Electrochemical Behaviour in 1M KOH

Cyclic voltammetry was used to observe the behaviour of the synthesized catalysts in 1 M KOH and to identify the phenomena happening on its surface. **Figure 6-3** shows the behaviour of the 4 different nanocatalysts in a 1 M KOH solution during cyclic voltammetry. The first peak that can be observed on the anodic scan is caused by hydrogen desorption from the Pd and Pd/Ni nanoparticles. The peak situated around -0.3 V is caused by the adsorption of OH^- groups on Pd. This peak seems to be mitigated by the addition of Ni maybe due to a more gradual adsorption spanned on a larger potential range. Further on, the gradual formation of PdO layer can be observed until the scan is reversed. The main peak on the cathodic scan is caused by the reduction of the previously formed PdO layer on the Pd surface. Eventually, the decrease in potential leads to the adsorption and absorption of hydrogen.

A few phenomena caused by the type of support used and the composition of the catalyst can be observed in **Figure 6-3**. First, it can be observed that while going from Pd/C to Pd/sG does not affect significantly the shape of the CV while the addition of Ni causes an increase in the ohmic resistance which is represented by a more pronounced inclination of the CV with increasing NiO content [214]. This effect may be caused by an increased electronic resistance of the catalyst caused by the possible formation of a NiO_x phase (this could be confirmed by XPS measurements in the Ni region). Another phenomenon than can be observed is the lower current response of Pd on sG than on carbon black which goes against the observations made from TEMs showing an increased dispersion on sG compared to carbon black. While this can be explained in part by a difference in particle size, which could be assessed by XRD and confirmed by higher resolution TEM images, another experimental effect is present. Indeed, the low density of sG compared to carbon black made the dissolution of the catalyst in the same liquid volume harder.

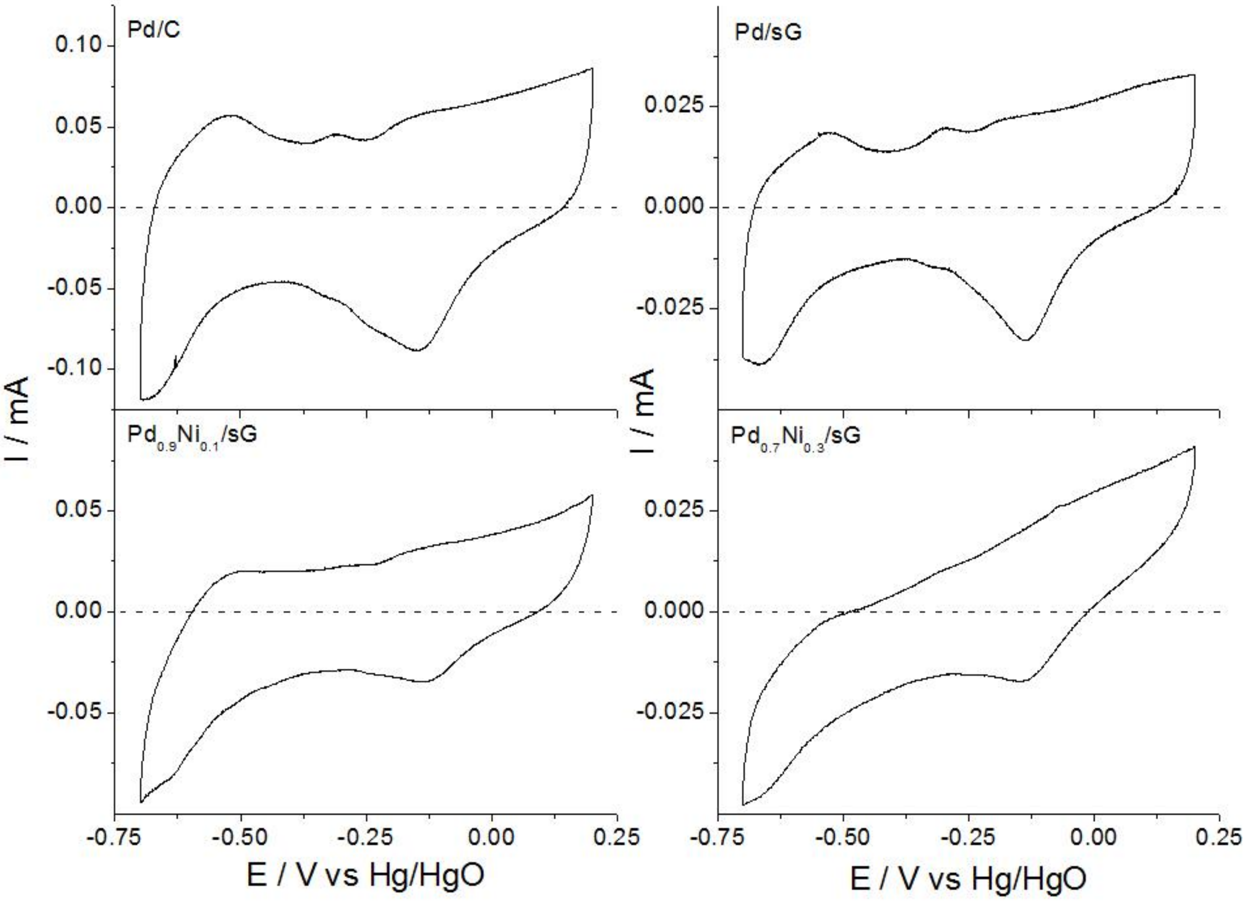

Figure 6-3: CV in 1 M KOH of all samples at a scan rate of 25 mVs^{-1}

6.4.2 CO Stripping

In order to obtain the ECSA the catalysts surfaces were saturated with CO which was then stripped from the surface by increasing the potential applied between the working and counter electrode. The CO stripping peak observed is integrated using **Eq. 3.10** which gives the charge necessary for the removal of the adsorbed CO. Using **Eq. 3.11** the ECSA is found assuming that the Pd surface is saturated with a full monolayer of CO. By finding the real surface area of the electrodes it is possible to normalize the current obtained for the ethanol electrooxidation allowing us to compare the activity of the different catalysts. **Figure 6-4** shows the CO stripping curve of the four different samples where the highlighted zone is the integrated peak used to determine the ECSA. The difference between the first and second cycle that is not attributed to CO desorption is caused by the charging of the double capacitance layer due to the potential hold at lower potential. Complete dissolution of the catalyst may not have been obtained and agglomeration of particles at the glass interface was observed. For these reasons the amount of catalyst deposited on the working electrode was lower for sG supported particles. That is the reason why the ECSA obtained from the different catalysts are not compared in this section.

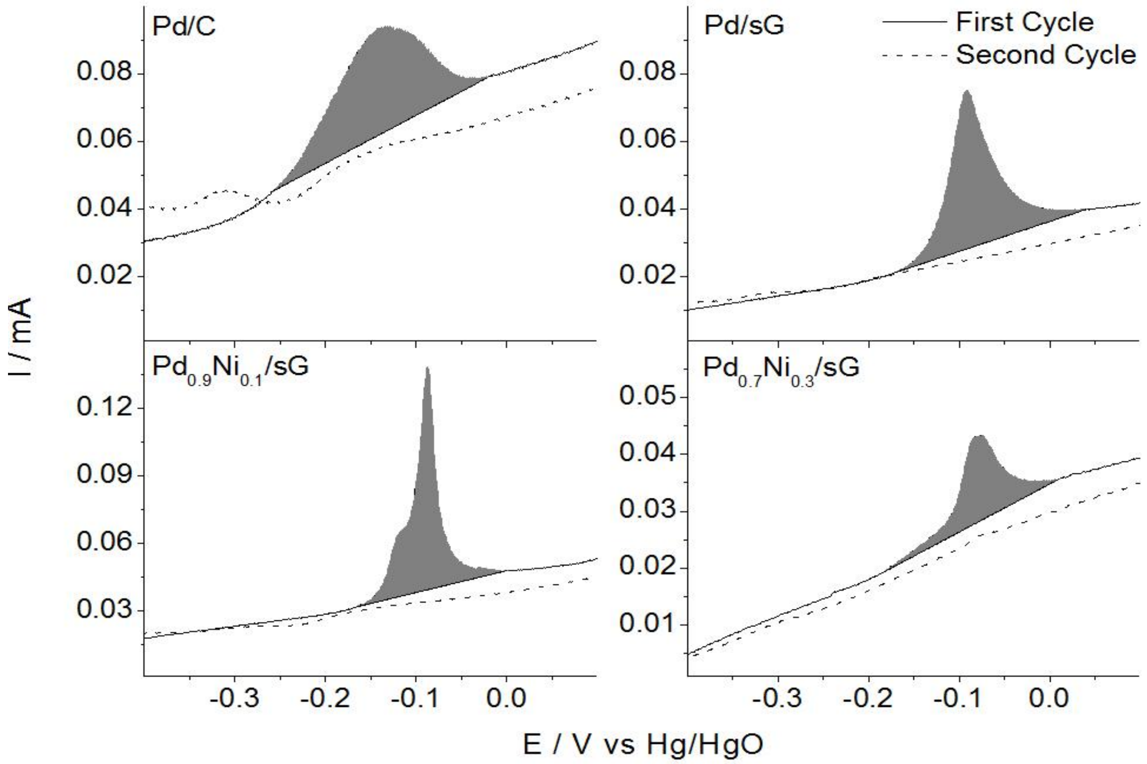

Figure 6-4: CO Stripping for all samples showing first and second cycle and integrated area

6.4.3 Electrooxidation of Ethanol on PdxNi1-x (x=1, 0.9 and 0.7)

The normalisation of the ethanol oxidation currents on the synthesized nanocatalysts by ECSA found using CO stripping allows us to compare the activity of the Pd surface of the different catalysts towards the EOR. **Figure 6-5** shows the current densities of the different nanocatalysts in a solution of 1 M KOH + 1 M ethanol normalized by ECSA during cyclic voltammetry. The peak on the anodic scan represents the increasing number of ethanol molecule partially oxidized with increasing potential until the PdO layer formation region is reach where the current density observed starts to decrease sharply. On the reverse scan, no current is observed until the PdO reduction region after which the peak observed is caused by the oxidation of strongly adsorbed molecules on the forward scan. In theory the ratio of the intensity of the peak of the forward scan to that of the reverse scan can give a gross comparison of the amount of carbonaceous species present on the surface of the forward scan (electrode poisoning) [188]. The I_f/I_b of the different catalysts were found to be 0.52, 0.83, 0.76 and 0.72 for Pd/C, Pd/sG, $Pd_{0.9}Ni_{0.1}$/sG and $Pd_{0.7}Ni_{0.3}$/sG respectively. This suggest that going from carbon black to sG as a support reduces the amount of poisoning on the surface of the catalysts probably due to an increased amount of hydroxyl groups present to oxidize the adsorbed molecules. An increase in poisoning can be observed with increasing Ni content which is thought to be caused by a decrease in the amount of metal-support interface compared to Pd/sG caused by the agglomeration of the nanoparticles.

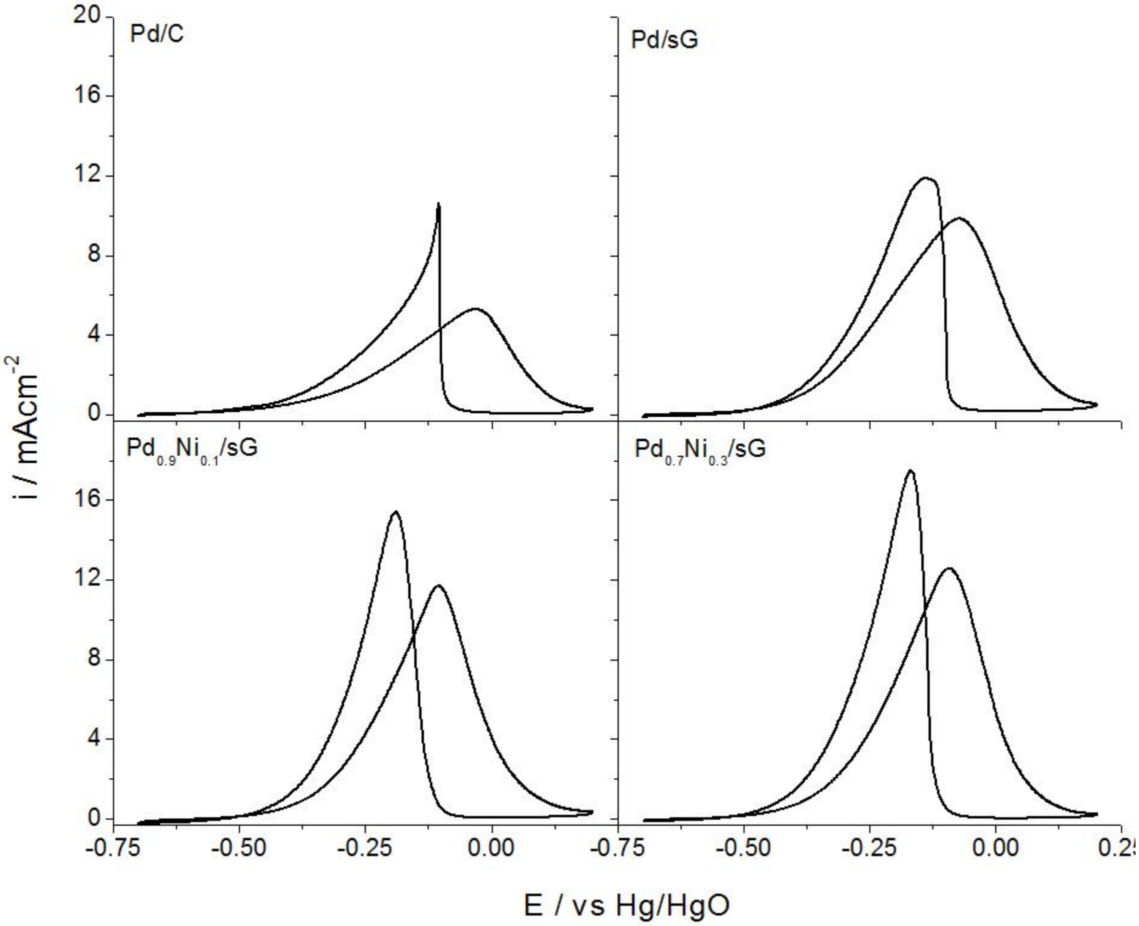

Figure 6-5: CV in 1 M KOH + 1 M ethanol normalized by ECSA, found using CO stripping, of all samples at a scan rate of 25 mVs^{-1}

By comparing the increasing portion of the anodic scan obtained during CV scans in the presence of ethanol of the different catalysts, it is possible to assess their relative activity. For this reason this region is plotted for all the catalysts in **Figure 6-6** where it is possible to observe that the catalysts deposited on the sG performed significantly better in all cases than the Pd/C. The onset potential of all the catalyst is very similar suggesting that the promoting effect is not caused by an adsorption of hydroxyl groups at lower potential as suggested in **Chapter 3 and Chapter 5**. Also, both catalysts containing Ni had the same current densities for the potential range of interest. It can be seen that while the current density for all catalysts deposited on sG was the same at potential below -0.2V the Ni containing catalyst had a higher current density at higher potential than the Ni-less catalyst. This can be explained by a bi-functional mechanism where at higher potential different molecules are preferentially attracted to Ni and others to Pd. These attached molecules on Ni and on Pd can react together if they are on neighbouring sites at the PdNi interface. Literature suggests [46], [47], [49] that the molecule preferentially adsorbed on Ni or NiO are hydroxyl groups that can help oxidize carbonaceous species adsorbed on Pd surfaces.

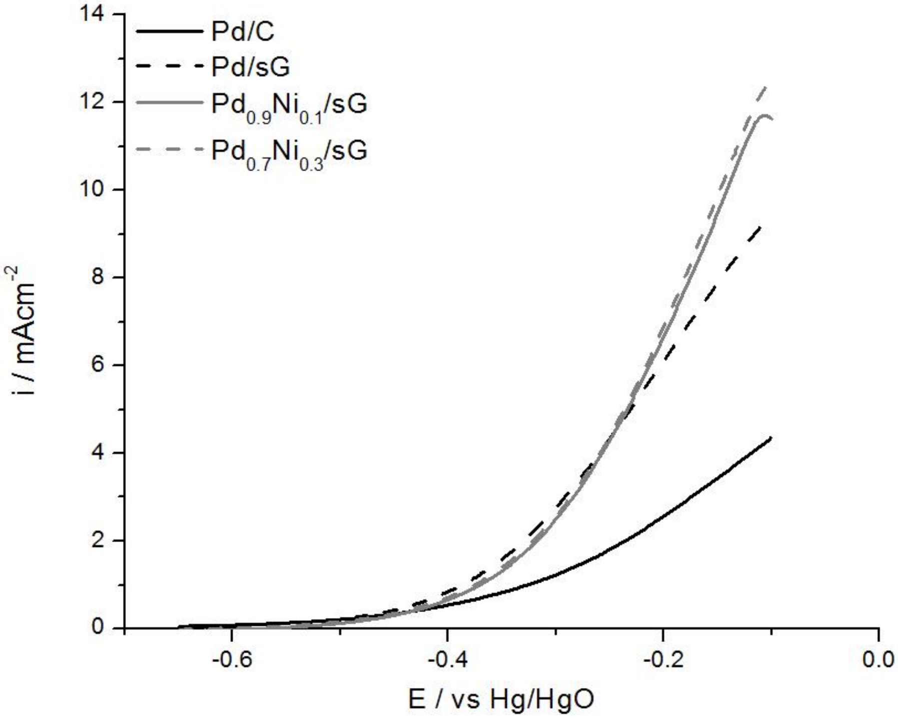

Figure 6-6: LSV of the increasing part of the anodic scan in 1 M KOH + 1 M ethanol normalized by ECSA of all samples at a scan rate of 25 mVs^{-1}

6.4.4 Chronoamperometry

By applying a potential in the range showed in **Figure 6-6** for an extended period of time it is possible to observe the change in power density over time which can be related to the phenomena happening at the catalyst surface. In **Figure 6-7** a potential of -0.2 V was applied for 1 h and the current densities obtained are plotted vs time. The current densities obtained at time 0 are close to those obtained for the same potential on the CV scan which correspond to the activity of a bare catalyst surface. The initial fast decrease is caused by the poisoning of reaction sites on the Pd surfaces by strongly adsorbed molecules such as ethoxy molecules and CO_{ads} [24]. It can be observed that Pd/C has a current density of about half that of Pd/sG for the whole time span suggesting that the reaction rate of the limiting step is about twice as high on the surface of Pd/sG. For samples containing Ni the current density can be seen to decrease at a faster pace than Pd/sG and eventually reaching that of Pd/C. This low stable current is suggested to be caused by the instability of the catalytic system due to the large amounts of agglomeration observed in the TEMs which are less strongly adsorbed to the supports surface than individual nanoparticles.

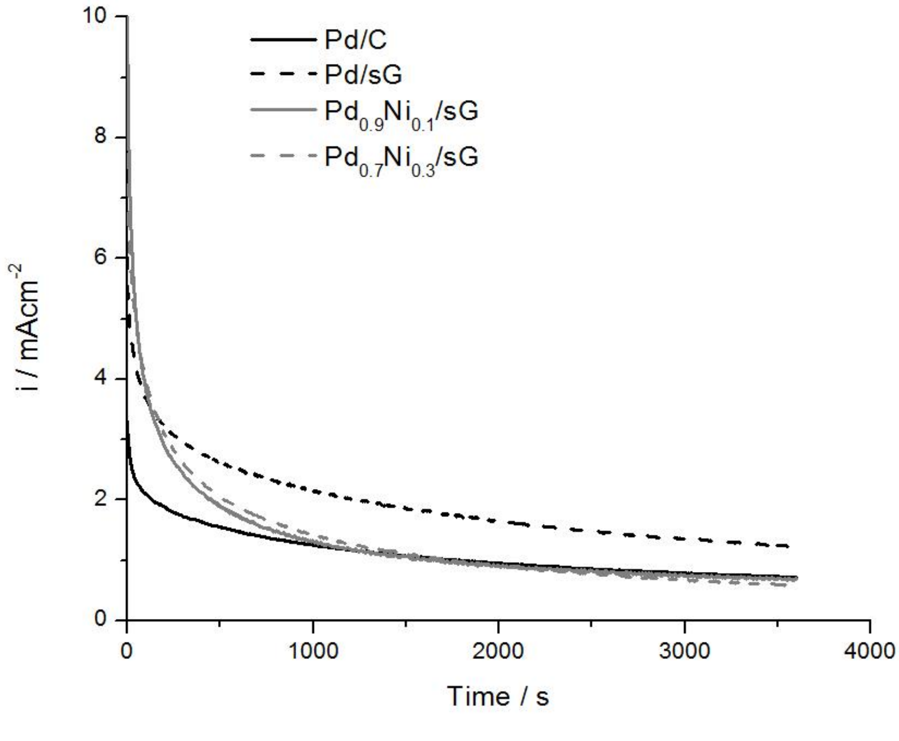

Figure 6-7: CA of all samples normalized by ECSA made by holding the potential at -0.2 V vs Hg/HgO for 1 h in a solution of 1 M KOH + 1 M ethanol

6.5 Conclusions

It was shown, that pure Pd nanoparticles could be deposited with a high level of dispersion on the surface of sG sheets and that they could express a catalytic activity about twice as high as Pd/C synthesized using the same method. This increase is thought to be caused by an increased amount of metal-support interface caused by a larger dispersion of the nanoparticles. The addition of Ni ions with Pd:Ni ratios of 9:1 and 7:3 during the nanoparticle synthesis has showed to cause large amount of agglomeration reducing the theoretical utilisation of the catalyst and decreasing the amount of three-phase boundary. PdNi/sG catalyst have shown to have an increased current density at higher potential compared to the pure Pd/sG catalyst which is thought to be caused by the supply of OH^- species from NiO sites neighbouring Pd reactive sites for the oxidation of adsorbed carbonaceous molecules. Pd/C and Pd/sG have similar stability with the current of the latter being twice as high. However Ni containing catalyst had a lower stability during prolonged operation which is attributed to their separation from the support caused by agglomeration rather than to a high level of surface poisoning. Overall, Pd_xNi_{1-x}/sG has shown to be a promising catalytic system for the EOR in alkaline media. However, the synthesis of the catalyst needs to be altered to obtained better dispersion of the nanoparticles to increase the stability of the catalysts.

As this study is incomplete, further characterizations are necessary to comprehend fully the behaviour of the catalysts for the EOR and to confirm the speculations made in this chapter. Suggested characterizations are, XRD measurements which would give the crystal structure of the Pd and Ni phases, XPS measurement which would show the oxidation state of the metallic atoms and help understand the surface composition of the catalysts and inductively coupled plasma mass spectrometry in order to obtain the actual Pd:Ni ratios of the synthesized nanoparticles. Also, samples containing different Pd:Ni ratios should be made in order to find the optimal Ni content.

6.6 Acknowledgements

I would like to acknowledge Dr. Chialiang Sun (Chang Gung University in Taiwan) and his team for the synthesis and supply of sulphonated graphene support. They also performed the TEM measurements for this chapter at their facility.

Chapter 7 : Direct Alkaline Ethanol Fuel Cell Test

7.1 Introduction

Ultimately, the goal of synthesizing more efficient electrocatalysts for alcohol electrooxidation is to improve the efficiency (lower overpotential) and power density ($mWcm^{-2}$) of direct alkaline fuel cell (DAFC). By developing such catalysts, it should be possible to obtain DAFCs systems with size, weight and power density comparable to internal combustion engines (ICEs) at comparable prices. Introducing such systems to the consumer market would reduce significantly the greenhouse gases produced by transportation for each ICE replaced by DAFC. This introduction could be followed by the gradual implementation of a renewable ethanol production cycle using biomass fermentation to further reduce CO_2 emissions. In this chapter, the best performing catalyst of **Chapter 3** was tested in an alkaline fuel cell using a commercially available membrane with varying fuel and electrolyte concentrations.

7.2 Experimental Setup

The fuel cell tests were made in a triode alkaline ethanol fuel cell which was designed and built in the department. The designed fuel cell consisted of three electrodes (one at the cathode and two at the anode) made of graphite with a circular geometry. The anode and the cathode are connected through a Bio-Logic potentiostat with the EC lab software package which measures the potential difference between the electrodes. Resistances are applied between the two working electrodes in order to induce a current between them which can be determined using the measured potential difference. The membrane electrode assembly is composed of two catalyst-coated carbon paper layers hot pressed on opposite sides of a commercially available anion exchange membrane (AEM) (Fumatech Fumasep® FAA-3-PK-130) at a pressure of 280 kg/cm^2 and a temperature of 105°C for 3 min. The cathode gas diffusion layer (GDL) catalyst was Pt/C 20 wt% with a metal loading of 0.5 mgcm^{-2} and the anode GDL catalyst was the synthesized Pd nanoparticles on oxide-supports with a Pd loading of 0.5 mgcm^{-2}. The catalysts used for dissolution were dissolved in 1 mL of ethanol and the catalysts weight equivalent of an ionomer solution (Fumatech Fumion® FAA-3 ionomer) 5 wt% in iso-propanol. The working area of the fuel cell was 7.9 cm^2 at the cathode and 5.9 cm^2 at the anode. The auxiliary electrode on the anode side can be used to apply a current between the cathode and anode side in order to increase to power output compared to the fuel cell in the conventional operation mode [215]–[217].

An exploded view of the fuel cell used can be observed in **Figure 7-1** where all the layers composing the fuel cell can be observed. The description of the components of the fuel cell will be made by starting with the AEM (yellow) and going outward on both sides simultaneously. As mentioned the membrane is an AEM resistant to high pH with a thickness of 130 μm and a diameter of 3.76 cm which is provided in bromide form. The Br^- anions were exchanged to OH^- anions by immersion of the membrane in 1 M NaOH for 72 h while changing the solution every 24 h after which it was kept in deionized water. On each side of the membrane is a GDL formed of carbon paper on which the mixtures of the cathodic and anodic catalysts were deposited on their respective side. These three components are those hot pressed together to form the membrane electrode assembly (MEA). After both GDL are the cathode and anode current collectors which contains the air and fuel channels respectively. The stainless steel entry tubes also act as the electrode contacts to form the closed circuit through the potentiostat. The cathode current collector possesses a channel from its side all the way to the middle in which a thermocouple can be inserted to measure the operating temperature and control it by communicating with a temperature controller connected to two heating pads situated on the exterior face of both current collectors. Those are enclosed by two insulating pads which direct the heat produced towards the MEA rather than to the environment. All of these are held together by two Teflon (electrical insulation) pads attached using stainless steel screws.

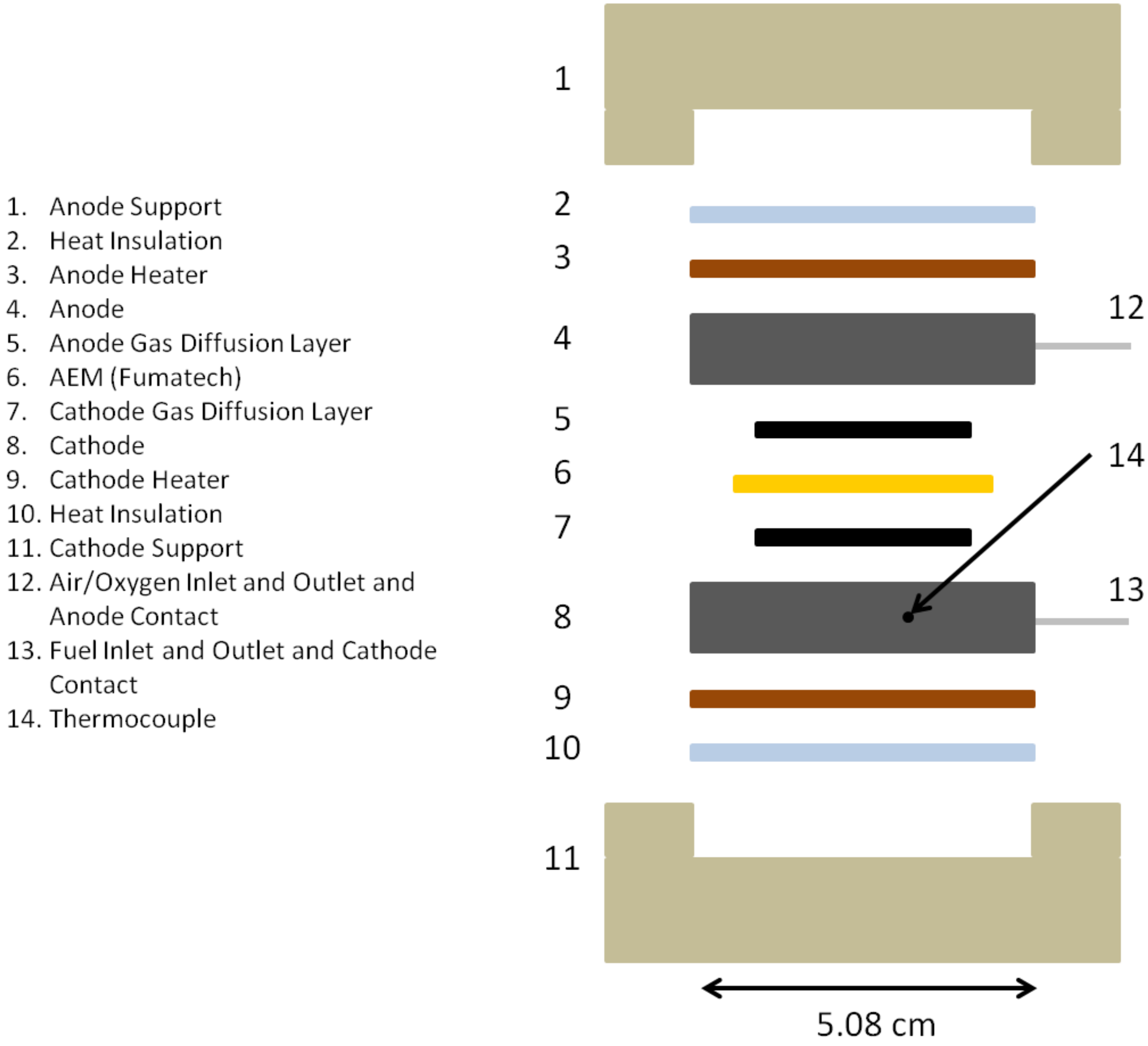

Figure 7-1: Exploded view of the designed fuel cell with parts descriptions.

In **Figure 7-2 (bottom)** the geometry of both electrodes can be observed. The reagents channels were made in a circular configuration to accommodate the additional electrode on the anode side. On both electrodes the stainless steel conduits used as inlets and outlets for the fuel and the air can be used as point of contact for electrical current. The auxiliary electrode is situated in the middle of the anode and separated from the latter using a Teflon sleeve to prevent direct electrical contact between the two.

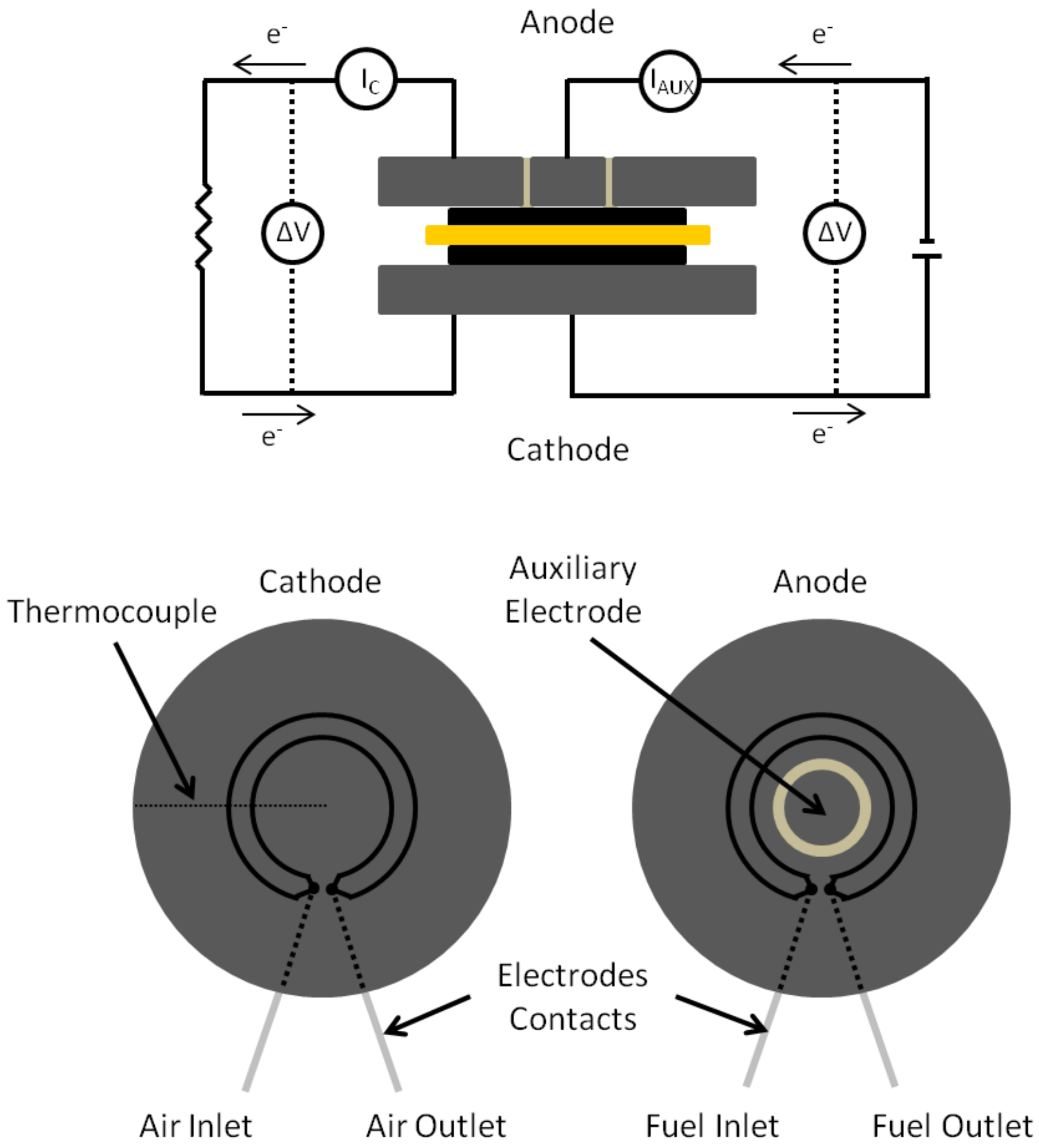

Figure 7-2: Side view of the MEA and current collectors with the electrical layout (top), top view of the geometry of the cathode and of the anode (bottom).

The electrical layout of the fuel cell is displayed in **Figure 7-2 (top).** First, the anode is connected to the cathode through an electrical connection containing a known resistance. When the fuel cell is in operation the electrons go from the anode to the cathode. The potential difference between the electrodes is measured using a voltmeter, a multimeter or a potentiostat and can be used to calculate the current and with it the power output of the fuel cell. The power output is varied by varying the resistance in the circuit. In a second circuit the cathode is connected to the auxiliary electrodes through a potentiostat. A current is applied between these electrodes in order to send electrons to the anode side. This transfer of electron would force hydroxyl species back to the cathode side where they would facilitate the oxygen reduction reaction. In order to have a beneficial effect the increase in power of the fuel cell has to be greater than the power sacrificed to the auxiliary electrode, a phenomenon (named power enhancement ratio) that was observed in certain cases [215]–[217] and that can be calculated using **Eq. 7.1**. If this ratio is found to be higher than one the power output of the fuel during triode operation is higher than that of conventional operation. Another variable that is used to analyse the effect of the auxiliary circuit is the power gain ratio calculated using **Eq. 7.2**. This ratio by how many times the power output of the fuel cell was increase compared to the current sacrificed to the auxiliary circuit. The power enhancement ratio has been showed to reach up to 1.32 [216] and the power gain reached 5.0 [215] in proton exchange membrane fuel cell (PEMFC) under high CO concentrations.

$$\boldsymbol{\rho_P = \frac{P_{FC}}{P_{FC}^0}} \tag{7.1}$$

$$\mathbf{\Lambda_P = \frac{P_{FC} - P_{FC}^0}{P_{aux}}} \tag{7.2}$$

Where ρ_P is the power enhancement ratio (unit-less), P_{FC} and $P^0{}_{FC}$ are the power obtained with the fuel cell under triode and normal operation in mW, respectively, P_{aux} is the power sacrifice to the auxiliary circuit in mW and Λ_P is the power gain ratio (unit-less).

7.3 Fuel Cell Tests Using a Commercially Available Anion Exchange Membrane

The catalyst of **Chapter 3** that was found to have the highest catalytic activity for the ethanol oxidation reaction (EOR) (Pd/TiO_2) was tested in the fuel cell as an anode catalyst using Pt/C 20wt% as the cathode catalyst for the oxygen reduction reaction (ORR).

A current going from the anode to the cathode is induced by connecting the two electrodes through a resistance. By varying the resistance applied between the electrodes, the current obtained varied and could be calculated using Ohm's law (**Eq. 7.3**) where V is the potential difference between the electrodes in V, R is the resistance applied in Ohms and I is the current in A. In **Figure 7-3 (top)** the current obtained is plotted against the potential difference between the electrodes. It can be observed that the open circuit voltage (OCV) increases with an increasing concentration of fuel and electrolyte which is expected. Also, an increase in the concentration of the fuel molecules and OH^- near the surface of the catalyst will increase the adsorption rate increasing the catalytic activity of the catalyst an effect that can be observed while going from a concentration of 0.1 M to 3 M.

$$\boldsymbol{I = \frac{V}{R}} \tag{7.3}$$

In **Figure 7-3 (bottom)** the power obtained from the operation of the fuel cell is calculated and plotted against the current observed. It can be observed that increasing the concentration of both fuel and electrolyte while keeping a ratio of 1:1 results in an increase in power. However studies have shown that a further increase in fuel and electrolyte concentration eventually leads to a decrease in power density [218], [219]. The power curves show to have a maximum before decreasing when the potential difference between the electrodes becomes too small and the increase in current is not enough to counter this change.

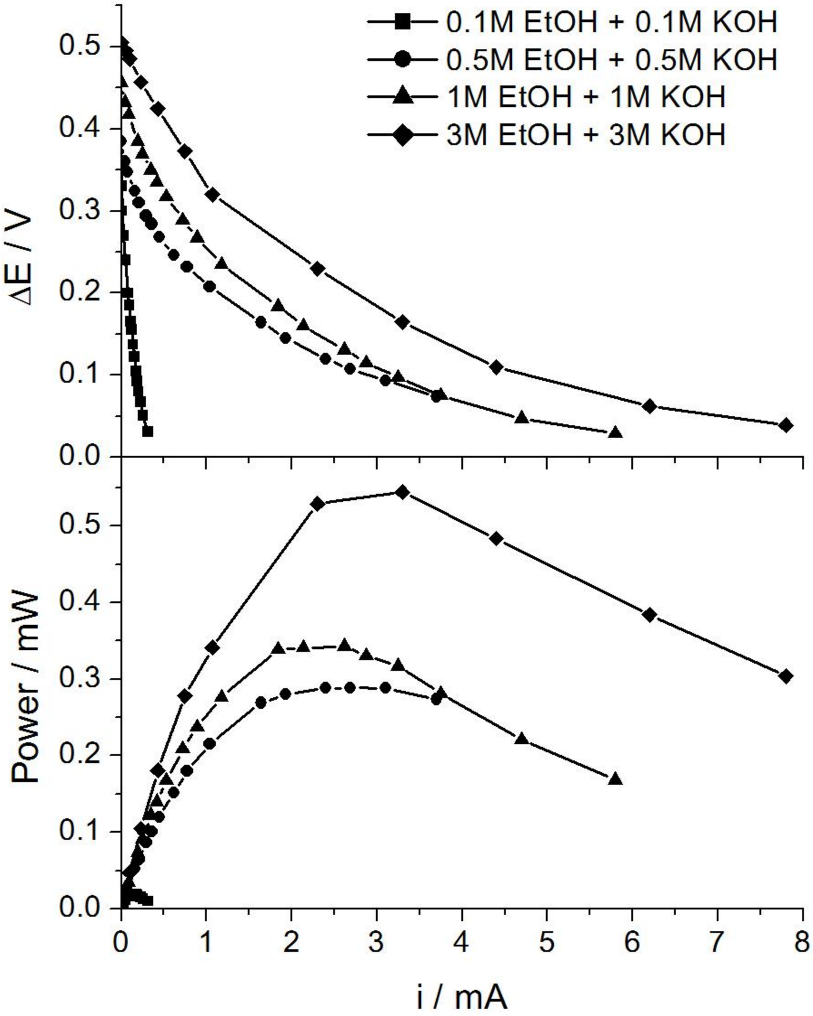

Figure 7-3: Power and potential difference plotted as a function of current density in an alkaline ethanol fuel cell using the synthesized Pd/TiO_2 as the anode catalyst and Pt 20 wt% on carbon black as cathode catalyst.

It was planned to make more experiments with the best catalyst in the fuel cell including varying the concentration of electrolyte with a fixed fuel concentration and vice-versa, operating at various temperature under the boiling point of the aqueous solution and applying a current between the cathode and the third electrode in order to promote the EOR. However, the unexpected low compatibility of the acquired membrane in alcohol due to a low level of cross-linking prevented further studies. The stability of the membrane, even at low concentrations of ethanol, was low and a constant decrease in current was observed. At higher ethanol concentration the membrane would be destroyed in less than an hour making further studies with this membrane obsolete.

7.4 Conclusion

The best performing catalyst from **Chapter 3** (Pd/TiO_2) was tested in a direct alkaline ethanol fuel cell (DAEFC) designed for this purpose. The designed fuel cell has the capability to operate in alkaline or acidic media with liquid and gaseous fuel. Also, an added feature allows the application a potential difference between the cathode and an auxiliary electrode in the attempt to increase the power output. The current and power output of the fuel cell was found to increase with increasing alcohol and electrolyte concentration with a molar ratio of 1:1 reaching values up to 7.8 mA and 0.55 mW respectively at 3 M. While the synthesized catalyst (Pd/TiO_2) shows to be a promising catalyst for DAEFC the instability of the commercial AEM used for the fuel cell tests in the presence of ethanol or other alcohol prevented further studies. In future work it will be necessary to obtain a highly conductive and highly stable AEM for fuel cell testing. With the new membrane more tests could be made to observe the activity of the catalysts towards the EOR: testing other catalysts, varying the fuel oxidizer ratios, varying the operating temperature, etc.

7.5 Acknowledgements

I would like to acknowledge Louis Germain Tremblay (University of Ottawa) for the manufacture of the designed fuel cell.

Chapter 8 : Summary of Conclusions

8.1 Conclusions

The objective of this work was to develop Pd and Pd-based nanocatalysts deposited on the surface of nanostructured reducible metal oxides and carbon-based supports and to test their activities for ethanol oxidation. The physical and chemical properties of these synthesized catalysts were characterized using various physicochemical and electrochemical techniques in order to observe the effect of the support on the catalyst activity and to quantify this activity towards the ethanol oxidation reaction (EOR). By normalising by electrochemical active surface area (ECSA) it was possible to observe the effect of the nature of the support on the reaction rate at the surface of the catalyst rather than apparent enhancement caused by the modification of the morphology of the catalytic system offering a larger ECSA.

In a first part, Pd nanoparticles were deposited using a metallic ion reduction method on the surface of MO_2 (M = Sn, Ce or Ti) particles. This deposition method yielded Pd nanoparticles with an average size ranging between 7 and 15 nm. The catalysts deposited on the metal oxides supports showed an increase current density compared to those deposited on carbon black by up to 100%. This increase in catalytic activity is ascribed to two phenomena: 1) The supply of OH^- groups from the surface of the support to neighboring groups on Pd reaction sites at lower potential. 2) An increase in Pd electron density, confirmed by a lower binding energy measured by XPS spectra, favoring the sharing of electrons between the catalyst and the reagents. Future work would focus on the control of the dispersion and of the size of the deposited nanoparticles on metal oxides to increase the utilisation of the synthesised catalysts.

Following those results, TiO_2-nanotubes (TiO_2-nts) were synthesised using anodization in a fluorine ion containing aqueous solution and were used as supports for Pd nanoparticles. Different modifications were made to the TiO_2-nts to tentatively increase the catalytic activity of the deposited nanoparticles. The Pd nanoparticles were deposited on the support using atomic layer deposition (ALD). It was found that annealing the support prior to deposition enhances the catalytic activity of the deposited catalyst and reduces the ethanol oxidation reaction onset potential. This is caused by a decreased electronic resistance of the support with the formation of the anatase phase. Also, the addition of a thin layer of SnO_2 using ALD on the surface of the TiO_2-nts showed a further increase of the catalytic activity of Pd which is attributed to an increased supply of OH^- groups from SnO_2 than from anatase TiO_2. Overall, the catalytic response of the catalytic system was increased by one order of magnitude compared to as grown TiO_2-nts. In future work, the effect of the thickness of the SnO_2 layer deposited on the TiO_2-nts should be study and could potentially lead to increase activity of the deposited catalysts.

Graphene, another carbon-based support was also used for Pd nanoparticles to which different Ni concentrations were added. The switch from carbon black to graphene resulted in an increased catalytic activity of the Pd catalyst comparable to that of going from carbon black to metal oxides. This increase is attributed to an increase in metal-support interface providing a larger amount of OH^- groups from the support following the effect observed on metal oxide supports. Furthermore, the addition of Ni to Pd during the synthesis has shown to cause an increase in current density at higher potential which is thought to be caused by the formation of NiOOH species near Pd reaction sites. Future work in this area would include the synthesis of catalysts containing other Ni concentration in order to find the optimal Pd:Ni ratio. Also, an optimization of the nanoparticle synthesis technique could reduce the amount of agglomeration observed for PdNi nanoparticles.

Finally, best working catalyst of out of the Pd deposited on MO_2 particles was tested in a direct alkaline ethanol fuel cell (DAEFC) using a commercially available anion exchange membrane (AEM). First, a triode fuel cell able to operate in both alkaline and acidic media only by changing the membrane used during operation was designed and built. Pd/TiO_2, which was found to be the best working catalyst, was tested in this fuel cell using a commercial AEM supplied by Fumatech and a Pt/C catalyst at the cathode. The current and power output of the fuel cell were found to increase with increasing alcohol and electrolyte concentration with a molar ratio of 1:1 reaching values up to 7.8mA and 0.55mW, respectively, at 3M. Unfortunately, the AEM was found to be unstable when immerged in solutions containing alcohol concentrations higher than 0.5M preventing further characterizations. The acquisition of a more stable membrane would allow further fuel cell tests with varying different parameters such as: varying the concentration of electrolyte with a fixed fuel concentration and vice-versa, operating at various temperatures and applying a current between the cathode and the auxiliary electrode.

In general, it was found that various metal oxides and graphene were promising support for the EOR on Pd nanoparticles due to their ability to modify the electronic structure of Pd and to supply the much needed OH^- species for the EOR. This increase in catalytic activity brings us one step closer to commercial DAEFC.

8.2 Future Work

While the results presented in this work are interesting, further work could improve the catalytic properties of the catalytic systems and help understand the related phenomena. In future works, the synthesis techniques could be adjusted in order to increase the dispersion, the utilisation and the ECSA of the catalysts. In-situ Fourier transform infrared spectroscopy would help in the understanding of the reaction mechanism of ethanol oxidation in alkaline media. The search for an anion exchange membrane more stable in alcohol solutions is under way which would allow further tests in the designed fuel cell. These tests would include the investigation of the optimal concentrations and ratio of ethanol to electrolyte in aqueous solution, the effect of the temperature of operation on the power output of the fuel cell, the effect of the use of pure oxygen rather than air and the operation of the fuel cell under the triode mode.

References

[1] A. Berger, F. Mesinger, and D. Šijački, *Climate Change: Inferences from Paleoclimate and Regional Aspects*, Springer. 2012, pp. 3–7.

[2] B. Medlyn and M. De Kauwe, “Carbon dioxide and water use in forests,” *Nature*, vol. 499, pp. 287–289, 2013.

[3] D. Charles, C. Stephen, B. Robert, P. Timothy, C. D. Keeling, S. C. Piper, R. B. Bacastow, M. Wahlen, T. P. Whorf, M. Heimann, and H. A. Meijer, “Exchanges of Atmospheric CO 2 and 13CO2 with the Terrestrial Biosphere and Oceans from 1978 to 2000 . I . Global Aspects,” *Scripps Inst. Oceanogr.*, pp. 1 – 29, 2001.

[4] G. P. Peters, R. M. Andrew, T. Boden, J. G. Canadell, P. Ciais, C. Le Quéré, G. Marland, M. R. Raupach, and C. Wilson, “The challenge to keep global warming below 2 °C,” *Nat. Clim. Chang.*, vol. 3, no. 1, pp. 4–6, Dec. 2013.

[5] C. Le Quéré, M. R. Raupach, J. G. Canadell, G. Marland, L. Bopp, P. Ciais, T. J. Conway, S. C. Doney, R. A. Feely, P. Foster, P. Friedlingstein, K. Gurney, R. A. Houghton, J. I. House, C. Huntingford, P. E. Levy, M. R. Lomas, J. Majkut, N. Metzl, J. P. Ometto, G. P. Peters, I. C. Prentice, J. T. Randerson, S. W. Running, J. L. Sarmiento, U. Schuster, S. Sitch, T. Takahashi, N. Viovy, G. R. van der Werf, and F. I. Woodward, “Trends in the sources and sinks of carbon dioxide,” *Nat. Geosci.*, vol. 2, no. 12, pp. 831–836, Nov. 2009.

[6] R. Dillon, S. Srinivasan, a. S. Aricò, and V. Antonucci, “International activities in DMFC R&D: status of technologies and potential applications,” *J. Power Sources*, vol. 127, no. 1–2, pp. 112–126, Mar. 2004.

[7] J. R. Mielenz, “Ethanol production from biomass: technology and commercialization status,” *Curr. Opin. Microbiol.*, vol. 4, no. 3, pp. 324–329, Jun. 2001.

[8] V. Putsche and D. Sandor, “Strategic, economic, and environmental issues for transportation fuels,” in *Handbook on Bioethanol: Production and Utilization*, Wyman CE, Ed. Washington DC: Taylor and Francis, 1996, pp. 21–35.

[9] W. W. Pulkrabek, *Engineering Fundamentals of the Internal Combustion Engine (2nd Ed.)*, vol. 126. Upper Saddle River: Prentice Hall, 2003, p. 59.

[10] U.S. Department of Energy, “Fuel Cells,” *Energy Effic. Renew. Energy*, 2010.

[11] J. H. Hirschenhofer, D. B. Stauffer, R. R. Engleman, and M. G. Klett, *Fuel Cell Handbook (4th Ed.)*. Reading: Parsons Corporation, 1998, pp. 2–20.

[12] C. Ronneau, *Énergie , pollution de l'air et développement durable*. Louvain-la-Neuve: Presses Universitaires de Louvain, 2004, p. 88.

[13] M. O. Hamdan, M. Y. E. Selim, S.-A. B. Al-Omari, and E. Elnajjar, "Hydrogen supplement co-combustion with diesel in compression ignition engine," *Renew. Energy*, pp. 1–7, 2014.

[14] C. Lamy, E. M. Belgsir, and J.-M. Léger, "Electrocatalytic oxidation of aliphatic alcohols : Application to the direct alcohol fuel cell (DAFC)," *J. Appl. Electrochem.*, pp. 799–809, 2001.

[15] L. Dong, R. R. S. Gari, Z. Li, M. M. Craig, and S. Hou, "Graphene-supported platinum and platinum–ruthenium nanoparticles with high electrocatalytic activity for methanol and ethanol oxidation," *Carbon N. Y.*, vol. 48, no. 3, pp. 781–787, Mar. 2010.

[16] R. C. Cerritos, M. Guerra-Balcázar, R. F. Ramírez, J. Ledesma-García, and L. G. Arriaga, "Morphological Effect of Pd Catalyst on Ethanol Electro-Oxidation Reaction," *Materials (Basel).*, vol. 5, no. 12, pp. 1686–1697, Sep. 2012.

[17] L. Zhou, "Progress and problems in hydrogen storage methods," *Renew. Sustain. Energy Rev.*, vol. 9, no. 4, pp. 395–408, Aug. 2005.

[18] M. Felderhoff, C. Weidenthaler, R. von Helmolt, and U. Eberle, "Hydrogen storage: the remaining scientific and technological challenges," *Phys. Chem. Chem. Phys.*, vol. 9, no. 21, pp. 2643–53, Jun. 2007.

[19] U.S. Department of Energy, "Clean Cities Alternative Fuel Price Report," *Energy Effic. Renew. Energy*, pp. 1–17, 2014.

[20] Y. Paik, S.-S. Kim, and O. H. Han, "Spatial distribution of reaction products in direct ethanol fuel cell," *Electrochem. commun.*, vol. 11, no. 2, pp. 302–304, Feb. 2009.

[21] K. S. Roelofs, T. Hirth, and T. Schiestel, "Dihydrogenimidazole modified silica-sulphonated poly(ether ether ketone) hybrid materials as electrolyte membranes for direct ethanol fuel cells," *Mater. Sci. Eng. B*, vol. 176, no. 9, pp. 727–735, May 2011.

[22] J. Perez, V. A. Paganin, and E. Antolini, "Particle size effect for ethanol electro-oxidation on Pt/C catalysts in half-cell and in a single direct ethanol fuel cell," *J. Electroanal. Chem.*, vol. 654, no. 1–2, pp. 108–115, May 2011.

[23] E. H. Yu, U. Krewer, and K. Scott, "Principles and Materials Aspects of Direct Alkaline Alcohol Fuel Cells," *Energies*, vol. 3, no. 8, pp. 1499–1528, Aug. 2010.

[24] E. Antolini and E. R. Gonzalez, "Alkaline direct alcohol fuel cells," *J. Power Sources*, vol. 195, no. 11, pp. 3431–3450, Jun. 2010.

[25] F. Hu, C. Chen, Z. Wang, G. Wei, and P. K. Shen, "Mechanistic study of ethanol oxidation on Pd–NiO/C electrocatalyst," *Electrochim. Acta*, vol. 52, no. 3, pp. 1087–1091, Nov. 2006.

[26] C. Xu, P. K. Shen, and Y. Liu, "Ethanol electrooxidation on Pt/C and Pd/C catalysts promoted with oxide," *J. Power Sources*, vol. 164, no. 2, pp. 527–531, Feb. 2007.

[27] R. Slade and J. Varcoe, "Investigations of conductivity in FEP-based radiation-grafted alkaline anion-exchange membranes," *Solid State Ionics*, vol. 176, no. 5–6, pp. 585–597, Feb. 2005.

[28] C. Bianchini and P. K. Shen, "Palladium-based electrocatalysts for alcohol oxidation in half cells and in direct alcohol fuel cells.," *Chem. Rev.*, vol. 109, no. 9, pp. 4183–206, Sep. 2009.

[29] I. Kim, O. H. Han, S. A. Chae, Y. Paik, S.-H. Kwon, K.-S. Lee, Y.-E. Sung, and H. Kim, "Catalytic reactions in direct ethanol fuel cells.," *Angew. Chem. Int. Ed. Engl.*, vol. 50, no. 10, pp. 2270–4, Mar. 2011.

[30] Y.-H. Qin, H.-H. Yang, X.-S. Zhang, P. Li, and C.-A. Ma, "Effect of carbon nanofibers microstructure on electrocatalytic activities of Pd electrocatalysts for ethanol oxidation in alkaline medium," *Int. J. Hydrogen Energy*, vol. 35, no. 15, pp. 7667–7674, Aug. 2010.

[31] R. Kavanagh, X. Cao, W. Lin, C. Hardacre, and P. Hu, "Acetaldehyde Production in the Direct Ethanol Fuel Cell : Mechanistic Elucidation by Density Functional Theory," *J. Phys. Chem. C*, vol. 156, pp. 7185–88, 2012.

[32] R. F. B. De Souza, G. S. Buzzo, J. C. M. Silva, E. V. Spinacé, a. O. Neto, and M. H. M. T. Assumpção, "Effect of TiO2 Content on Ethanol Electrooxidation in Alkaline Media Using Pt Nanoparticles Supported on Physical Mixtures of Carbon and TiO2 as Electrocatalysts," *Electrocatalysis*, vol. 5, no. 2, pp. 213–219, Jan. 2014.

[33] K. J. Klabunde, J. Stark, O. Koper, C. Mohs, D. G. Park, S. Decker, Y. Jiang, I. Lagadic, and D. Zhang, "Nanocrystals as Stoichiometric Reagents with Unique Surface Chemistry," *J. Phys. Chem.*, vol. 100, pp. 12142–12153, 1996.

[34] R. J. Gilliam, D. W. Kirk, and S. J. Thorpe, "Influence of Structural, Microstructural and Electrical Properties on Electrocatalytic Performance at the Nanoscale," *Electrocatalysis*, vol. 2, no. 1, pp. 1–19, Feb. 2011.

[35] A. Antonelli and K.- Wilsdorf, "Size dependence of the lattice parameter for Pd clusters: A molecular-dynamics study," vol. 54, no. 23, pp. 57–60, 1996.

[36] R. Lamber, S. Wetjen, and N. I. Jaeger, "Size dependance of the lattice parameter of small palladium particles," *Phys. Rev. B*, vol. 51, no. 16, pp. 10968–10971, 1995.

[37] J. S. Vermaak, C. W. Mays, and D. Kuhlmann-Wilsdorf, “On surface stress and surface tension,” *Surf. Sci.*, vol. 12, pp. 128–133, 1968.

[38] S. C. S. Lai and M. T. M. Koper, “Ethanol electro-oxidation on platinum in alkaline media.,” *Phys. Chem. Chem. Phys.*, vol. 11, no. 44, pp. 10446–56, Nov. 2009.

[39] S. T. Nguyen, H. M. Law, H. T. Nguyen, N. Kristian, S. Wang, S. H. Chan, and X. Wang, “Enhancement effect of Ag for Pd/C towards the ethanol electro-oxidation in alkaline media,” *Appl. Catal. B Environ.*, vol. 91, no. 1–2, pp. 507–515, Sep. 2009.

[40] C. Xu, L. Cheng, P. Shen, and Y. Liu, “Methanol and ethanol electrooxidation on Pt and Pd supported on carbon microspheres in alkaline media,” *Electrochem. commun.*, vol. 9, no. 5, pp. 997–1001, May 2007.

[41] H. T. Zheng, Y. Li, S. Chen, and P. K. Shen, “Effect of support on the activity of Pd electrocatalyst for ethanol oxidation,” *J. Power Sources*, vol. 163, no. 1, pp. 371–375, Dec. 2006.

[42] Y. Chen, L. Zhuang, and J. Lu, “Non-Pt Anode Catalysts for Alkaline Direct Alcohol Fuel Cells,” *Chinese J. Catal.*, vol. 28, no. 10, pp. 870–874, Oct. 2007.

[43] H. Wang, C. Xu, F. Cheng, and S. Jiang, “Pd nanowire arrays as electrocatalysts for ethanol electrooxidation,” *Electrochem. commun.*, vol. 9, no. 5, pp. 1212–1216, May 2007.

[44] R. M. Modibedi, T. Masombuka, and M. K. Mathe, “Carbon supported Pd–Sn and Pd–Ru–Sn nanocatalysts for ethanol electro-oxidation in alkaline medium,” *Int. J. Hydrogen Energy*, vol. 36, no. 8, pp. 4664–4672, Apr. 2011.

[45] Q. He, W. Chen, S. Mukerjee, S. Chen, and F. Laufek, “Carbon-supported PdM (M=Au and Sn) nanocatalysts for the electrooxidation of ethanol in high pH media,” *J. Power Sources*, vol. 187, no. 2, pp. 298–304, Feb. 2009.

[46] T. Maiyalagan and K. Scott, “Performance of carbon nanofiber supported Pd–Ni catalysts for electro-oxidation of ethanol in alkaline medium,” *J. Power Sources*, vol. 195, no. 16, pp. 5246–5251, Aug. 2010.

[47] Z. Zhang, L. Xin, K. Sun, and W. Li, “Pd–Ni electrocatalysts for efficient ethanol oxidation reaction in alkaline electrolyte,” *Int. J. Hydrogen Energy*, vol. 36, no. 20, pp. 12686–12697, Oct. 2011.

[48] L. D. Zhu, T. S. Zhao, J. B. Xu, and Z. X. Liang, “Preparation and characterization of carbon-supported sub-monolayer palladium decorated gold nanoparticles for the electro-oxidation of ethanol in alkaline media,” *J. Power Sources*, vol. 187, no. 1, pp. 80–84, Feb. 2009.

[49] S. Y. Shen, T. S. Zhao, J. B. Xu, and Y. S. Li, “Synthesis of PdNi catalysts for the oxidation of ethanol in alkaline direct ethanol fuel cells,” *J. Power Sources*, vol. 195, no. 4, pp. 1001–1006, Feb. 2010.

[50] K.-W. Park, J.-H. Choi, B.-K. Kwon, S.-A. Lee, Y.-E. Sung, H.-Y. Ha, S.-A. Hong, H. Kim, and A. Wieckowski, “Chemical and Electronic Effects of Ni in Pt/Ni and Pt/Ru/Ni Alloy Nanoparticles in Methanol Electrooxidation,” *J. Phys. Chem. B*, vol. 106, no. 8, pp. 1869–1877, Feb. 2002.

[51] J.-H. Choi, K.-W. Park, B.-K. Kwon, and Y.-E. Sung, “Methanol Oxidation on Pt/Ru, Pt/Ni, and Pt/Ru/Ni Anode Electrocatalysts at Different Temperatures for DMFCs,” *J. Electrochem. Soc.*, vol. 150, no. 7, p. A973, 2003.

[52] Z.-B. Wang, P.-J. Zuo, G.-J. Wang, C.-Y. Du, and G.-P. Yin, “Effect of Ni on PtRu/C Catalyst Performance for Ethanol Electrooxidation in Acidic Medium,” *J. Phys. Chem. C*, vol. 112, no. 16, pp. 6582–6587, Apr. 2008.

[53] E. Ribadeneira and B. A. Hoyos, “Evaluation of Pt–Ru–Ni and Pt–Sn–Ni catalysts as anodes in direct ethanol fuel cells,” *J. Power Sources*, vol. 180, no. 1, pp. 238–242, May 2008.

[54] Z. Wen, S. Yang, Y. Liang, W. He, H. Tong, L. Hao, X. Zhang, and Q. Song, “The improved electrocatalytic activity of palladium/graphene nanosheets towards ethanol oxidation by tin oxide,” *Electrochim. Acta*, vol. 56, no. 1, pp. 139–144, Dec. 2010.

[55] M. R. Tarasevich, Z. R. Karichev, V. A. Bogdanovskaya, E. N. Lubnin, and A. V. Kapustin, “Kinetics of ethanol electrooxidation at RuNi catalysts,” *Electrochem. commun.*, vol. 7, no. 2, pp. 141–146, Feb. 2005.

[56] J.-W. Kim and S.-M. Park, “In Situ XANES Studies of Electrodeposited Nickel Oxide Films with Metal Additives for the Electro-Oxidation of Ethanol,” *J. Electrochem. Soc.*, vol. 150, no. 11, pp. E560–6, 2003.

[57] J. Kim and S. Park, “Electrochemical Oxidation of Ethanol at Thermally Prepared RuO 2 -Modified Electrodes in Alkaline Media,” *J. Electrochem. Soc.*, vol. 146, no. 3, pp. 1075–1080, 1999.

[58] J. Friedl and U. Stimming, “Model catalyst studies on hydrogen and ethanol oxidation for fuel cells,” *Electrochim. Acta*, vol. 101, pp. 41–58, Jul. 2013.

[59] Z. X. Liang, T. S. Zhao, J. B. Xu, and L. D. Zhu, “Mechanism study of the ethanol oxidation reaction on palladium in alkaline media,” *Electrochim. Acta*, vol. 54, no. 8, pp. 2203–2208, Mar. 2009.

[60] A. Santasalo-Aarnio, P. Peljo, E. Aspberg, K. Kontturi, and T. Kallio, “Methanol, Ethanol and Iso-propanol Performance in Alkaline Direct Alcohol Fuel Cell (ADAFC),” *ECS Trans.*, vol. 33, no. 1, pp. 1701–1714, 2010.

[61] N. Fujiwara, Z. Siroma, S. Yamazaki, T. Ioroi, H. Senoh, and K. Yasuda, “Direct ethanol fuel cells using an anion exchange membrane,” *J. Power Sources*, vol. 185, no. 2, pp. 621–626, Dec. 2008.

[62] H. Hou, G. Sun, R. He, Z. Wu, and B. Sun, “Alkali doped polybenzimidazole membrane for high performance alkaline direct ethanol fuel cell,” *J. Power Sources*, vol. 182, no. 1, pp. 95–99, Jul. 2008.

[63] V. Bambagioni, C. Bianchini, A. Marchionni, J. Filippi, F. Vizza, J. Teddy, P. Serp, and M. Zhiani, “Pd and Pt–Ru anode electrocatalysts supported on multi-walled carbon nanotubes and their use in passive and active direct alcohol fuel cells with an anion-exchange membrane (alcohol=methanol, ethanol, glycerol),” *J. Power Sources*, vol. 190, no. 2, pp. 241–251, May 2009.

[64] Z. X. Liang, T. S. Zhao, J. B. Xu, and L. D. Zhu, “Mechanism study of the ethanol oxidation reaction on palladium in alkaline media,” *Electrochim. Acta*, vol. 54, no. 8, pp. 2203–2208, Mar. 2009.

[65] L. An and T. S. Zhao, “An alkaline direct ethanol fuel cell with a cation exchange membrane,” *Energy Environ. Sci.*, vol. 4, no. 6, pp. 2213–7, 2011.

[66] S. Uhm, Y. Yi, and J. Lee, “Electrocatalytic Activity of Pd–CeO2 Nanobundle in an Alkaline Ethanol Oxidation,” *Catal. Letters*, vol. 138, no. 1–2, pp. 46–49, Jun. 2010.

[67] V. Bambagioni, C. Bianchini, Y. Chen, J. Filippi, P. Fornasiero, M. Innocenti, A. Lavacchi, A. Marchionni, W. Oberhauser, and F. Vizza, “Energy efficiency enhancement of ethanol electrooxidation on Pd-CeO(2)/C in passive and active polymer electrolyte-membrane fuel cells.,” *ChemSusChem*, vol. 5, no. 7, pp. 1266–73, Jul. 2012.

[68] C. Xu, R. Zeng, P. K. Shen, and Z. Wei, “Synergistic effect of CeO2 modified Pt/C catalysts on the alcohols oxidation,” *Electrochim. Acta*, vol. 51, no. 6, pp. 1031–1035, Nov. 2005.

[69] C. Xu and P. K. Shen, “Electrochamical oxidation of ethanol on Pt-CeO2/C catalysts,” *J. Power Sources*, vol. 142, no. 1–2, pp. 27–29, Mar. 2005.

[70] H. Mao, L. Wang, P. Zhu, Q. Xu, and Q. Li, “Carbon-supported PdSn–SnO2 catalyst for ethanol electro-oxidation in alkaline media,” *Int. J. Hydrogen Energy*, vol. 39, no. 31, pp. 17583–17588, Oct. 2014.

[71] L. Jiang, L. Colmenares, Z. Jusys, G. Q. Sun, and R. J. Behm, “Ethanol electrooxidation on novel carbon supported Pt/SnOx/C catalysts with varied Pt:Sn ratio,” *Electrochim. Acta*, vol. 53, no. 2, pp. 377–389, Dec. 2007.

[72] Y. Ren, S. Zhang, and H. Li, “Electro-oxidation of methanol on SnO2-promoted Pd/MWCNTs catalysts in alkaline solution,” *Int. J. Hydrogen Energy*, vol. 39, no. 1, pp. 288–296, Jan. 2014.

[73] S. G. de Silva, M. H. M. T. Assumpção, J. C. M. Silva, R. F. B. De Souza, E. V Spinacé, A. O. Neto, and G. S. Buzzo, “PdSn / C Electrocatalysts with Different Atomic Ratios for Ethanol Electro-Oxidation in Alkaline Media,” *Int. J. Electrochem. Sci.*, vol. 9, pp. 5416–24, 2014.

[74] M. Wang, D. Guo, and H. Li, “High activity of novel Pd/TiO2 nanotube catalysts for methanol electro-oxidation,” *J. Solid State Chem.*, vol. 178, no. 6, pp. 1996–2000, Jun. 2005.

[75] F. Hu, F. Ding, S. Song, and P. K. Shen, “Pd electrocatalyst supported on carbonized TiO2 nanotube for ethanol oxidation,” *J. Power Sources*, vol. 163, no. 1, pp. 415–419, Dec. 2006.

[76] Y.-H. Qin, Y. Zhuang, R.-L. Lv, T.-L. Wang, W.-G. Wang, and C.-W. Wang, “Pd nanoparticles anchored on carbon-doped TiO2 nanocoating support for ethanol electrooxidation in alkaline media,” *Electrochim. Acta*, vol. 154, pp. 77–82, Feb. 2015.

[77] J. C. M. Silva, G. S. Buzzo, R. F. B. De Souza, E. V. Spinacé, a. O. Neto, and M. H. M. T. Assumpção, “Enhanced Electrooxidation of Ethanol Using Pd/C + TiO2 Electrocatalysts in Alkaline Media,” *Electrocatalysis*, vol. 2, pp. 2–7, Aug. 2014.

[78] B. Ohtani, Y. Okugawa, S. Nishimoto, and T. Kagiya, “Photocatalytic Activity of TiO2 Powders Suspended in Aqueous Silver Nitrate Solution. Correlation with pH-Dependent Surface Structures,” *J. Phys. Chem.*, vol. 91, no. 13, pp. 3550–55, 1987.

[79] L. Zang, C.-Y. Liu, and X.-M. Ren, “Adsorption of Cations on TiO2 Particles. A Method to Determine the Surface Density of OH Groups,” *Chem. Commun.*, pp. 1865–6, 1994.

[80] C. Xu, Z. Tian, P. Shen, and S. P. Jiang, “Oxide (CeO2, NiO, Co3O4 and Mn3O4)-promoted Pd/C electrocatalysts for alcohol electrooxidation in alkaline media,” *Electrochim. Acta*, vol. 53, no. 5, pp. 2610–2618, Jan. 2008.

[81] C. Xu, P. K. Shen, X. Ji, R. Zeng, and Y. Liu, “Enhanced activity for ethanol electrooxidation on Pt–MgO/C catalysts,” *Electrochem. commun.*, vol. 7, no. 12, pp. 1305–1308, Dec. 2005.

[82] Y. Bai, J. Wu, J. Xi, J. Wang, W. Zhu, L. Chen, and X. Qiu, "Electrochemical oxidation of ethanol on Pt–ZrO2/C catalyst," *Electrochem. commun.*, vol. 7, no. 11, pp. 1087–1090, Nov. 2005.

[83] S. Chen, M. Malig, M. Tian, and A. Chen, "Electrocatalytic Activity of PtAu Nanoparticles Deposited on TiO2 Nanotubes," *J. Phys. Chem. C*, vol. 116, no. 5, pp. 3298–3304, 2012.

[84] J. M. Macak, P. J. Barczuk, H. Tsuchiya, M. Z. Nowakowska, a. Ghicov, M. Chojak, S. Bauer, S. Virtanen, P. J. Kulesza, and P. Schmuki, "Self-organized nanotubular TiO2 matrix as support for dispersed Pt/Ru nanoparticles: Enhancement of the electrocatalytic oxidation of methanol," *Electrochem. commun.*, vol. 7, no. 12, pp. 1417–1422, Dec. 2005.

[85] M. Hosseini and M. M. Momeni, "Praparation and characterisation of TiO2 nanotubular arrays for electro-oxidation of organic compounds: effect of immobilization of the noble metal particles," *Int. J. Mod. Phys. Conf. Ser.*, vol. 5, pp. 41–48, Jan. 2012.

[86] M. G. Hosseini, M. M. Momeni, and M. Faraji, "Preparation and electrocatalytic activity of gold nanoparticle embedded in highly ordered TiO2 nanotube array electrode for electro-oxidation of galactose," *Surf. Eng.*, vol. 27, no. 10, pp. 784–789, Sep. 2011.

[87] M. G. Hosseini, S. a. S. Sajjadi, and M. M. Momeni, "Electrodeposition of platinum metal on titanium and anodised titanium from P salt: application to electro-oxidation of glycerol," *Surf. Eng.*, vol. 23, no. 6, pp. 419–424, Nov. 2007.

[88] H. Song, X. Qiu, X. Li, F. Li, W. Zhu, and L. Chen, "TiO2 nanotubes promoting Pt/C catalysts for ethanol electro-oxidation in acidic media," *J. Power Sources*, vol. 170, no. 1, pp. 50–54, Jun. 2007.

[89] W. Xu, S. Zhu, Z. Li, Z. Cui, and X. Yang, "Synthesis and catalytic properties of Pd nanoparticles loaded nanoporous TiO2 material," *Electrochim. Acta*, vol. 114, pp. 35–41, Dec. 2013.

[90] Y.-H. Qin, H.-H. Yang, R.-L. Lv, W.-G. Wang, and C.-W. Wang, "TiO2 nanotube arrays supported Pd nanoparticles for ethanol electrooxidation in alkaline media," *Electrochim. Acta*, vol. 106, pp. 372–7, Sep. 2013.

[91] Y. Li, L. Tang, and J. Li, "Preparation and electrochemical performance for methanol oxidation of pt/graphene nanocomposites," *Electrochem. commun.*, vol. 11, no. 4, pp. 846–849, Apr. 2009.

[92] S. M. Choi, M. H. Seo, H. J. Kim, and W. B. Kim, "Synthesis of surface-functionalized graphene nanosheets with high Pt-loadings and their applications to methanol electrooxidation," *Carbon N. Y.*, vol. 49, no. 3, pp. 904–9, Mar. 2011.

[93] J. Liu, H. Zhou, Q. Wang, F. Zeng, and Y. Kuang, "Reduced graphene oxide supported palladium–silver bimetallic nanoparticles for ethanol electro-oxidation in alkaline media," *J. Mater. Sci.*, vol. 47, no. 5, pp. 2188–94, Oct. 2012.

[94] Z. Huang, H. Zhou, C. Li, F. Zeng, C. Fu, and Y. Kuang, "Preparation of well-dispersed PdAu bimetallic nanoparticles on reduced graphene oxide sheets with excellent electrochemical activity for ethanol oxidation in alkaline media," *J. Mater. Chem.*, vol. 22, no. 5, pp. 1781–5, 2012.

[95] R. Awasthi and R. N. Singh, "Graphene-supported Pd–Ru nanoparticles with superior methanol electrooxidation activity," *Carbon N. Y.*, vol. 51, pp. 282–9, Jan. 2013.

[96] M. H. Seo, S. M. Choi, J. K. Seo, S. H. Noh, W. B. Kim, and B. Han, "The graphene-supported palladium and palladium–yttrium nanoparticles for the oxygen reduction and ethanol oxidation reactions: Experimental measurement and computational validation," *Appl. Catal. B Environ.*, vol. 129, pp. 163–171, Jan. 2013.

[97] L. J. Wu, Y. Wang, Y. P. Wang, X. Du, F. Wang, Y. Y. Gao, T. Qi, and C. M. Li, "Thermally treated 3-D nanostructured graphene-supported Pd catalyst for significantly improved electrocatalytic performance towards ethanol electrooxidation," *RSC Adv.*, vol. 3, no. 15, pp. 5196–203, 2013.

[98] R. N. Singh and R. Awasthi, "Graphene support for enhanced electrocatalytic activity of Pd for alcohol oxidation," *Catal. Sci. Technol.*, vol. 1, no. 5, pp. 778–83, 2011.

[99] Y. Li, W. Gao, L. Ci, C. Wang, and P. M. Ajayan, "Catalytic performance of Pt nanoparticles on reduced graphene oxide for methanol electro-oxidation," *Carbon N. Y.*, vol. 48, no. 4, pp. 1124–1130, Apr. 2010.

[100] C. Hu, H. Cheng, Y. Zhao, Y. Hu, Y. Liu, L. Dai, and L. Qu, "Newly-designed complex ternary Pt/PdCu nanoboxes anchored on three-dimensional graphene framework for highly efficient ethanol oxidation.," *Adv. Mater.*, vol. 24, no. 40, pp. 5493–8, Oct. 2012.

[101] H. J. Wang, H. Yu, F. Peng, and P. Lv, "Methanol electrocatalytic oxidation on highly dispersed Pt/sulphonated-carbon nanotubes catalysts," *Electrochem. commun.*, vol. 8, no. 3, pp. 499–504, Mar. 2006.

[102] Z.-P. Sun, X.-G. Zhang, R.-L. Liu, Y.-Y. Liang, and H.-L. Li, "A simple approach towards sulphonated multi-walled carbon nanotubes supported by Pd catalysts for methanol electro-oxidation," *J. Power Sources*, vol. 185, no. 2, pp. 801–806, Dec. 2008.

[103] C.-L. Sun, J.-S. Tang, N. Brazeau, J.-J. Wu, S. Ntais, C.-W. Yin, H.-L. Chou, and E. a. Baranova, "Particle size effects of sulphonated graphene supported Pt nanoparticles on ethanol electrooxidation," *Electrochim. Acta*, Dec. 2014.

[104] J. K. Nørskov, J. Rossmeisl, A. Logadottir, L. Lindqvist, J. R. Kitchin, T. Bligaard, and H. Jónsson, "Origin of the Overpotential for Oxygen Reduction at a Fuel-Cell Cathode," *J. Phys. Chem. B*, vol. 108, no. 46, pp. 17886–17892, 2004.

[105] T. Toda, H. Igarashi, H. Uchida, and M. Watanabe, "Enhancement of the Electroreduction of Oxygen on Pt Alloys with Fe , Ni , and Co," *J. Electrochem. Soc.*, vol. 146, no. 10, pp. 3750–3756, 1999.

[106] C. Jeyabharathi, P. Venkateshkumar, J. Mathiyarasu, and K. L. N. Phani, "Platinum–tin bimetallic nanoparticles for methanol tolerant oxygen-reduction activity," *Electrochim. Acta*, vol. 54, no. 2, pp. 448–454, Dec. 2008.

[107] K. Sasaki, Y. Mo, J. X. Wang, M. Balasubramanian, F. Uribe, J. McBreen, and R. R. Adzic, "Pt submonolayers on metal nanoparticles—novel electrocatalysts for H2 oxidation and O2 reduction," *Electrochim. Acta*, vol. 48, no. 25–26, pp. 3841–3849, Nov. 2003.

[108] E. Antolini, R. R. Passos, and E. A. Ticianelli, "Electrocatalysis of oxygen reduction on a carbon supported platinum - vanadium alloy in polymer electrolyte fuel cells," *Electrochim. Acta*, vol. 48, no. 3, pp. 263–270, 2002.

[109] S. Mukerjee, S. Srinivasan, M. P. Soriaga, and J. Mcbreen, "Role of Structural and Electronic Properties of Pt and Pt Alloys on Electrocatalysis of Oxygen Reduction," *J. Electrochem. Soc.*, vol. 142, no. 5, pp. 1409–22, 1995.

[110] F. Bidault, D. J. L. Brett, P. H. Middleton, and N. P. Brandon, "Review of gas diffusion cathodes for alkaline fuel cells," *J. Power Sources*, vol. 187, no. 1, pp. 39–48, Feb. 2009.

[111] D. Zhang, D. Chi, T. Okajima, and T. Ohsaka, "Catalytic activity of dual catalysts system based on nano-manganese oxide and cobalt octacyanophthalocyanine toward four-electron reduction of oxygen in alkaline media," *Electrochim. Acta*, vol. 52, no. 17, pp. 5400–5406, May 2007.

[112] A. Verma, A. Jha, and S. Basu, "Manganese dioxide as a cathode catalyst for a direct alcohol or sodium borohydride fuel cell with a flowing alkaline electrolyte," *J. Power Sources*, vol. 141, no. 1, pp. 30–34, Feb. 2005.

[113] I. Roche, E. Chaînet, M. Chatenet, and J. Vondrák, "Carbon-Supported Manganese Oxide Nanoparticles as Electrocatalysts for the Oxygen Reduction Reaction (ORR) in Alkaline Medium: Physical Characterizations and ORR Mechanism," *J. Phys. Chem. C*, vol. 111, no. 3, pp. 1434–1443, Jan. 2007.

[114] L. Mao, "Mechanistic study of the reduction of oxygen in air electrode with manganese oxides as electrocatalysts," *Electrochim. Acta*, vol. 48, no. 8, pp. 1015–1021, Apr. 2003.

[115] F. H. B. Lima, M. L. Calegaro, and E. A. Ticianelli, “Investigations of the catalytic properties of manganese oxides for the oxygen reduction reaction in alkaline media,” *J. Electroanal. Chem.*, vol. 590, no. 2, pp. 152–160, May 2006.

[116] Y. Liang, Y. Li, H. Wang, J. Zhou, J. Wang, T. Regier, and H. Dai, “Co3O4 nanocrystals on graphene as a synergistic catalyst for oxygen reduction reaction.,” *Nat. Mater.*, vol. 10, no. 10, pp. 780–6, Oct. 2011.

[117] L. Xiao, L. Zhuang, Y. Liu, J. Lu, and H. D. Abruña, “Activating Pd by morphology tailoring for oxygen reduction.,” *J. Am. Chem. Soc.*, vol. 131, no. 2, pp. 602–8, Jan. 2009.

[118] V. Hacker, E. Wallnöfer, W. Baumgartner, T. Schaffer, J. O. Besenhard, H. Schröttner, and M. Schmied, “Carbon nanofiber-based active layers for fuel cell cathodes – preparation and characterization,” *Electrochem. commun.*, vol. 7, no. 4, pp. 377–382, Apr. 2005.

[119] T. C. Nagaiah, S. Kundu, M. Bron, M. Muhler, and W. Schuhmann, “Nitrogen-doped carbon nanotubes as a cathode catalyst for the oxygen reduction reaction in alkaline medium,” *Electrochem. commun.*, vol. 12, no. 3, pp. 338–341, Mar. 2010.

[120] G. Merle, M. Wessling, and K. Nijmeijer, “Anion exchange membranes for alkaline fuel cells: A review,” *J. Memb. Sci.*, vol. 377, no. 1–2, pp. 1–35, Jul. 2011.

[121] R. C. T. Slade, J. P. Kizewski, S. D. Poynton, R. Zeng, and J. R. Varcoe, “Encyclopedia of Sustainability Science and Technology.” Springer New York, New York, NY, pp. 9–29, 2013.

[122] T. N. Danks, R. C. T. Slade, and J. R. Varcoe, “Alkaline anion-exchange radiation-grafted membranes for possible electrochemical application in fuel cells,” *J. Mater. Chem.*, vol. 13, no. 4, pp. 712–721, Mar. 2003.

[123] H. Herman, R. C. . Slade, and J. R. Varcoe, “The radiation-grafting of vinylbenzyl chloride onto poly(hexafluoropropylene-co-tetrafluoroethylene) films with subsequent conversion to alkaline anion-exchange membranes: optimisation of the experimental conditions and characterisation,” *J. Memb. Sci.*, vol. 218, no. 1–2, pp. 147–163, Jul. 2003.

[124] J. Varcoe and R. Slade, “An electron-beam-grafted ETFE alkaline anion-exchange membrane in metal-cation-free solid-state alkaline fuel cells,” *Electrochem. commun.*, vol. 8, no. 5, pp. 839–843, May 2006.

[125] J. R. Varcoe, R. C. T. Slade, L. E. H. Yee, S. D. Poynton, D. J. Driscoll, and D. C. Apperley, “Poly (ethylene- co -tetrafluoroethylene) -Derived Radiation-Grafted Anion-Exchange Membrane with Properties Specifically Tailored for Application in Metal-Cation-Free Alkaline Polymer Electrolyte Fuel Cells,” *Chem. Mater.*, vol. 19, no. 10, pp. 2686–2693, 2007.

[126] J. Wang, J. Wang, S. Li, and S. Zhang, “Poly(arylene ether sulphone)s ionomers with pendant quaternary ammonium groups for alkaline anion exchange membranes: Preparation and stability issues,” *J. Memb. Sci.*, vol. 368, no. 1–2, pp. 246–253, Feb. 2011.

[127] K. H. Gopi, S. G. Peera, S. D. Bhat, P. Sridhar, and S. Pitchumani, “Preparation and characterization of quaternary ammonium functionalized poly(2,6-dimethyl-1,4-phenylene oxide) as anion exchange membrane for alkaline polymer electrolyte fuel cells,” *Int. J. Hydrogen Energy*, vol. 39, no. 6, pp. 2659–2668, Feb. 2014.

[128] K. Shen, J. Pang, S. Feng, Y. Wang, and Z. Jiang, “Synthesis and properties of a novel poly(aryl ether ketone)s with quaternary ammonium pendant groups for anion exchange membranes,” *J. Memb. Sci.*, vol. 440, no. 1, pp. 20–28, Aug. 2013.

[129] J. F. Fauvarque, S. Guinot, N. Bouzir, E. Salmon, and J. F. Penneau, “Alkaline poly(ethylene oxide) solid polymer electrolytes. Application to nickel secondary batteries,” *Electrochim. Acta*, vol. 40, no. 13–14, pp. 2449–2453, Oct. 1995.

[130] C. Yang and S. Lin, “Preparation of composite alkaline polymer electrolyte,” *Mater. Lett.*, vol. 57, no. 4, pp. 873–881, 2002.

[131] C.-C. Yang, S.-J. Lin, and G.-M. Wu, “Study of ionic transport properties of alkaline poly(vinyl) alcohol-based polymer electrolytes,” *Mater. Chem. Phys.*, vol. 92, no. 1, pp. 251–255, Jul. 2005.

[132] C.-C. Yang, S.-J. Lin, and S.-T. Hsu, “Synthesis and characterization of alkaline polyvinyl alcohol and poly(epichlorohydrin) blend polymer electrolytes and performance in electrochemical cells,” *J. Power Sources*, vol. 122, no. 2, pp. 210–218, Jul. 2003.

[133] B. Xing and O. Savadogo, “Hydrogen/oxygen polymer electrolyte membrane fuel cells (PEMFCs) based on alkaline-doped polybenzimidazole (PBI),” *Electrochem. commun.*, vol. 2, no. 10, pp. 697–702, 2000.

[134] J. Fu, Q. Jinli, H. Lv, J. Ma, X.-Z. Yuan, and H. Wang, “Alkali doped poly(vinyl alcohol) (PVA) for anion-exchange membrane fuel cells --- Ionic conductivity, chemical stability and FT-IR characterizations,” *ECS Trans.*, vol. 25, no. 13, pp. 15–23, 2010.

[135] J. Fu, J. Qiao, X. Wang, J. Ma, and T. Okada, “Alkali doped poly(vinyl alcohol) for potential fuel cell applications,” *Synth. Met.*, vol. 160, no. 1–2, pp. 193–199, Jan. 2010.

[136] X. Zhu, B. Wang, and H. Wang, “Effects of [Bmim]OH on structure and conductive properties of alkaline PVA/[Bmim]OH membranes,” *Polym. Bull.*, vol. 65, no. 7, pp. 719–730, Jun. 2010.

[137] R. Jervis and D. J. L. Brett, *Materials for Low-Temperature Fuel Cells*. Weinheim: Wiley, 2015, p. 24.

[138] M. Reinholdt, A. Ilie, S. Roualdès, J. Frugier, M. Schieda, C. Coutanceau, S. Martemianov, V. Flaud, E. Beche, and J. Durand, "Plasma membranes modified by plasma treatment or deposition as solid electrolytes for potential application in solid alkaline fuel cells.," *Membranes (Basel).*, vol. 2, no. 3, pp. 529–52, Jan. 2012.

[139] FuMA-Tech, "Technical Datasheet fumasep FAA-3-PK-130," no. 0. Germany, pp. 1–2, 2014.

[140] D. Briggs and M. P. Seah, *Practical Surface Analysis (2nd Ed.), Vol. 1*. New York: Wiley, 1996.

[141] S. Hüfner and G. K. Wertheim, "Core-line asymmetries in the x-ray-photoemission spectra of metals," *Phys. Rev. B*, vol. 11, no. 2, pp. 678–83, 1975.

[142] I. Bilecka, P. J. Barczuk, and J. Augustynski, "Photoanodic oxidation of small organic molecules at nanostructured TiO2 anatase and rutile film electrodes," *Electrochim. Acta*, vol. 55, no. 3, pp. 979–984, Jan. 2010.

[143] M. M. O. Thotiyl and S. Sampath, "Electrochemical oxidation of ethanol in acid media on titanium nitride supported fuel cell catalysts," *Electrochim. Acta*, vol. 56, no. 10, pp. 3549–3554, Apr. 2011.

[144] J. Kacher, C. Landon, B. L. Adams, and D. Fullwood, "Bragg's Law diffraction simulations for electron backscatter diffraction analysis.," *Ultramicroscopy*, vol. 109, no. 9, pp. 1148–56, Aug. 2009.

[145] Y. Chen, B. He, and H. Liu, "Preparation and Characterization of Palladium Colloidal Nanoparticles by Thermal Decomposition of Palladium Acetate with Microwave Irradiation," *J. Mater. Sci. Technol.*, vol. 21, no. 2, pp. 187–90, 2005.

[146] K. Thamaphat, P. Limsuwan, and B. Ngotawornchai, "Phase Characterization of TiO2 Powder by XRD and TEM," *Kasetsart J. Nat. Sci.*, vol. 42, no. 5, pp. 357–361, 2008.

[147] H.-S. Chen, C. Su, J.-L. Chen, T.-Y. Yang, N.-M. Hsu, and W.-R. Li, "Preparation and Characterization of Pure Rutile TiO2 Nanoparticles for Photocatalytic Study and Thin Films for Dye-Sensitized Solar Cells," *J. Nanomater.*, vol. 2011, p. 869618, 2011.

[148] D. A. H. Hanaor and C. C. Sorrell, "Review of the anatase to rutile phase transformation," *J. Mater. Sci.*, vol. 46, no. 4, pp. 855–874, Dec. 2010.

[149] H. Ahn, H. Choi, K. Park, S. Kim, and Y. Sung, "Investigation of the Structural and Electrochemical Properties of Size-Controlled SnO2 Nanoparticles," *J. Phys. Chem. B*, vol. 108, no. 28, pp. 9815–9820, 2004.

[150] S. A. Pianaro, P. R. Bueno, E. Longo, and J. A. Varela, "A new SnO2-based varistor system," *J. Mater. Sci. Lett.*, vol. 14, no. 10, pp. 692–694, 1995.

[151] D.-F. Zhang, L.-D. Sun, J.-L. Yin, and C.-H. Yan, “Low-Temperature Fabrication of Highly Crystalline SnO2 Nanorods,” *Adv. Mater.*, vol. 15, no. 12, pp. 1022–1025, Jun. 2003.

[152] A. Vantomme, Z.-Y. Yuan, G. Du, and B.-L. Su, “Surfactant-Assisted Large-Scale Preparation of Crystalline CeO 2 Nanorods,” *Langmuir*, vol. 21, no. 3, pp. 1132–1135, 2005.

[153] S. Watanabe, X. Ma, and C. Song, “Characterization of Structural and Surface Properties of Nanocrystalline TiO2 - CeO2 Mixed Oxides by XRD, XPS, TPR, and TPD,” *J. Phys. Chem. C*, vol. 113, no. 32, pp. 14249–14257, 2009.

[154] W. Han, L. Wu, and Y. Zhu, “Formation and Oxidation State of CeO2-x Nanotubes,” *J. Am. Chem. Soc.*, vol. 127, no. 37, pp. 12814–12815, 2005.

[155] J. Biscoe and B. E. Warren, “An X-Ray Study of Carbon Black,” *J. Appl. Phys.*, vol. 13, no. 6, pp. 364–71, 1942.

[156] E. A. Baranova, Y. Le Page, D. Ilin, C. Bock, B. MacDougall, and P. H. J. Mercier, “Size and composition for 1–5nm Ø PtRu alloy nano-particles from Cu Kα X-ray patterns,” *J. Alloys Compd.*, vol. 471, no. 1–2, pp. 387–394, Mar. 2009.

[157] M. Birkholz, *Thin Film Analysis by X-Ray Scattering*. Weinheim: Wiley, 2006, p. 119.

[158] H. Tollefsen, E. O. Laastad, and S. Raaen, “Surface alloying and mixed valence in thin layers of Ce and Pd on Ru(0001),” *Surf. Sci.*, vol. 603, no. 1, pp. 197–202, Jan. 2009.

[159] M. Brun, A. Berthet, and J. C. Bertolini, “XPS, AES and Auger parameter of Pd and PdO,” *J. Electron Spectros. Relat. Phenomena*, vol. 104, no. 1, pp. 55–60, 1999.

[160] M. Josep, P. Regull, L. Victori, and M. D. de Castellar, “XPS and IR (ATR) Analysis of Pd Oxide Films Obtained by Electrochemical Methods,” *Surf. Interface nalysis*, vol. 11, no. 8, pp. 447–449, 1988.

[161] M. C. Militello and S. J. Simko, “Palladium Chloride (PdCl2) by XPS,” *Surf. Sci. Spectra*, vol. 3, no. 4, p. 402, Oct. 1994.

[162] D. Simone, T. Kennelly, N. L. Brungard, and R. J. Farrauto, “Reversible poisoning of palladium catalysts for methane oxidation,” *Appl. Catal.*, vol. 70, no. 1, pp. 87–100, 1991.

[163] N. Mahata and V. Vishwanathan, “Influence of Palladium Precursors on Structural Properties and Phenol Hydrogenation Characteristics of Supported Palladium Catalysts,” *J. Catal.*, vol. 196, no. 2, pp. 262–270, Dec. 2000.

[164] T. Lear, R. Marshall, J. A. Lopez-Sanchez, S. D. Jackson, T. M. Klapötke, M. Bäumer, G. Rupprechter, H.-J. Freund, and D. Lennon, “The application of infrared spectroscopy to probe the surface morphology of alumina-supported palladium catalysts.,” *J. Chem. Phys.*, vol. 123, no. 17, p. 174706, Nov. 2005.

[165] H.-F. Wang, H. Ariga, R. Dowler, M. Sterrer, and H.-J. Freund, “Surface science approach to catalyst preparation – Pd deposition onto thin Fe3O4(111) films from PdCl2 precursor,” *J. Catal.*, vol. 286, no. 1, pp. 1–5, Feb. 2012.

[166] M. Jin, J.-N. Park, J. K. Shon, J. H. Kim, Z. Li, Y.-K. Park, and J. M. Kim, “Low temperature CO oxidation over Pd catalysts supported on highly ordered mesoporous metal oxides,” *Catal. Today*, vol. 185, no. 1, pp. 183–190, May 2012.

[167] H. A. E. Dole, L. F. Safady, S. Ntais, M. Couillard, and E. A. Baranova, “Electrochemically enhanced metal-support interaction of highly dispersed Ru nanoparticles with a CeO2 support,” *J. Catal.*, vol. 318, pp. 85–94, Oct. 2014.

[168] S.-Z. Chen, P.-Y. Zhang, W.-P. Zhu, L. Chen, and S.-M. Xu, “Deactivation of TiO2 photocatalytic films loaded on aluminium: XPS and AFM analyses,” *Appl. Surf. Sci.*, vol. 252, no. 20, pp. 7532–7538, Aug. 2006.

[169] J. A. Taylor, G. M. Lancaster, and W. J. Rabalais, “Chemical reaction of N2+ ion beams with group IV elements and their oxides,” *J. Electron Spectros. Relat. Phenomena*, vol. 13, no. 3, pp. 435–444, 1978.

[170] D. E. Ramaker, J. de Graaf, J. A. R. van Veen, and D. C. Koningsberger, “Nature of the Metal–Support Interaction in Supported Pt Catalysts: Shift in Pt Valence Orbital Energy and Charge Rearrangement,” *J. Catal.*, vol. 203, no. 1, pp. 7–17, Oct. 2001.

[171] S. Bernal, J. J. Calvino, M. A. Cauqui, J. M. Gatica, C. Larese, J. A. P. Omil, and J. M. Pintado, “Some recent results on metal/support interaction effects in NM/CeO2 (NM: noble metal) catalysts,” *Catal. Today*, vol. 50, no. 2, pp. 175–205, 1999.

[172] A. Nazarov and D. Thierry, “Application of Volta potential mapping to determine metal surface defects,” *Electrochim. Acta*, vol. 52, no. 27, pp. 7689–7696, Oct. 2007.

[173] S. Harinipriya and M. V Sangaranarayanan, “Influence of the Work Function on Electron Transfer Processes at Metals : Application to the Hydrogen Evolution Reaction,” *Langmuir*, vol. 18, no. 14, pp. 5572–5578, 2002.

[174] N. E. Singh-Miller and N. Marzari, “Surface energies, work functions, and surface relaxations of low-index metallic surfaces from first principles,” *Phys. Rev. B*, vol. 80, no. 23, p. 235407, Dec. 2009.

[175] E. Roduner, “Size matters: why nanomaterials are different,” *Chem. Soc. Rev.*, vol. 35, no. 7, pp. 583–92, Jul. 2006.

[176] M. N. Islam and M. O. Hakim, “Electron affinity and work function of polycrystalline Sn02 thin film,” *J. Mater. Sci. Lett.*, vol. 5, no. 1, pp. 63–65, 1986.

[177] M. Batzill and U. Diebold, “The surface and materials science of tin oxide,” *Prog. Surf. Sci.*, vol. 79, no. 2–4, pp. 47–154, 2005.

[178] J. Robertson and B. Falabretti, “Electronic Structure of Transparent Conducting Oxides,” in *Handbook of Transparent Conductors*, D. S. Ginley, H. Hosono, and D. C. Payne, Eds. Boston, MA: Springer US, 2011, pp. 27–50.

[179] A. Imanishi, E. Tsuji, and Y. Nakato, “Dependence of the Work Function of TiO2 (Rutile) on Crystal Faces , Studied by a Scanning Auger Microprobe,” *J. Phys. Chem. C*, vol. 111, no. 5, pp. 2128–2132, 2007.

[180] S. S. Warule, N. S. Chaudhari, B. B. Kale, K. R. Patil, P. M. Koinkar, M. A. More, and R. Murakami, “Organization of cubic CeO2 nanoparticles on the edges of self assembled tapered ZnO nanorods via a template free one-pot synthesis: significant cathodoluminescence and field emission properties,” *J. Mater. Chem.*, vol. 22, no. 18, pp. 8887–95, 2012.

[181] A. Ponrouch, S. Garbarino, E. Bertin, C. Andrei, G. A. Botton, and D. Guay, “Highly Porous and Preferentially Oriented {100} Platinum Nanowires and Thin Films,” *Adv. Funct. Mater.*, vol. 22, no. 19, pp. 4172–4181, Oct. 2012.

[182] A. N. Simonov, P. E. Plyusnin, Y. V. Shubin, R. I. Kvon, S. V. Korenev, and V. N. Parmon, “Hydrogen electrooxidation over palladium–gold alloy: Effect of pretreatment in ethylene on catalytic activity and CO tolerance,” *Electrochim. Acta*, vol. 76, pp. 344–353, Aug. 2012.

[183] M. Łukaszewski, M. Grdeń, and A. Czerwiński, “Cyclic voltammetric behavior of Pd–Pt–Rh ternary alloys,” *J. Solid State Electrochem.*, vol. 9, no. 1, pp. 1–9, Apr. 2005.

[184] P. S. Ruvinsky, S. N. Pronkin, V. I. Zaikovskii, P. Bernhardt, and E. R. Savinova, “On the enhanced electrocatalytic activity of Pd overlayers on corbon-supported gold particles in hydrogen electrooxidation,” *Phys. Chem. Chem. Phys.*, vol. 10, no. 44, pp. 6665–76, Jul. 2008.

[185] E. A. Baranova, M. A. Padilla, B. Halevi, T. Amir, K. Artyushkova, and P. Atanassov, “Electrooxidation of ethanol on PtSn nanoparticles in alkaline solution: Correlation between structure and catalytic properties,” *Electrochim. Acta*, vol. 80, pp. 377–382, Oct. 2012.

[186] H. Meng, S. Sun, J. Masse, and J. Dodelet, “Electrosynthesis of Pd Single-Crystal Nanothorns and Their Application in the Oxidation of Formic Acid,” *Chem. Mater.*, vol. 20, no. 22, pp. 6998–7002, 2008.

[187] R. Manoharan and J. B. Goodenough, “Methanol Oxidation in Acid on Ordered NiTi,” *J. Mater. Chem.*, vol. 2, no. 8, pp. 875–887, 1992.

[188] S. Sun, G. Zhang, N. Gauquelin, N. Chen, J. Zhou, S. Yang, W. Chen, X. Meng, D. Geng, M. N. Banis, R. Li, S. Ye, S. Knights, G. A. Botton, T.-K. Sham, and X. Sun, “Single-atom Catalysis Using Pt/Graphene Achieved through Atomic Layer Deposition,” *Sci. Rep.*, vol. 3, pp. 1–9, May 2013.

[189] S. Chibani, C. Michel, F. Delbecq, C. Pinel, and M. Besson, “On the key role of hydroxyl groups in platinum-catalysed alcohol oxidation in aqueous medium,” *Catal. Sci. Technol.*, vol. 3, no. 2, pp. 339–50, 2013.

[190] J.-P. Hsu, *Interfacial forces and fields Theory and application*. New York: Marcel Dekker, 1999.

[191] M. Yaldagard, M. Jahanshahi, and N. Seghatoleslami, “Carbonaceous Nanostructured Support Materials for Low Temperature Fuel Cell Electrocatalysts — A Review,” *World J. Nano Sci. Eng.*, vol. 3, no. 4, pp. 121–153, 2013.

[192] F. Brusciotti, A. Batan, I. De Graeve, M. Wenkin, M. Biessemans, R. Willem, F. Reniers, J. J. Pireaux, M. Piens, J. Vereecken, and H. Terryn, “Characterization of thin water-based silane pre-treatments on aluminium with the incorporation of nano-dispersed CeO2 particles,” *Surf. Coatings Technol.*, vol. 205, no. 2, pp. 603–613, Oct. 2010.

[193] C. Karunakaran and P. Gomathisankar, “Solvothermal Synthesis of CeO2−TiO2 Nanocomposite for Visible Light Photocatalytic Detoxification of Cyanide,” *ACS Sustain. Chem. Eng.*, vol. 1, no. 12, pp. 1555–63, 2013.

[194] J. Horkans, “The hydrogen region of the cyclic voltammetry of Pd: The effect of pH and anion,” *J. Electroanal. Chem.*, vol. 209, no. 2, pp. 371–376, 1986.

[195] L. Assaud, E. Monyoncho, K. Pitzschel, A. Allagui, M. Petit, M. Hanbücken, E. A. Baranova, and L. Santinacci, “3D-nanoarchitectured Pd/Ni catalysts prepared by atomic layer deposition for the electrooxidation of formic acid,” *Beilstein J. Nanotechnol.*, vol. 5, pp. 162–72, Jan. 2014.

[196] J. W. Elam, A. Zinovev, C. Y. Han, H. H. Wang, U. Welp, J. N. Hryn, and M. J. Pellin, “Atomic layer deposition of palladium films on Al2O3 surfaces,” *Thin Solid Films*, vol. 515, no. 4, pp. 1664–1673, Dec. 2006.

[197] B. Chen, J. Hou, and K. Lu, “Formation Mechanism of TiO2 Nanotubes and Their Applications in Photoelectrochemical Water Splitting and Supercapacitors,” *Langmuir*, vol. 29, no. 19, pp. 5911–19, 2013.

[198] L. Assaud, “Fonctionnalisation de Substrats Nano-structurés pour la Conversion et le Stockage de l’Energie,” Université d’Aix-Marseille, 2013.

[199] D. Regonini, C. R. Bowen, A. Jaroenworaluck, and R. Stevens, “A review of growth mechanism, structure and crystallinity of anodized TiO2 nanotubes,” *Mater. Sci. Eng. R*, vol. 74, no. 12, pp. 377–406, Dec. 2013.

[200] L. V. Taveira, J. M. Macák, H. Tsuchiya, L. F. P. Dick, and P. Schmuki, “Initiation and Growth of Self-Organized TiO2 Nanotubes Anodically Formed in NH4F⁄(NH4)2SO4 Electrolytes,” *J. Electrochem. Soc.*, vol. 152, no. 10, p. B405, 2005.

[201] G. Li, Z.-Q. Liu, J. Lu, L. Wang, and Z. Zhang, “Effect of calcination temperature on the morphology and surface properties of TiO2 nanotube arrays,” *Appl. Surf. Sci.*, vol. 255, no. 16, pp. 7323–7328, May 2009.

[202] J. Yu and B. Wang, “Effect of calcination temperature on morphology and photoelectrochemical properties of anodized titanium dioxide nanotube arrays,” *Appl. Catal. B Environ.*, vol. 94, no. 3–4, pp. 295–302, Feb. 2010.

[203] O. K. Varghese, D. Gong, M. Paulose, C. A. Grimes, and E. C. Dickey, “Crystallization and high-temperature structural stability of titanium oxide nanotube arrays,” *J. Mater. Res.*, vol. 18, no. 01, pp. 156–165, Jan. 2011.

[204] D. A. J. Rand and R. Woods, “Determination of Real Surface Area of Palladium Electrodes,” *Anal. Chem.*, vol. 47, no. 8, pp. 1481–1483, 1975.

[205] D. A. J. Rand and R. Woods, “The nature of adsorbed oxygen on rhodium, palladium and gold electrodes,” *Eectroanalytical Chem. Interfacial Electrochem.*, vol. 31, no. 1, pp. 29–38, 1971.

[206] K. Juodkazis, J. Juodkazytė, B. Šebeka, and V. Šukienė, “Kinetic regularities of cathodic reduction of palladium (II) oxide surface layer,” *Russ. J. Electrochem.*, vol. 39, pp. 954–9, 2003.

[207] H. Erikson, A. Kasikov, C. Johans, K. Kontturi, K. Tammeveski, and A. Sarapuu, “Oxygen reduction on Nafion-coated thin-film palladium electrodes,” *J. Electroanal. Chem.*, vol. 652, no. 1–2, pp. 1–7, Mar. 2011.

[208] H. Erikson, A. Sarapuu, K. Tammeveski, J. Solla-Gullón, and J. M. Feliu, “Enhanced electrocatalytic activity of cubic Pd nanoparticles towards the oxygen reduction reaction in acid media,” *Electrochem. commun.*, vol. 13, no. 7, pp. 734–737, Jul. 2011.

[209] M. Grdeń, M. Łukaszewski, G. Jerkiewicz, and A. Czerwiński, “Electrochemical behaviour of palladium electrode: Oxidation, electrodissolution and ionic adsorption,” *Electrochim. Acta*, vol. 53, no. 26, pp. 7583–7598, Nov. 2008.

[210] S. H. Cadle, “Electrochemical oxidation of thin palladium films on gold,” *Anal. Chem.*, vol. 46, no. 4, pp. 587–590, Apr. 1974.

[211] X. Wang, J. Yang, H. Yin, R. Song, and Z. Tang, "'Raisin bun'-like nanocomposites of palladium clusters and porphyrin for superior formic acid oxidation.," *Adv. Mater.*, vol. 25, no. 19, pp. 2728–32, May 2013.

[212] A. N. Correia, L. H. Mascaro, S. A. S. Machado, and L. A. Avaca, "Active surface area determination of Pd-Si alloys by H-adsorption," *Electrochim. Acta*, vol. 42, no. 3, pp. 493–495, 1997.

[213] J. T. Tanskanen, C. Hägglund, and S. F. Bent, "Correlating Growth Characteristics in Atomic Layer Deposition with Precursor Molecular Structure: The Case of Zinc Tin Oxide," *Chem. Mater.*, vol. 26, no. 9, pp. 2795–802, 2014.

[214] V. Srinivasan and J. W. Weidner, "Capacitance studies of cobalt oxide films formed via electrochemical precipitation," *J. Power Sources*, vol. 108, no. 1–2, pp. 15–20, Jun. 2002.

[215] S. Balomenou, F. Sapountzi, D. Presvytes, M. Tsampas, and C. Vayenas, "Triode fuel cells," *Solid State Ionics*, vol. 177, no. 19–25, pp. 2023–2027, Oct. 2006.

[216] F. M. Sapountzi, S. C. Divane, M. N. Tsampas, and C. G. Vayenas, "Enhanced performance of CO poisoned proton exchange membrane fuel cells via triode operation," *Electrochim. Acta*, vol. 56, no. 20, pp. 6966–6975, Aug. 2011.

[217] S. P. Balomenou and C. G. Vayenas, "Triode Fuel Cells and Batteries," *J. Electrochem. Soc.*, vol. 151, no. 11, p. A1874, 2004.

[218] Y. S. Li, T. S. Zhao, and Z. X. Liang, "Performance of alkaline electrolyte-membrane-based direct ethanol fuel cells," *J. Power Sources*, vol. 187, no. 2, pp. 387–392, Feb. 2009.

[219] Z. J. Mellinger and J. G. Chen, "Chapter 2 Metal-Modified Carbide Anode Electrocatalysts," in *Electrocatalysis in Fuel Cells: A Non- and Low Platinum Approach*, M. Shao, Ed. London: Springer, 2013, p. 115.